Numerical Methods for Modeling the Fluid Flow of Pulsing Soft Corals and the Photosynthesis of their Symbiotic Algae

UNIVERSITY OF CALIFORNIA, MERCED

A dissertation submitted in partial satisfaction of the
requirements for the degree

Doctor of Philosophy in Applied Mathematics

Matea Santiago

Committee in charge:

Professor Shilpa Khatri, Chair
Professor Kevin Mitchell
Professor François Blanchette
Professor Laura Miller

2021

The dissertation of Matea Santiago is approved, and it is acceptable in quality and form for publication on microfilm and electronically:

(Kevin Mitchell)

(François Blanchette)

(Laura Miller)

(Shilpa Khatri, Chair)

University of California, Merced

2021

Dedicated to my friends and family. Without their levity, love, and presence in my life, my accomplishments would be hollow.

"*Reduced to general theories, mathematics would be a beautiful form without content.*"

Henri Lebesgue

Contents

List of Figures

List of Tables

Acknowledgements

I would like first to acknowledge my advisor, Prof. Shilpa Khatri, for her guidance throughout my Ph.D. She continually challenged me to improve and become an independent researcher, and for that, I am grateful. I appreciate her tireless support with my many different efforts to diversify my skills and her time and efforts to secure funding throughout my Ph.D. My Ph.D. was the most challenging task I have ever done, and I am grateful for her patience and kindness.

I also would like to acknowledge my committee members. Prof. Laura Miller has been an inspiration and valued collaborator in my work. I am grateful for her mentorship and confidence in me, and I look forward to working with her in the future. Prof. Kevin Mitchell has introduced me to a beautiful side of physics and mathematics. I have thoroughly enjoyed our collaborations and hope to continue using these tools in my research for many more years. In addition to Prof. François Blanchette serving on my committee, he also was one of the people who taught me the fundamentals of fluid dynamics. I am grateful for his attentive insights, which result in better and more substantial work.

I want to thank my primary mentor, Dr. Johannes Blaschke, and supervisor, Dr. Ann Almgren, at the CCSE group in the Computational Research Division at Berkeley National Laboratory. My time as a summer intern was remarkably instructive in making me a more well-rounded and confident researcher. I will always appreciate the time spent helping me grow as a scientist.

I would also like to acknowledge the other students in the Khatri Group Lab. I have greatly enjoyed their company and camaraderie. I would particularly like to acknowledge Shayna Bennett, whom I started out mentoring, but she ended up mentoring me. My cohort was remarkably supportive during my Ph.D., Fabian Santiago, Alex John Quijano, Jessica Taylor, Omar DeGauchy, and Michael Kelley. I am grateful that we went from colleagues to friends. They made the intimidating world of academics approachable and enjoyable. I would also like to acknowledge the many wonderful people in the Applied Mathematics department. There are too many to name, but the people in this department have been astoundingly positive and uplifting.

I also want to thank my family for their continued support and love. My mother, Anett Edington, was the first person to suggest graduate school. My father, Troy Alvarado, supported me unconditionally and was always there to tell me I was working too hard. It made all the difference as a first-generation college student to have parents that always encouraged me to pursue higher education. I credit them with my interest in mathematics. Luckily I believed them when they told me I had a talent for mathematics as I was growing up.

I would like to acknowledge my husband, Fabian Santiago. Without his support, encouragement, compassion, and belief in me, I would not have made it this far. There were many times when he selflessly cared for and sustained me when I

struggled to keep up with my workload. I appreciate and admire his intellect, his convictions, and his tenacity. His presence enriches my life and inspires me, and I look forward to the next chapter in our life together.

Finally, I would like to acknowledge my funding sources throughout my Ph.D. The National Science Foundation primarily funded my research (NSF) grants PHY-1505061 and DMS-1853608. My final year was funded by the NSF Research and Training Grant DMS-1840265 and the Graduate Dean's Dissertation Fellowship from the Graduate Division at UC Merced. Additionally, I had travel funding and summer funding from the Applied Mathematics Department. I also have had travel funding through the Broader Engagements program funded by the Sustainable Horizons Institute. I was fortunate enough to receive funding for internships through the NSF Mathematical Sciences Graduate Internship Program and Berkeley National Laboratory. This work required extensive use of the MERCED cluster at UC Merced, funded by NSF ACI-1429783.

CURRICULUM VITAE

2021	Doctor of Philosophy in Applied Mathematics Advisor: Professor Shilpa Khatri University of California, Merced Merced, CA
2015	Bachelors of Science in Applied Mathematics Sonoma State University Rohnert Park CA

Numerical Methods for Modeling the Fluid Flow of Pulsing Soft Corals and the Photosynthesis of their Symbiotic Algae

By
Matea Santiago
Doctor of Philosophy
University of California, Merced
2021
Professor Shilpa Khatri, Chair

Abstract

This dissertation presents a novel numerical method to study the pulsing behavior of soft corals. Evidence indicates that the pulsing behavior of soft corals in the family *Xeniidae* facilitates photosynthesis of their symbiotic algae. One way to investigate this complex behavior is through mathematical modeling and numerical simulations. The immersed boundary method is used to model the interaction of the coral tentacles with the surrounding fluid. The flow is then coupled with a photosynthesis model. Photosynthesis is modeled by advecting and diffusing oxygen, the byproduct of photosynthesis, where the coral tentacles act as a moving source of oxygen. This work develops a methodology for solving a system of partial differential equations with boundary conditions on a moving immersed elastic boundary. Two-dimensional numerical simulations are presented where the Reynolds and Péclet numbers are varied in the simulations to understand how these parameters affect the mixing and photosynthesis. The mixing is quantified using both the fluid flow and oxygen concentration dynamics. The results show that for the biologically relevant Péclet number, the fluid dynamics significantly affect the photosynthesis and that the biologically relevant Reynolds number is advantageous for mixing and photosynthesis. The models and methods developed have been contributed to the open-source software library implementation of the immersed boundary method, `IB2d`. A three-dimensional numerical simulations of soft coral pulsing are also presented using the `IBAMR` software library. Three-dimensional mixing analysis of the flow is presented. Further, preliminary results of the three-dimensional corals pulsing with a background oxygen concentration are presented with the methodology for modeling the three-dimensional coral tentacles as a sink or source of a concentration.

Chapter 1

Introduction

Scientists in a variety of different disciplines have long been fascinated with the mechanics of moving organisms in fluids such as fish swimming, bird flight, and insect flight [1]. There is a long history of using the knowledge gained from work with organisms and applying these to engineering problems. The mechanics of insect flight has been studied to improve the maneuverability and efficiency of micro-air vehicle (drone) flight [2]. The swimming efficiency of fish has been well studied and has been used to design underwater and above water vehicles [3]. Others have investigated the link between the morphology of aquatic animals and their locomotive efficiency [4] and the effect on foraging behavior [5], the efficiency of propulsion in aquatic animals [6], and the role of hydrodynamic drag on flying and swimming [7]. Experimental studies using digital particle image velocimetry (DPIV) have been used to measure the external forces of swimming fish [8] and the swimming dynamics and efficiency over the changing morphology and resulting Reynolds number regime over the lifetime development of squid [9]. The ability to study these dynamics analytically and experimentally is limited due to the complexity of these systems. Instead, computational simulations are used to gain insight into the roles of the various properties of the system, including length scale, speed, morphology, and kinematics [4]. The studies mentioned above focused on mechanics relating to locomotion. Studies investigating active motion in sessile organisms are more limited. This dissertation will focus on the computational simulations of sessile pulsing soft corals in the family *Xeniidae*. We develop novel modeling and numerical methods to investigate the pulsing phenomenon.

Soft corals are known to be more resistant to ocean acidification than stony corals, which make up the structure of coral reefs [10]. As climate change progresses, understanding the ecological dynamics of coral reefs is vital. This work seeks to bring insight into the energy source of soft corals of the family *Xeniidae*. The purpose of the pulsing motion was thought to help with food capture. However, they are rarely found with food in their gastric cavities [11], [12]. These soft corals are one of the only known sessile animals who move with such an energetically expensive behavior [13]. Experimental studies have shown increased photosynthesis in the symbiotic algae of soft corals that are pulsing compared to stationary corals

[13]. It is believed that the coral's primary source of energy is through this symbiotic relationship.

These experimental studies have suggested that photosynthesis is an oxygen-limited process. Artificially heightened oxygen levels in the fluid tanks resulted in less photosynthesis by the symbiotic algae [13]. Numerical studies by our collaborators simulating the fluid flow around pulsing soft corals [14], [15] focus on analyzing the flow itself. The work presented in this dissertation is the first study to examine the interaction of this fluid flow around the pulsing corals with the photosynthesis of the symbiotic algae.

We are interested in modeling the photosynthesis of the symbiotic algae on pulsing soft corals. There has been extensive work to model different aspects of photosynthesis in leaves [16]–[19] and algae [20]–[22]. We expect that the fluid flow generated from the pulsing behavior enhances the photosynthesis of the symbiotic algae. The role of mixing and fluid flow has been vital for other biological systems. It has been found that mixing is necessary for efficient photobioreactors for cultivating microalgae [23]. Fluid flow and transport of oxygen and carbon dioxide are essential for photosynthesis of benthic marine autotrophs [24] and in particular reef-building stony corals [25], [26]. In this work, the photosynthesis of the symbiotic algae on the tentacles of soft corals, family *Xeniidae*, is modeled to study the effects of motion and fluid flow on the rate of photosynthesis.

This mixing in the fluid due to coral pulsing can facilitate byproduct removal and carbon dioxide access for the symbiotic photosynthetic algae, providing the coral with additional energy [13]. Understanding this phenomenon required the development of fluid simulations coupled with concentration dynamics, which is the primary goal of this dissertation. Numerous problems in the natural world require an understanding of concentration dynamics. Examples include the modeling of pollutants in urban areas [27], chemicals in marine ecology [28], [29], and contaminants in hydrogeological systems [30]. This novel methodology can be used to investigate many of these other applications. It can be used to study photosynthesis on other marine and terrestrial organisms, heat transfer in organic and inorganic materials, and chemical reactions occurring on elastic bodies.

The photosynthesis of the symbiotic algae is modeled with an advection-diffusion equation coupled to an elastic material, the coral tentacle, in a fluid, so the interaction of fluids, flexible materials, and advection-diffusion is of interest. Both advection and diffusion have been studied in heat transfer in general fluid-structure interactions such as over a flexible oscillating fin [31] and a lid-driven cavity with a flexible bottom [32]. However, this work is not simply a fluid-structure interaction; we are modeling a biological process. There are other cases in which advection and diffusion have been used to understand biological processes. Advection and diffusion have played roles in different physiological fluid-structure interactions such as modeling oxygen concentrations in blood vessels [33] and cardiovascular hemodynamics [34]. The advection-diffusion-reaction equations have also been used to model heat

transfer in biological tissues [35] and chemotaxis in bacteria [36]. In our application, the corals pulse and generate fluid flow, which affects the dissolved oxygen and carbon dioxide in the fluid, so we are interested in the interaction of marine organisms, fluid flow, and concentrations and how they play a role in complex physiological and ecological systems. Many prior studies look at the pivotal role of fluid flow and concentrations on marine organisms. In particular, there has been quite a bit of work to understand the uptake of materials by organisms. Turbulence has been known to affect the width of the diffusive layer around small organisms, which can limit their access to necessary nutrients [37]. Concentration dynamics give an understanding of the role of fluid dynamics in nutrient transport and feeding [38]–[40] and reproduction [41], [42]. Using chemical cues to sense and interact with the environment is pivotal in organism and ecological survival. Chemosensory, chemotaxis, and chemoattractants have been well studied [43]–[48]. In this work, we are instead interested in the expelling of byproducts which has limited study [49], [50].

This dissertation will be presenting work modeling the pulsing behavior of an individual coral polyp and its effect on the photosynthesis of their symbiotic algae. The first component of this is modeling the polyp movement and the resulting fluid flow, which is done using the immersed boundary method [51]. The immersed boundary method is a front-tracking method that is particularly well suited for elastic-material fluid interactions, so it has been extensively used to model biomechanical problems. In particular, it has been used to model cardiovascular systems including human hearts [52], aortic heart valve dynamics [53], tubular hearts [54]. It has been used to investigate other aspects of human physiology, such as modeling the cochlea [55] and sperm motility [56]. Additionally, it has been used to model aquatic animal locomotion, such as eels, nematodes, and microorganisms with flagella [57], and jellyfish movement [58]. The immersed boundary method is commonly used and it has been well studied numerically, [59]–[63], extended [64]–[66], and analyzed [67], [68]. There are several open-source implementations of the immersed boundary method. In this dissertation, we will be using and modifying two of these software libraries. There is a two-dimensional implementation in MATLAB and Python, `IB2d`[69] and a three-dimensional implementation in C++, `IBAMR`, with support for adaptive mesh refinement and parallelization[70].

In elastic-structure fluid interactions, the moving deforming elastic material creates a complex boundary condition on the fluid. The immersed boundary method allows the elastic material to be defined with a Lagrangian frame of reference while defining the fluid with an Eulerian frame of reference. The different frames of reference are reconciled using regularized delta functions. These delta functions are used to enforce a no-slip boundary condition at the fluid-elastic interface. This method allows for an elegant simplicity, where the elastic material does not have to be defined on the Eulerian grid as in many other numerical methods [71]. Additionally, the Eulerian fluid grid does not have to be adapted to the Lagrangian elastic material coordinates [72]. Given that we seek to model the biological tissue of the coral

tentacles, moving with a prescribed motion based on kinematic data, the immersed boundary method was chosen as it is well suited to biomechanical problems.

The second component of this work is modeling photosynthesis coupled with the fluid flow. To model photosynthesis, we represent a dissolved gas (carbon dioxide or oxygen) as a concentration in the fluid solved for using the advection-diffusion equations. The symbiotic algae live on the tentacles of the coral, so as the tentacles move through the fluid, they deplete the carbon dioxide (as a sink) and produce oxygen (as a source). Thus, modeling a moving boundary as a source and sink of a concentration is a crucial component of this work and presents the most significant challenge. In this work, the moving immersed boundary acts as a boundary condition for the advection-diffusion equations. There are many ways to numerically enforce a boundary condition of a partial differential equation on a moving deforming interface. Some examples include finite element methods, where the mesh is modified to fit the deforming boundary condition [73]. Finite volume methods define boundary conditions using cell fractions [74]. The current framework uses finite differences with an interface tracking method. This methodology benefits from using a fixed Cartesian grid without the added complexity of computing body-fitted grids, as in the finite element method, or cell fractions, as in the finite volume method. The difficulty of using an interface tracking finite-difference representation is that the interface does not align with the Cartesian grid. The embedded boundary method addresses this by using interpolating polynomials to define flux boundary conditions across interfaces [75]; however, this approach is computationally expensive. We will be developing a method based on a model for a surfactant that is absorbed and desorbed from an interface to a surrounding bulk fluid [76]. In this formulation, the regularized delta function from the immersed boundary method [51] is used to define a source or sink of the concentration on the immersed boundary. This approach has been used to define concentration point sources to model bioconvection of motile bacteria [77] and cell aggregation relating to constructing biofilms [78]. It is a natural approach to coupling an advected and diffused quantity with a fluid-structure interaction solved using the immersed boundary method. This methodology can be used in other applications where a deforming elastic material produces or absorbs heat densities or chemical concentrations.

The other main result of this work is the dynamical systems approach to quantify mixing in the fluid due to the coral tentacle pulsing. We are particularly interested in mixing due to chaotic advection. Mixing is defined as chaotic when the distance between two close passive tracers increases exponentially, i.e., the trajectories are sensitive to initial conditions. The idea of using dynamical systems approaches to understand the role of mixing and chaotic advection in fluid dynamics problems is not new [79]–[85]. We are particularly interested in investigating mixing in environmental and biological flows. Mixing has been studied in the natural world in ocean currents [86], the atmosphere [87], lava flow [88], blood flow [89], and in DNA replication [90]. We will be applying this methodology to understand the fluid mixing

around the pulsing soft corals and are particularly interested in using dynamical systems to understand aquatic organism behavior. Other studies have used these methods to understand fluid mixing around other aquatic organisms. For example, chaotic advection was studied around microfluid slugs [91] and plankton distributions [92]. We want to quantify the role of movement in mixing around the corals. The beating of the flagellum was found to increase mixing and feeding efficiency in sessile microorganisms [93]. Peng and Dabiri used DPIV data around free-swimming moon jellyfish to analyze the fluid flow with a dynamical systems approach to gain insight into their feeding behavior [94]. In this work, we consider the Lagrangian trajectories of passive tracers in computational fluid simulations to gain insight into the mixing by chaotic advection due to the pulsing behavior of the coral.

To capture the fluid flow characteristics in varying regimes, the Reynolds number, the ratio of inertial to viscous forces, and the Péclet number, the ratio of advection to diffusion, are used. The dynamics of fluid flows can be characteristically similar even in regimes with different parameters including, length scales, speeds, or viscosity. The Reynolds number, $Re = \frac{L^2\gamma}{\nu}$, is used to characterize the flow, found by non-dimensionalizing the Navier-Stokes equations. The Reynolds number is defined using the coral tentacle length, L, pulsation frequency, γ, and kinematic fluid viscosity, ν. The dimensionless Péclet, Pe, number is found by non-dimensionalizing the advection-diffusion equation of the photosynthesis model. In this work, the Péclet number, $Pe = \frac{L^2\gamma}{D}$, is defined using the coral tentacle length, pulsation frequency, and the diffusion coefficient of oxygen or carbon dioxide in water, D. In different applications, varying the Reynolds number can give insight into fluid flow behavior at different length scales, velocities, or fluid viscosities. Different numerical studies have varied the Reynolds number in canonical fluid dynamics problems such as lid-driven cavity flow [95], vortex shedding of an oscillating cylinder [96], flow around an airfoil [97], and turbulent channel flow [98]. Here, we vary the Reynolds number around the biologically relevant Reynolds number to understand the role of fluid inertia and viscosity on photosynthesis production and mixing. Varying the Péclet number will give insight into the dynamics of a concentration being advected at different speeds, at different length scales, or differing diffusivity. Numerical studies have varied the Péclet number in order to get insight into mixing [99], swimming speed of phoretic Janus particles [100], and the rising speed of surfactant coated droplets [101]. Here, we vary the Péclet number to understand the role of advection and diffusion on photosynthesis production and mixing. By varying both the Reynolds and Péclet numbers simultaneously, we seek to understand how the Reynolds number and Péclet number interact in a system where the fluid dynamics are coupled to a concentration. Simultaneously varying both parameters has been done in other coupled fluid concentration studies [44], [102], [103]. In this work, we vary the Reynolds and Péclet numbers to understand how these dimensionless parameters affect the mixing due to the fluid dynamics around the pulsing soft coral

and the resulting photosynthesis of their symbiotic algae.

In this dissertation, the modeling and numerical methods for the two-dimensional study are presented in Chapter 2. The results and analysis for the two-dimensional study are presented in Chapter 3. A discussion of adding this methodology to the open-source MATLAB implementation of the software library `IB2d` is given in Chapter 4. The three-dimensional methodology and results for velocity simulations and the corresponding mixing analysis are presented. We will give preliminary work coupling to the three-dimensional velocity simulations to the concentration dynamics in Chapter 5. The discussion and conclusion of this work are provided in Chapter 6.

Chapter 2

Two-Dimensional Modeling and Numerical Methods

The first component in this work is to model the fluid-structure interaction of the pulsing tentacles of the coral polyp. We use the immersed boundary (IB) method to model this moving elastic body, the coral polyp, and the resulting fluid flow [52]. The IB method allows for the flow to be solved computationally on a uniform Cartesian grid around complex, moving, immersed elastic boundaries, described using Lagrangian coordinates. This method allows for straightforward computations without needing complex moving body-fitted grids.

The main goal of this work is to model photosynthesis coupled to the fluid-structure interaction of a pulsing coral polyp. To model the photosynthesis of the symbiotic algae on the coral tentacle, we consider the coral tentacles as a source of oxygen and a sink of carbon dioxide. In this formulation, only the byproduct of photosynthesis, oxygen, is tracked since it has been hypothesized that this process is oxygen-limited [13]. This work has led to a paper that has been submitted [104].

2.1 Mathematical Model

The fluid flow is modeled on a two-dimensional rectangular domain, $\underline{x} = (x_1, x_2) \in \Omega$. The flow velocity, $\underline{u}(\underline{x},t) = (u_1, u_2)$, and pressure, $p(\underline{x},t)$, are solved using the Navier-Stokes equations for an incompressible, viscous fluid in a periodic channel initially at rest,

$$\frac{\partial \underline{u}}{\partial t} + \underline{u} \cdot \nabla \underline{u} + \nabla p = \frac{1}{\mathrm{Re}} \nabla^2 \underline{u} + \underline{f} \ , \tag{2.1}$$

$$\nabla \cdot \underline{u} = 0 \ . \tag{2.2}$$

The velocity has homogeneous Dirichlet boundary conditions at the top and bottom of the domain and periodic boundary conditions at the sides of the domain. The periodic boundary condition is appropriate as these corals live in colonies. The domain is chosen to be large enough so that the boundary conditions do not significantly affect

the flow dynamics around the coral. The pressure boundary conditions are defined implicitly with the Navier-Stokes solver, described below.

The dimensionless Reynolds number is defined as $Re = \frac{L^2\gamma}{\nu}$, where L is the characteristic length, γ is the characteristic frequency, and ν is the kinematic viscosity. In this study, the characteristic length is the length of a coral polyp tentacle, and the characteristic frequency is the frequency of coral pulsation. These values are provided in Table 2.1. The force per area, $\underline{f}(\underline{x},t)$, is the force of the tentacles on the fluid which couples the fluid flow to the immersed boundary.

TABLE 2.1: Physical parameters of the soft coral Xennidae.

parameter	description	value	units
L	tentacle length	0.4070	cm
γ	pulsation frequency	0.5286	sec $^{-1}$
ν	kinematic fluid viscosity	0.01	cm^{2}sec^{-1}
D	diffusion coefficient	2×10^{-5}	cm^{2}sec^{-1}
Re	Reynolds number	8.7546	-

Two additional interaction equations couple the elastic boundary, the coral tentacles, and the fluid. The force defined on the fluid, $\underline{f}(\underline{x},t)$, is extrapolated from the force of the boundary on the fluid, $\underline{F}(s,t)$, which is defined on the Lagrangian boundary,

$$\underline{f}(\underline{x},t) = \int_0^{\ell} \underline{F}(s,t)\delta(\underline{x} - \underline{X}(s,t))ds \ . \tag{2.3}$$

Further, the velocity of the immersed boundary is interpolated from the velocity of the surrounding fluid,

$$\frac{\partial \underline{X}}{\partial t}(s,t) = \underline{U}(s,t) = \underline{u}(\underline{X}(s,t)) = \int_{\Omega} \underline{u}(\underline{x},t)\delta(\underline{x} - \underline{X}(s,t))d\underline{x} \ . \tag{2.4}$$

In these equations, the boundary position is given by $\underline{X}(s,t)$ as a function of the arclength s defined from 0 to ℓ and $\underline{x}$ is the position in the fluid. These equations enforce a no-slip boundary condition at the tentacles.

The force of the boundary on the fluid prescribes the motion of the pulsing coral. Tether points prescribe this motion. These points do not interact with the fluid; instead, they move in a defined way to give the desired pulsing behavior. We compute the force as,

$$\underline{F}(s,t) = \kappa_T(\underline{X}_T(s,t) - \underline{X}(s,t)) + \kappa_d(\underline{U}_T(s,t) - \underline{U}(s,t)) \tag{2.5}$$

for the position of the tether points, $\underline{X}_T(s,t)$, spring constant, κ_T, velocity of the tether points, $\underline{U}_T$, and damping coefficient, κ_d [66].

The tether point positions, $\underline{X}_T(s,t)$, determine how the corals pulse in the numerical simulations. These positions are determined from experimental data [14]. The

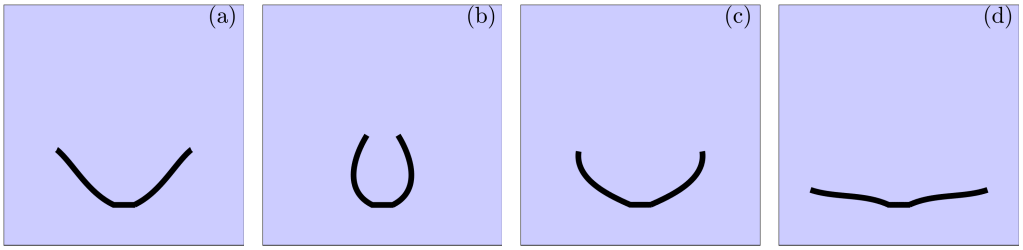

FIGURE 2.1: This figure shows the 2D model coral at (a) 10%, (b) 30%, (c) 50%, and (d) 80% through a pulse.

experimental data is collected assuming the motion of all eight tentacles is identical, and each tentacle moves radially. To model the coral movement in two dimensions, we include two tentacles and assume that the motion of each tentacle is a reflection of the other, see Fig. 2.1. Fig. 2.1(a) shows the closing phase, (b)-(c) show the opening phase, and (d) shows the resting phase.

We use laboratory data to find the kinematic motion of the corals. Experimental videos of pulsing soft corals are used to find the motion of the coral tentacles [14]. Six points are tracked on one tentacle at every frame of five different coral polyps for five pulses. At each frame, polynomials are fit using the position of the six points. Then, the coefficients of these polynomials were nondimensionalized and averaged over the different polyps and pulses. Finally, time-dependent polynomials were fit to these coefficients. The position of the tether points, $\underline{X}_T(s,t) = (X_T(s,t), Y_T(s,t))$, are then given by,

$$X_T(s,t) = C_3(t)s^3 + C_2(t)s^2 + C_1(t)s + C_0(t) \tag{2.6}$$

$$Y_T(s,t) = D_3(t)s^3 + D_2(t)s^2 + D_1(t)s + D_0(t) \tag{2.7}$$

with the time dependent coefficients C_i(t) and $D_i(t)$ for the data a_{ji} and b_{ji}, given by,

$$C_i(t) = b_{4i}t^4 + b_{3i}t^3 + b_{2i}t^2 + b_{1i}t + b_{0i} \tag{2.8}$$

$$D_i(t) = a_{4i}t^4 + a_{3i}t^3 + a_{2i}t^2 + a_{1i}t + a_{0i}\ . \tag{2.9}$$

In the collected experimental data, the coefficients have slight discontinuities in the coral motion and prescribe an initial velocity inconsistent with the assumption that the fluid is initially at rest. To remedy these issues, an equally spaced sample of each coefficient is taken, and then a curve is fit through the sample using clamped splines, enforcing continuity and a zero initial velocity to get consistent initial conditions, as shown in Fig. 2.2 for one coefficient.

The next component in this work is modeling photosynthesis. The concentration

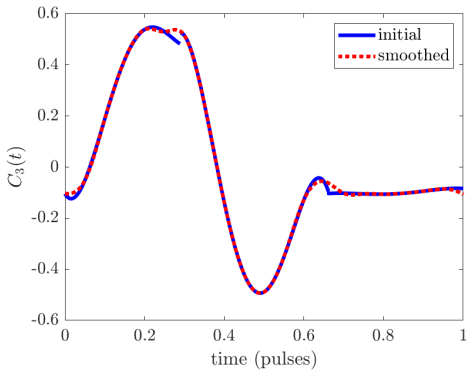

FIGURE 2.2: Example of coefficient $C_3(t)$ from experimental data (blue) and the smoothed fit used in the modeling (red).

dynamics of the oxygen byproduct are modeled using an advection-diffusion equation with an additional source term, coupled to the immersed boundary equations, Eqs. (2.1)-(2.5),

$$c_t + \underline{u} \cdot \nabla c = \frac{1}{Pe} \nabla^2 c + \int_\Gamma \tilde{f}(s,t)\delta(\underline{x} - \underline{X}(s,t))d\underline{s} \ . \tag{2.10}$$

Here, $c(\underline{x},t)$ is the oxygen concentration and $\underline{u}(\underline{x},t)$ is the fluid velocity solved for in Eqs. (2.1)-(2.2). The concentration has no-flux boundary conditions at the top and bottom of the domain and periodic boundary conditions at the sides of the domain. The dimensionless Péclet number is defined as $Pe = \frac{L^2\gamma}{D}$, where the characteristic length L, frequency γ, and diffusion coefficient D are given in Table 2.1. The last term in Eq. (2.10) models the tentacle as a source of oxygen, where $\tilde{f}(s,t)$ is the photosynthesis model chosen. This approach is based on the modeling by Chen and Lai for surfactants [76]. A similar approach has been used as point sources of concentration to model bioconvection of motile bacteria [77], and cell aggregation relating to constructing biofilms [105]. It is a natural approach to coupling an advected and diffused quantity with a fluid-structure interaction solved using the immersed boundary method.

We choose an oxygen-limited model for photosynthesis,

$$\tilde{f}(s,t) = \kappa(1 - C(s,t)) \ , \tag{2.11}$$

where

$$C(s,t) = \int_\Omega c(\underline{x},t)\delta(\underline{x} - \underline{X}(s,t))d\underline{x} \ . \tag{2.12}$$

Here Eq. (2.12) shows the oxygen concentration that has been interpolated onto the tentacles. It gives a measure of how much oxygen is present locally around the

tentacles. κ is the absorption rate of oxygen to the tentacles. The amount of photosynthesis that occurs and the amount of oxygen byproduct produced is dependent only on the amount of oxygen present locally. Since this model does not depend on carbon dioxide, there is no need to model and track the carbon dioxide concentration.

We also consider another model to analyze and validate the methodology. The constant model assumes $\tilde{f}(s,t) = \kappa$, where a constant amount of oxygen is produced at all times. For both models, there is no initial concentration present in the domain. We also considered a model with no sources or sinks ($\tilde{f}(s,t) = 0$) and with an initial condition of a Gaussian function defined along the tentacles. It was found that the dynamics of this system did not capture the photosynthesis dynamics. Chapter 3 presents minimal results of this model. Therefore, the novel modeling introduced by Eq. (2.10) is necessary to capture the photosynthesis dynamics coupled to the pulsing motion and fluid flow.

2.2 Numerical Method

First, the numerical discretization of the IB method for the fluid flow is discussed, and then the discretization of the advection-diffusion equation for the oxygen concentration dynamics is presented.

There are three components in discretizing the IB method: discretizing the Navier-Stokes equations, the immersed boundary, and the interaction equations, which provide the coupling between the two. A projection method is used to solve the Navier-Stokes equations, Eqs. (2.1)-(2.2). Projection methods, first developed by Chorin [106], are a standard finite difference approach to solving the Navier-Stokes equations. In this work, the rotational form of the incremental pressure-correction method developed by Timmermans et al. is used [107]. The rotational form avoids prescribing artificial numerical boundary conditions for the pressure. In a periodic channel, this method is proven to be second-order convergent for the velocity and pressure [108] and has been used with other immersed boundary problems [109], [110].

The fluid is discretized on a marker and cell grid [111] with a mesh width h and time step Δt. We use standard centered finite differences for the discrete gradient, ∇_h, and discrete Laplacian, ∇_h^2, operators. The immersed boundary is discretized with N points separated by $\Delta s \approx \frac{h}{2}$ which is a necessary numerical constraint [51]. The position of the kth point at time t^n, on the boundary curve representing the coral tentacles is denoted $\underline{X}_k^n$ and the position of the kth tether point at the same time is similarly denoted $\underline{X}_{T_k}^n$.

Choosing a method to compute the force, $\underline{f}$, is non-trivial [112] since the force is dependent on the tentacle location. Therefore, we chose to handle it explicitly and solve the fully coupled system by taking two half-time steps. In the first step, the velocity at times t^n and $t^{n-1/2}$ and the pressure and boundary position at time t^n are used to advance the solution to the system to time $t^{n+1/2}$.

First, the velocity $\underline{U}^n$ on the boundary $\underline{X}^n$ is evaluated using the trapezoidal rule and a regularized delta function, δ_h to discretize Eq. (2.4),

$$\underline{U}_k^n = \sum_{ij} \underline{u}_{ij}^n \delta_h(\underline{X}_k^n - \underline{x}_{ij}) h^2 \tag{2.13}$$

where the ij subscripts denote the Cartesian grid points on the fluid grid. The boundary is then advanced a half time step using forward Euler,

$$\underline{X}_k^{n+1/2} = \underline{X}_k^n + \frac{\Delta t}{2} \underline{U}_k^n \ .$$

The force, $\underline{F}^{n+1/2}$ is computed on this boundary, $\underline{X}^{n+\frac{1}{2}}$, using Eq. (2.5),

$$\underline{F}_k^{n+1/2} = \kappa_T (\underline{X}_T{}_k^{n+1/2} - \underline{X}_k^{n+1/2}) + \kappa_d \left(\frac{\underline{X}_T{}_k^{n+1/2} - \underline{X}_T{}_k^{n-1/2}}{\Delta t} - \underline{U}_k^n \right).$$

and then spread to the fluid grid to evaluate $\underline{f}^{n+\frac{1}{2}}$, using the trapezoidal rule for Eq. (2.3),

$$\underline{f}_{ij}^{n+1/2} = \sum_{k=1}^{N-1} \left(\underline{F}_k^{n+1/2} \delta_h(\underline{X}_k^{n+1/2} - \underline{x}_{ij}) + \underline{F}_{k+1}^{n+1/2} \delta_h(\underline{X}_{k+1}^{n+1/2} - \underline{x}_{ij}) \right) \frac{\Delta s}{2} \ . \tag{2.14}$$

Then, the Navier-Stokes equations Eqs. (2.1)-(2.2) are solved at time $t^{n+1/2}$ for the fluid velocity $\underline{u}^{n+\frac{1}{2}}$ and pressure $p^{n+\frac{1}{2}}$ using the force $\underline{f}^{n+\frac{1}{2}}$. First, a second-order backwards difference formula is used to advance Eq. (2.1) a half time step for an intermediate velocity field $\underline{\tilde{u}}^{n+1/2}$ at time $t^{n+1/2}$ using the velocities, $\underline{u}^n$ and $\underline{u}^{n-1/2}$ at times t^n and $t^{n-1/2}$, respectively, and the pressure at time t^n, p^n,

$$\frac{1}{\Delta t}(3\underline{\tilde{u}}^{n+1/2} - 4\underline{u}^n + \underline{u}^{n-1/2}) + 2(\underline{u}^n \cdot \nabla_h)\underline{u}^n - (\underline{u}^{n-1/2} \cdot \nabla_h)\underline{u}^{n-1/2} - \frac{1}{\mathrm{Re}} \nabla_h^2 \underline{\tilde{u}}^{n+1/2} + \nabla_h p^n = \underline{f}^{n+1/2} \ .$$

Using the intermediate velocity, $\underline{\tilde{u}}^{n+1/2}$, a Poisson equation is then solved for the auxiliary function $\psi^{n+1/2}$,

$$\nabla_h^2 \psi^{n+1/2} = \frac{3}{\Delta t} \nabla_h \cdot \underline{\tilde{u}}^{n+1/2} \ ,$$

with mixed homogeneous Neumann (on the top and bottom of the rectangular domain) and periodic (on the sides of the rectangular domain) boundary conditions. Finally, the auxiliary function, $\psi^{n+1/2}$, is used to update the pressure and velocity at

time $t^{n+1/2}$,

$$p^{n+1/2} = \psi^{n+1/2} + p^n - \frac{1}{\mathrm{Re}}\nabla_h \cdot \underline{\tilde{u}}^{n+1/2} \ ,$$

$$\underline{u}^{n+1/2} = \underline{\tilde{u}}^{n+1/2} - \frac{1}{3}\Delta t \nabla_h \psi^{n+1/2} \ .$$

which enforces the incompressibility condition, Eq. (2.2).

In the second step, the velocity at times $t^{n+1/2}$ and t^n, and pressure and boundary position at time $t^{n+1/2}$, evaluated in the first step, are used to advance the solution of the coupled system to time t^{n+1} using similar methodology as in the first step. The boundary velocity $\underline{U}^{n+\frac{1}{2}}$ on the boundary $\underline{X}^{n+\frac{1}{2}}$ is computed using the trapezoidal rule, similar to Eq. (2.13), using the velocity solved for in the previous step, $\underline{u}^{n+\frac{1}{2}}$. The boundary is then advanced a full time step using this velocity, $\underline{X}^{n+1} = \underline{X}^n + \Delta t \underline{U}^{n+\frac{1}{2}}$. Finally, the Navier-Stokes equations Eqs. (2.1)-(2.2) are solved at time t^{n+1} for fluid velocity $\underline{u}^{n+1}$ and pressure p^{n+1} using the force $\underline{f}^{n+\frac{1}{2}}$ using the same method as in the first step,

$$\frac{1}{\Delta t}(3\underline{\tilde{u}}^{n+1} - 4\underline{u}^{n+1/2} + \underline{u}^n) + 2(\underline{u}^{n+1/2} \cdot \nabla_h)\underline{u}^{n+1/2} - (\underline{u}^n \cdot \nabla_h)\underline{u}^n - \frac{1}{\mathrm{Re}}\nabla_h^2 \underline{\tilde{u}}^{n+1} + \nabla_h p^{n+1/2} = \underline{f}^{n+1/2} \ ,$$

$$\nabla_h^2 \psi^{n+1} = \frac{3}{\Delta t}\nabla_h \cdot \underline{\tilde{u}}^{n+1} \ ,$$

$$p^{n+1} = \psi^{n+1} + p^{n+1/2} - \frac{1}{\mathrm{Re}}\nabla_h \cdot \underline{\tilde{u}}^{n+1} \ ,$$

$$\underline{u}^{n+1} = \underline{\tilde{u}}^{n+1} - \frac{1}{3}\Delta t \nabla_h \psi^{n+1} \ .$$

Note once again, an auxiliary function ψ^{n+1} has been introduced to enforce the incompressibility condition.

An analytic delta function would not capture the interaction of the fluid grid and the boundary in Eqs. (2.13)-(2.14) because the immersed boundary Lagrangian points do not perfectly align with the Cartesian fluid grid. Therefore a regularized delta function is used at $\underline{x} = (x_1, x_2)$, defined as $\delta_h(\underline{x}) = \delta_h(x_1)\delta_h(x_2)$ where δ_h is a smooth continuous function with bounded support in the form $\delta_h(x) = \frac{1}{h}\phi(\frac{x}{h})$. In this work $\phi(r)$ is defined as,

$$\phi(r) = \begin{cases} \frac{1}{4}(1 + \cos(\frac{r\pi}{2})) & |\, r \,| \leq 2 \\ 0 & \text{otherwise} \end{cases} \ .$$

This $\phi(r)$ is an approximation for the analytically found second order $\phi_a(r)$,

$$\phi_a(r) = \begin{cases} \frac{1}{8}\left(5+2r-\sqrt{-7-12r-4r^2}\right) & -2 \le r \le -1 \\ \frac{1}{8}\left(3+2r+\sqrt{1-4r-4r^2}\right) & -1 \le r \le 0 \\ \frac{1}{8}\left(3-2r+\sqrt{1+4r-4r^2}\right) & 0 \le r \le 1 \\ \frac{1}{8}\left(5-2r-\sqrt{-7+12r-4r^2}\right) & 1 \le r \le 2 \\ 0 & \text{otherwise} \end{cases} .$$

We choose to use ϕ rather than ϕ_a because it cuts down computational time. Further details for this choice of $\phi(x)$ are discussed in Peskin 2002 [51].

Once the fluid-structure interaction equations are solved, we use the fluid velocity and coral tentacle locations to solve for the oxygen concentration. Strang splitting is used to solve the advection-diffusion equation, Eq. (2.10) [113]. Using Strang splitting, the advection and diffusion operators are split so that each may be solved using different numerical methods. The forcing term in the advection-diffusion equation involves the concentration dynamics defined on the boundary, and therefore solving implicitly would be challenging. A similar approach as used to discretize the IB method is used.

The solution is advanced a half time step in order to find the concentration solution, $c^{n+1/2}$, using c^n to compute $\tilde{f}_k^n$ using either the oxygen-limited model, Eq. (2.11), or the constant model. In the oxygen-limited model, the trapezoidal rule is used to discretize Eq. (2.12) to evaluate C_k^n. First, a quarter step is taken and the advection equation is solved using an explicit upwinding method,

$$c^* = c^n - \frac{\Delta t}{4}\left(u_1^n \tilde{c_x}^n + u_2^n \tilde{c_y}^n\right) .$$

The discrete derivatives, $\tilde{c_x}$ and $\tilde{c_y}$, are determined using a third-order weighted essentially non-oscillatory (WENO) scheme developed by Lui et. al. [114]. The WENO scheme takes the weighted average of all possible, depending on the desired order of accuracy, finite difference stencils as the derivative approximation. The stencils that result in larger magnitude derivative approximations are given a smaller weight so that the solution does not propagate spurious oscillations. Then, a half time step of Crank-Nicolson, an implicit method, is used to solve the diffusion equation with the source term kept fully explicit,

$$\frac{c^{**}-c^*}{\Delta t} = \frac{1}{Pe}\nabla_h^2(c^{**}+c^*) + \sum_{k=1}^{N} \tilde{f}_k^n \delta_h(\underline{X}_k^n - \underline{x}_{ij})\Delta s .$$

Then, another quarter time step of the advection equation is used to compute $c^{n+1/2}$,

$$c^{n+1/2} = c^{**} - \frac{\Delta t}{4}\left(u_1^n \tilde{c_x}^{**} + u_2^n \tilde{c_y}^{**}\right) \ .$$

In the second step, $c^{n+1/2}$ is used to find $\tilde{f}_k^{n+1/2}$ which is then used to advance the concentration solution a full time step in a similar manner as in the previous step to find c^{n+1},

$$c^{*} = c^{n} - \frac{\Delta t}{2}\left(u_1^n \tilde{c_x}^{n} + u_2^n \tilde{c_y}^{n}\right) \ ,$$

$$\frac{c^{**} - c^{*}}{2\Delta t} = \frac{1}{Pe}\nabla_h^2(c^{**} + c^{*}) + \sum_{k=1}^{N} \tilde{f}_k^{n+1/2}\delta_h(\underline{X}_k^{n+1/2} - \underline{x}_{ij})\Delta s,$$

$$c^{n+1} = c^{**} - \frac{\Delta t}{2}\left(u_1^n \tilde{c_x}^{**} + u_2^n \tilde{c_y}^{**}\right) \ .$$

Here, we have presented the coupled system advanced one-time step, solving for the velocity, pressure, and oxygen concentration. The system is then solved over multiple time steps until the desired final time is reached.

2.2.1 Convergence Studies

In order to validate the methodology, a convergence study is conducted for a pulsing coral at Re = 8 up to final time 0.4, 40% through a pulse on a 3×3 domain. The grid sizes used for the fluid grid are h = 0.03, 0.015, 0.0075, and 0.00375. The number of points to discretize a tentacle is given by $N = \lceil 2/h \rceil$. The spring constant in Eq. (2.5) is dependent on the number of immersed boundary points, defined as $\kappa_T = \frac{C_T}{\rho L^3 \gamma^2} N^2$ and the damping coefficient in Eq. (2.5) is dependent on the spring constant, $\kappa_d = C_d\sqrt{\kappa_T}$ [66]. For stability, the time step Δt is dependent on the spring constant, $\Delta t = \frac{\gamma C_t}{\sqrt{\kappa_T}}$ [66]. C_T, C_d, and C_t are constants that need to be empirically chosen. C_T =100 is chosen to be as large as necessary, and C_t = 1/106.4057 is chosen to be as small as necessary. C_d = 5 is chosen to provide damping to the springs for stability. The error at mesh width h, for a quantity Q_h is approximated as $Q_h - Q_{h/2}$.

The convergence results for the velocity field are shown in Table 2.2. We would

TABLE 2.2: Convergence results for the velocity field. The error and order of convergence is presented in both the L_2 and L_∞ norms for both components of the velocity field, u_1 and u_2.

h	Δt	$\|u_{1h} - u_{1h/2}\|_2$	order	$\|u_{2h} - u_{2h/2}\|_2$	order	$\|u_{1h} - u_{1h/2}\|_\infty$	order	$\|u_{2h} - u_{2h/2}\|_\infty$	order
0.0300	2.50×10^{-6}	3.42×10^{-1}	-	4.89×10^{-1}	-	1.72×10^{0}	-	1.04×10^{0}	-
0.0150	1.25×10^{-6}	1.63×10^{-1}	1.06	1.93×10^{-1}	1.34	1.20×10^{0}	0.52	6.11×10^{-1}	1.06
0.0075	6.25×10^{-7}	8.09×10^{-2}	1.01	8.47×10^{-2}	1.19	9.38×10^{-1}	0.35	3.44×10^{-1}	1.01

expect above first order in the L_2 norm and first order in the L_∞ norm for an idealized case assuming Stokes flow and a closed immersed boundary [68], [115]. However, in this work, the Navier-Stokes equations are used and coupled to an open immersed boundary. In prescribing the motion of the coral tentacles, there is a substantial initial acceleration to allow for accuracy of the coral motion. This initial motion yields significant initial errors in the tether points and thus in the fluid, particularly for a coarse mesh seen in the convergence study. However, as we refine the grid, the method is converging at approximately the expected order.

A corresponding convergence study is conducted for the concentration dynamics coupled to the flow up to the final time $t = 0.4$. The previous study's velocity fields and boundary positions are used, so the concentration is solved using the same grid sizes used for the fluid flow, $h = 0.03$, 0.015, 0.0075, and 0.00375. The time step, $\Delta t = \frac{h}{240}$ is significantly larger than for the velocity solution. The smaller time step used for the IB simulations is necessary for the stability of the velocity fields due to the large spring constant but is not necessary for computing the concentration dynamics. The time step chosen satisfies the CFL condition of the advection equation.

The error and the norms are computed as in the velocity convergence study. The convergence study results for the concentration with $Pe = 1$ and $Pe = 400$ are shown in Table 2.3. As the Péclet number increases, the solutions have sharper gradients at the tentacles, which slightly degrades the order of convergence observed. However, one can observe that the solution is converging to first order.

To understand what grid sizes need to be used for the simulations, we also need

TABLE 2.3: Convergence results for the concentration field solved using the oxygen-limited source term. The error and order of convergence is presented in both the L_2 and L_∞ norms for $Pe = 1$ and $Pe = 400$.

		$Pe = 1$				$Pe = 400$			
h	Δt	$\|\|c_h - c_{h/2}\|\|_2$	order	$\|\|c_h - c_{h/2}\|\|_\infty$	order	$\|\|c_h - c_{h/2}\|\|_2$	order	$\|\|c_h - c_{h/2}\|\|_\infty$	order
0.0300	1.25×10^{-4}	6.30×10^{-4}	-	1.07×10^{-3}	-	2.62×10^{-2}	-	9.87×10^{-2}	-
0.0150	6.25×10^{-5}	3.34×10^{-4}	0.92	7.76×10^{-4}	0.46	1.39×10^{-2}	0.92	6.19×10^{-2}	0.67
0.0075	3.12×10^{-5}	6.65×10^{-5}	2.33	2.32×10^{-4}	1.74	7.26×10^{-3}	0.94	4.54×10^{-2}	0.45

to consider the relative error. In Table 2.4, the relative error,

$$\frac{|| Q_h - Q_{h/2} ||}{|| Q_{h/2} ||},$$

for a quantity Q_h approximated at spatial grid h in the L_2 and L_∞ norm are shown for $Re = 8$ and $Pe = 1$ and 400. The relative L_2 error of the velocities are small, 5% or less at the two most refined meshes. The relative L_∞ error is decreasing but still relatively large for the horizontal velocity. However, this error is localized around the tentacles. In the simulations shown in Chapter 3, the spatial grid chosen for the

velocity simulations is the intermediate spatial grid $h = 0.015$ and a time step of $\Delta t = 2.666 \times 10^{-6}$. A time step approximately double that of the time step in the convergence study is chosen, as most of the error is due to the spatial discretization, and this choice does not significantly modify the results. This time step choice allows for shorter wall-clock times for the simulations.

The relative errors for the concentration are also presented in Table 2.4. The L_2 and L_∞ errors with Pe = 1 is always less than 4%. The concentration dynamics have much sharper gradients near the tentacles as the Péclet number increases. So the relative L_2 error for Pe = 400 has much larger errors for coarse grids but less than 6% for the finest mesh. The relative L_∞ error similarly has large values for the coarse grids but decreases for the most refined mesh. In this case, it is clear that we need to use the most refined mesh for the larger Péclet numbers, so the finest mesh, $h = 0.0075$, with a time step of $\Delta t = 5.3203 \times 10^{-4}$ is chosen for all the concentration simulations. Again, a larger time step is chosen for the simulations since most of the error is due to spatial discretizations. In order to couple the fluid grid with a coarser mesh to the finer concentration grid, the velocity is interpolated onto the finer mesh using a second-order method.

TABLE 2.4: Relative error for the fluid velocity with $Re = 8$ and concentration dynamics with Pe = 1 and Pe = 400 using the L_2 and L_∞ norms. The time steps used to compute the velocity and concentration simulations are $\Delta t = h/12000$ and $\Delta t = h/240$, respectively.

	$Re = 8$		$Pe = 1$	$Pe = 400$	$Re = 8$		$Pe = 1$	$Pe = 400$
h	$\frac{\|u_{1h}-u_{1h/2}\|_2}{\|u_{1h}\|_2}$	$\frac{\|u_{2h}-u_{2h/2}\|_2}{\|u_{2h}\|_2}$	$\frac{\|c_h-c_{h/2}\|_2}{\|c_h\|_2}$	$\frac{\|c_h-c_{h/2}\|_2}{\|c_h\|_2}$	$\frac{\|u_{1h}-u_{1h/2}\|_\infty}{\|u_{1h}\|_\infty}$	$\frac{\|u_{2h}-u_{2h/2}\|_\infty}{\|u_{2h}\|_\infty}$	$\frac{\|c_h-c_{h/2}\|_\infty}{\|c_h\|_\infty}$	$\frac{\|c_h-c_{h/2}\|_\infty}{\|c_h\|_\infty}$
0.0300	0.099	0.075	0.016	0.227	0.429	0.145	0.032	0.312
0.0150	0.050	0.032	0.009	0.113	0.307	0.089	0.023	0.163
0.0075	0.026	0.014	0.002	0.059	0.253	0.051	0.007	0.107

Chapter 3

Two-Dimensional Results

Numerical simulations and analyses were conducted to study the interplay of the photosynthesis of the symbiotic algae and the fluid flow created by the pulsing soft corals. Fluid flow results are provided in Section 3.1 and analysis of the fluid mixing is provided in Section 3.2. We use the periodic steady-state velocity simulations to quantify the mixing using a dynamical systems approach. The results of the simulations of the pulsing coral coupled with the photosynthesis model are provided in Section 3.3. We analyze the dynamics in order to understand the role of mixing in photosynthesis. These results have been included in the paper that has been submitted [104].

3.1 Velocity Simulations

Here, we present simulations of the fluid flow of the pulsing coral. The Reynolds number is varied in these simulations, Re = 1, 4, 8, 12, and 16, around the biologically relevant Reynolds number, $Re \approx 8$. The simulations are run on a 3.75 $\times$ 9 domain. This choice of domain size is discussed below. These simulations are run until they reach a quasi-steady state and are time-periodic. For $Re = 1$, 4, and 8, steady-state is achieved by nine pulses, and for Re = 12 and 16, steady-state is achieved by twenty-four pulses. Snapshots of the velocity field during the ninth pulse for the $Re = 8$ simulation are shown in Fig. 3.1.

Average horizontal and vertical velocities on vertical and horizontal lines, respectively, for Re = 1, 8, and 16 at varying distances from the pulsing coral are presented in Fig. 3.2. Results of the last three pulses of each simulation are presented, denoted by the shading. The vertical dashed black lines indicate the change of phase during each pulse. The first dotted black line in each pulse indicates the transition from closing to opening, and the second line indicates the transition from opening to resting. These results show that the flow has reached a periodic steady state. Re = 4 and 12, not presented, have also reached a periodic steady state. These time-periodic solutions will be analyzed below.

We observe more reversible flow, as expected, for the lower Reynolds numbers. In Fig. 3.2(b)-(d), the solid blue line presents the average vertical velocity directly

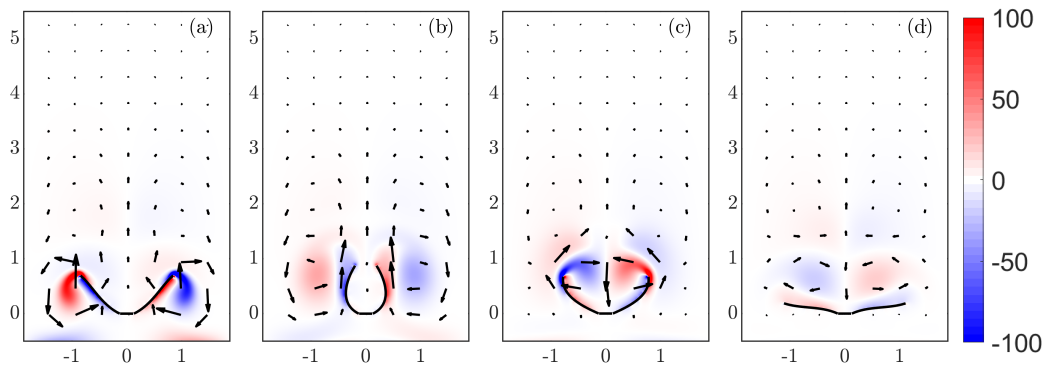

FIGURE 3.1: The fluid flow of a pulsing soft coral at $Re = 8$ at (a) 10%, (b) 30%, (c) 50%, and (d) 80% of a pulse. The color map shows the dimensionless vorticity and the vectors give the dimensionless velocity field in the simulation. Note that these panels only present a subset of the full domain.

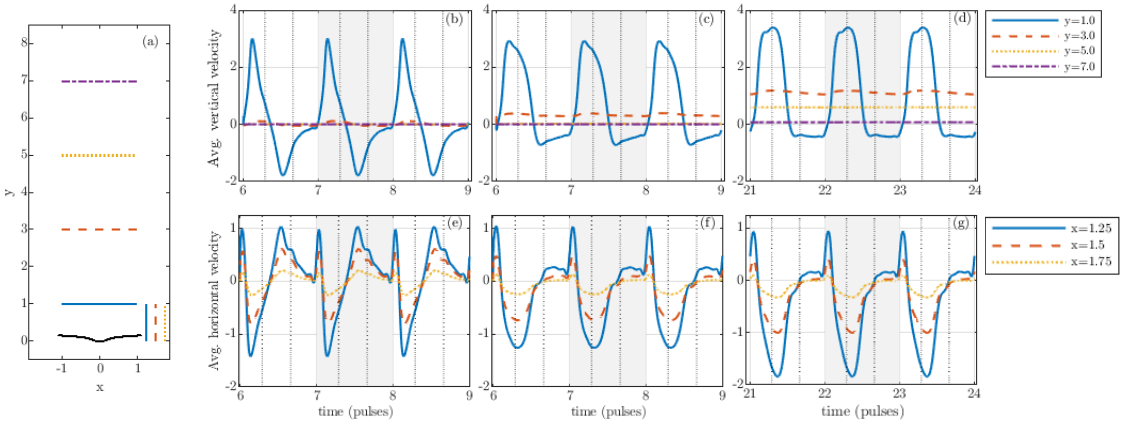

FIGURE 3.2: Average dimensionless velocities along lines at varying distances from the pulsing coral during the last three pulses of the simulations for (b,e) $Re = 1$, (c,f) $Re = 8$, and (d,g) $Re = 16$. (b)-(d) The average vertical velocities on the horizontal lines shown in (a). (e)-(g) The average horizontal velocities on the vertical lines shown in (a). The different colors and line styles correspond to the lines shown in (a).

above the coral. There is less backflow for $Re = 8$ and 16 than for $Re = 1$ since these cases have more inertia in the flow. In Fig. 3.2(b) at Re = 1, the average vertical velocity two tentacle lengths above the top of the coral (red dashed line) is small in magnitude and slightly oscillates between positive and negative, mirroring the behavior directly above the coral. In Fig. 3.2(c)-(d) at $Re = 8$ and 16, the red dashed line remains positive, and as the Reynolds number increases, the magnitude of the positive average velocity increases. $Re = 16$ is the only case in which the average

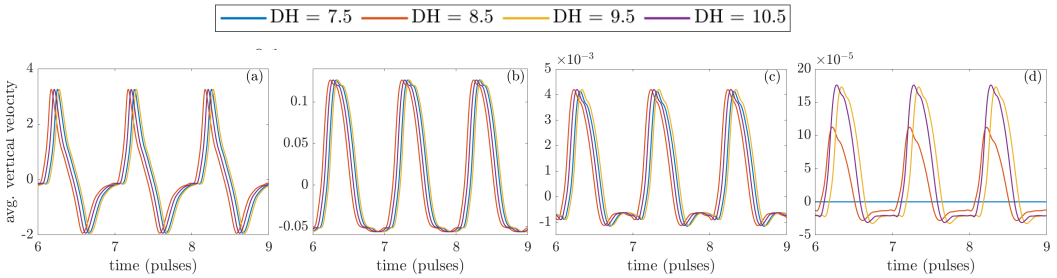

FIGURE 3.3: Average dimensionless vertical velocities over time for varying domain heights (DH) along the horizontal lines presented in Fig. 3.2(a) at (a) $y = 1$, (b) $y = 3$, (c) $y = 5$, and (d) $y = 7$ for $Re = 1$. The domain width was kept constant at 3.75.

vertical velocity four tentacle lengths above the top of the coral (yellow dotted line) is noticeably greater than zero. For $Re = 8$ and 16, there is continuous upward flow away from the coral, and as the Reynolds number increases, the magnitude of the upward flow increases. This upward flow is important as the contributions of this flow to the photosynthesis dynamics are analyzed.

As stated above, to determine the appropriate domain size for the simulations, the effect of the velocity boundary conditions on the flow results is examined by conducting a study of varying domain sizes. Both the length and width of the domain were varied for $Re = 1$, Figs. 3.3 and 3.4, and for $Re = 16$, Figs. 3.5 and 3.6, to make sure that the results presented in Fig. 3.2 were convergent in the domain size. This domain study uses a coarser resolution than the final simulations to speed up the computation time. We chose the domain size for the final simulations such that the consecutive average velocities along the horizontal and vertical lines shown in Fig. 3.2(a) were not qualitatively different. The average horizontal velocities along vertical lines in domains with varying widths are shown in Figs. 3.4 and 3.6. The behavior is qualitatively similar, and therefore a domain width of 3.75 is chosen. We show simulations on domains with varying heights in Figs. 3.3 and 3.5. One can observe that the average velocities are converging in an oscillatory fashion for the three largest domains, i.e., the distance between consecutively larger domains is getting smaller, so a domain height of 9 is chosen. In Fig. 3.5(c)-(d), there are some different dynamics than those observed in Fig. 3.2(d), but this inaccuracy is attributed to the coarse mesh used.

3.2 Mixing Analysis

Next, we quantify how the fluid flow contributes to transport away from the coral tentacles as we vary the Reynolds number. Flow trajectories are used to build a Poincaré Map. This tool is commonly used in dynamical systems to characterize

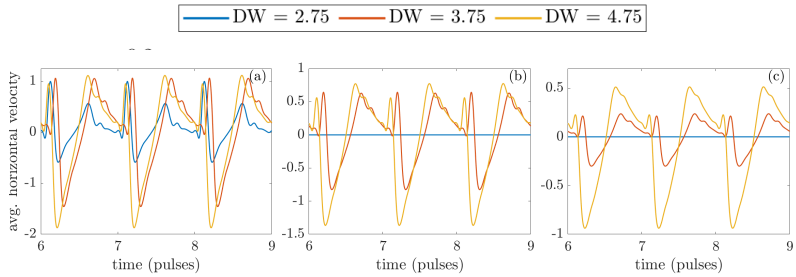

FIGURE 3.4: Average dimensionless horizontal velocities over time varying domain widths (DW) along the vertical lines presented in Fig. 3.2(a) at (a) $x = 1.25$, (b) $x = 1.5$, and (c) $x = 1.75$ for $Re = 1$. The domain height was kept constant at 9.

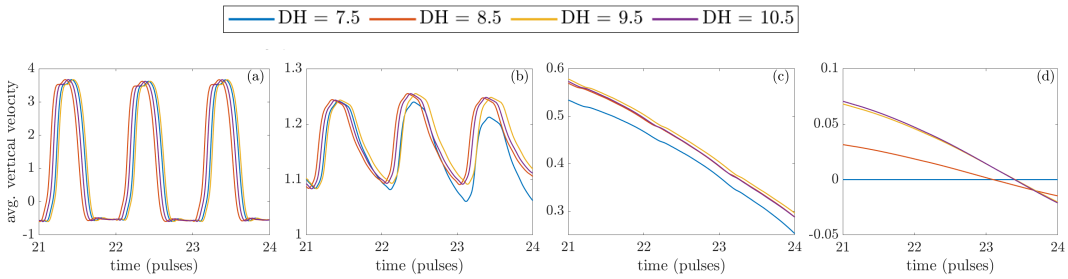

FIGURE 3.5: Average dimensionless vertical velocities over time for varying domain heights (DH) along the horizontal lines presented in Fig. 3.2(a) at (a) $y = 1$, (b) $y = 3$, (c) $y = 5$, and (d) $y = 7$ for $Re = 16$. The domain width was kept constant at 3.75

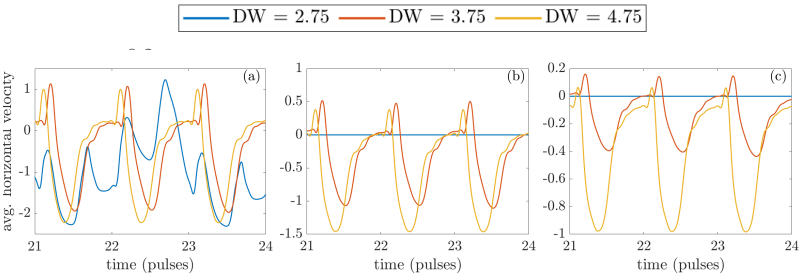

FIGURE 3.6: Average dimensionless horizontal velocities over time varying domain widths (DW) along the vertical lines presented in Fig. 3.2(a) at (a) $x = 1.25$, (b) $x = 1.5$, and (c) $x = 1.75$ for $Re = 1$. The domain height was kept constant at 9.

the transport and mixing dynamics of fluid flow [116]. The role of fluid inertia and viscosity is examined by analyzing fluid flows with varying Reynolds numbers.

A Poincaré map tracks the location of the flow trajectories after one period. In this work, the trajectory locations are tracked at the beginning of every pulse. We integrate the trajectories using a second-order Runge-Kutta scheme and interpolate the velocity using a second-order interpolation scheme, commonly used in the IB method [51].

Stable and unstable invariant manifolds of the Poincaré map are computed. A fixed point on the separatrix ($x = 0$) is computed, and a thin horizontal line of points is initialized at the fixed point to find the stable manifold. The points were mapped backward in time to compute the stable manifold using second-order Runge Kutta and a second-order interpolation scheme used in the immersed boundary method [51]. The tentacles are known to generate an unstable manifold. Points were initialized along the tentacle. The points were mapped forward in time to compute the unstable manifold. In computing both the stable and unstable manifold for each Reynolds number simulation, the number of initialized points and the number of iterations forwards or backward in time were adjusted empirically.

These manifolds define an interior and exterior region in phase space. The transport and mixing between these regions are controlled by capture and escape lobes, areas between the stable and unstable manifolds. The fluid can only pass between these regions by being mapped into or out of these lobes. The invariant manifolds and lobes of the Poincaré map provide a deeper understanding of how fluid is transported during one pulse [116].

In Fig. 3.7, the stable and unstable manifolds for Re = 1, 4, 8, 12, and 16 are presented. Half of the domain is plotted as the dynamics are symmetric across the y-axis. The interior region is denoted in light and dark green, and the exterior region is denoted in yellow and white. The quantity of interest is the amount of fluid leaving and entering the green region near the coral. This quantity gives a metric to the amount of fluid near the coral polyp replenished over a pulse. A larger amount of fluid replenished indicates more mixing, while a small amount of fluid indicates less mixing.

The area of the capture lobe (dark green) is the amount of fluid that has entered the interior region (dark green and light green) from the exterior region (white and yellow) during one pulse. The area of the escape lobe (yellow) is the amount of fluid that has escaped from the interior region. Since the fluid is incompressible, the capture and escape lobes have approximately (due to numerical error) the same area. To quantify the amount of fluid replenished in the interior region over one pulse we compute,

$$\% \text{ of the fluid entering interior region} = \frac{\text{area of capture lobe}}{\text{area of interior region}} \times 100 \ .$$

The results for all Reynolds numbers simulated are presented in Table 3.1. As the Reynolds number increases, the percentage of the fluid entering the interior region increases, indicating more mixing due to the increased inertia in the flow. Note that for $Re = 12$ and 16, there is an overlap in the capture and escape lobes. These areas are omitted in the calculation, as only the amount of fluid that has escaped and not re-entered the interior region is of interest. Observe the benefit as the Reynolds number increases between $Re = 1$, 4, and 8 compared to $Re = 8$, 12, and 16. These results indicate that the biologically relevant $Re \approx 8$ is advantageous for mixing, a result that will be observed in the concentration dynamics in Section 3.3.

TABLE 3.1: Area of interior regions, capture lobes, and percent of fluid entering the interior region.

Reynolds number	Area of interior region	Area of capture lobe	% of the fluid entering interior region
1	0.5485	0.0085	1.55
4	0.3790	0.1671	44.09
8	0.3581	0.2515	70.23
12	0.3648	0.2895	79.34
16	0.3816	0.3127	81.95

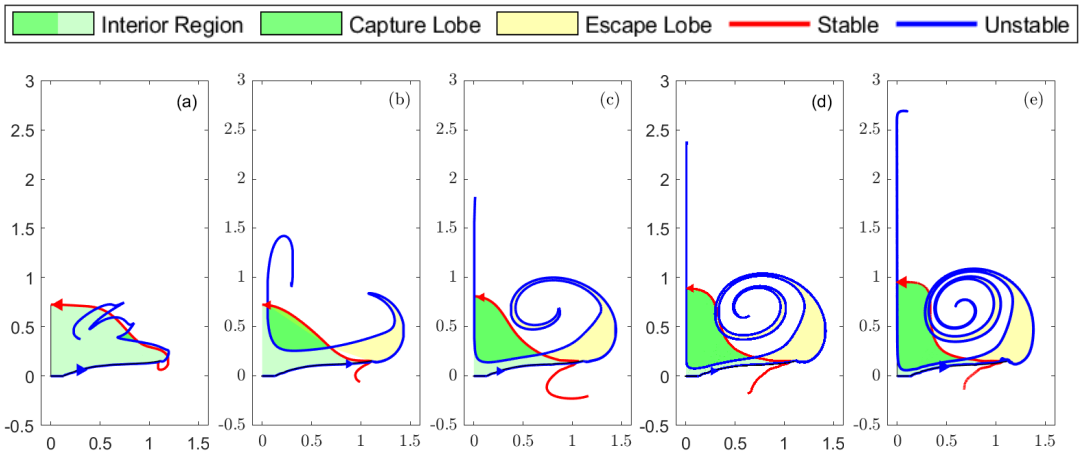

FIGURE 3.7: Analysis of Poincaré Maps for (a) $Re = 1$, (b) $Re = 4$, (c) $Re = 8$, (d) $Re = 12$, and (e) $Re = 16$. Half of the domain is presented. The stable manifold (red) and unstable manifold (blue) are plotted as well as the location of the tentacle (black). The interior regions, capture lobes, and escapes lobe are denoted with different colors.

3.3 Photosynthesis Simulations

We model the photosynthesis of the symbiotic algae using an advection-diffusion equation for the oxygen byproduct. Since the pulsing coral flow has reached a quasi-steady state and has become time-periodic, the last pulse is coupled to the oxygen concentration dynamics. A more refined grid than used in the velocity simulations is needed to resolve the oxygen concentration dynamics near the tentacles. During the final pulse for each Reynolds number, the velocity field is interpolated from a 250 $\times$ 600 grid onto a 500 $\times$ 1200 grid. The concentration is simulated for ten pulses, with no initial concentration in the domain unless otherwise stated. The Péclet number is varied in the concentration simulations coupled to each flow field. The Péclet numbers simulated are Pe = 1, 10, 100, 200, and 400 for both the constant and oxygen-limited photosynthesis models, for a total of 50 simulations. Additionally, we show some limited results from the Gaussian model, discussed below. For the oxygen concentration, the boundary conditions on the domain are periodic on the sides and no flux on the top and bottoms of the domain.

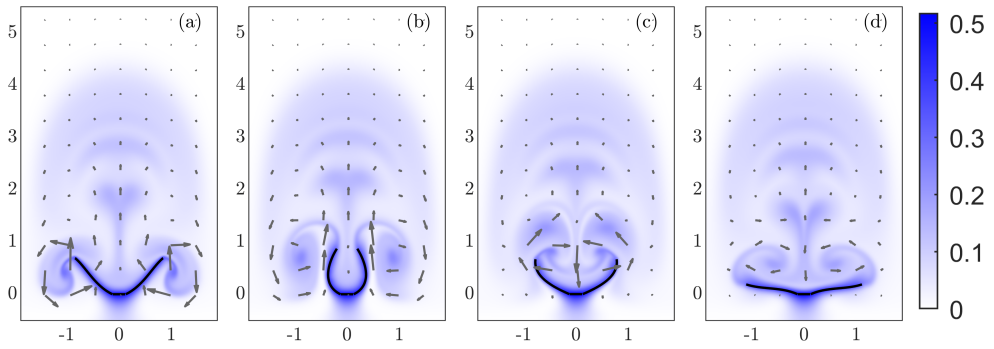

FIGURE 3.8: The concentration dynamics of the oxygen-limited model with Re = 8 and Pe = 100 at (a) 10 %, (b) 30%, (c) 50%, and (d) 80 % through the tenth pulse. The vectors give the dimensionless velocity field and the color map shows the dimensionless oxygen concentration. Note that this panel only shows a subset of the domain.

In Fig. 3.8, snapshots of the velocity field and oxygen concentration for the oxygen-limited model for Re = 8 and Pe = 100 are presented during the final pulse. Comparing these results to Fig. 3.1, it is clear that the vortices in the fluid flow trap the concentration and play an essential role in the concentration dynamics.

In Fig. 3.9, the concentration dynamics for Pe = 100 at the end of the tenth pulse for varying Reynolds numbers and the two photosynthesis models, constant and oxygen-limited, are shown. For smaller Reynolds numbers, the vortices do not develop, and the oxygen stays in the vicinity of the coral throughout the simulation, while for larger Reynolds numbers, the concentration is transported away from the

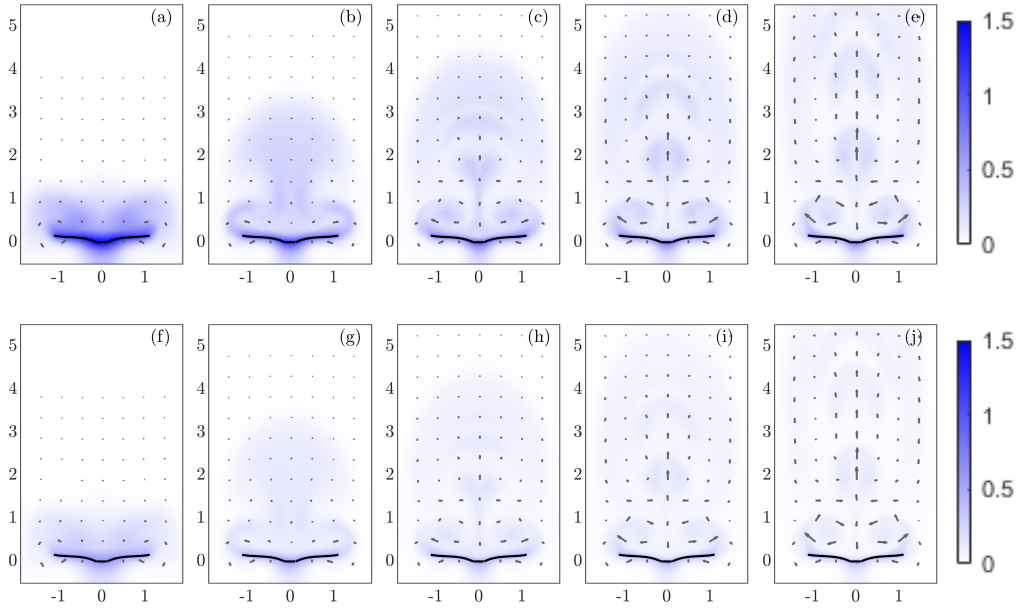

FIGURE 3.9: The concentration dynamics at the end of ten pulses for *Re* = 1, 4, 8, 12, and 16 (from left to right) for *Pe* = 100. The color map shows the dimensionless oxygen concentration for each photosynthesis model, (a)-(e) the constant model and (f)-(j) the oxygen-limited model. The vectors give the dimensionless velocity field at the final time. Note that each panel only shows a subset of the domain.

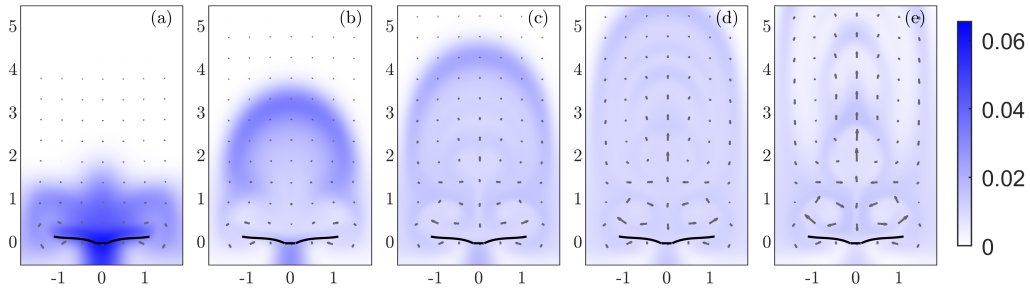

FIGURE 3.10: The concentration dynamics at the end of ten pulses for *Re* = 1, 4, 8, 12, and 16 (from left to right) for *Pe* = 100. The color map shows the dimensionless oxygen concentration for the Gaussian model. The vectors give the dimensionless velocity field at the final time. Note that each panel only shows a subset of the domain.

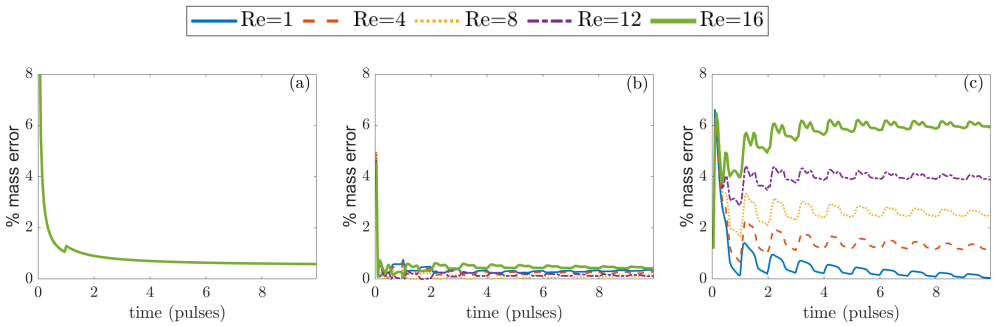

FIGURE 3.11: Relative error in the dimensionless total mass of oxygen versus time for varying Reynolds numbers for (a) $Pe = 1$, (b) $Pe = 100$, and (c) $Pe = 400$.

coral tentacles. In these cases, the concentration is trapped in the vortices pushed away from the coral. Since the constant model is not limited, more oxygen is present in the domain and a larger buildup around the tentacles.

Results where the coral tentacle is not a source of oxygen are shown at the last pulse in Fig. 3.10. The initial condition is given as:

$$c(\underline{x},0) = \int_0^{\ell} 0.1\tilde{\delta}(\underline{x}-\underline{X}(s,0))ds$$

Where $\tilde{\delta}(\underline{r}) = e^{(-(r_1)^2/\pi)}e^{(-(r_2)^2/\pi)}$ for $\underline{r} = (r_1, r_2)$. This initial condition gives a Gaussian type function defined along the coral tentacles; thus, this is called the Gaussian model. One can see that these results do not capture the results observed in Fig. 3.9 since the tentacles are not producing oxygen. Therefore it is necessary to have models and methods where the coral tentacles are a source of oxygen, The rest of this chapter will focus on the results from the constant and oxygen-limited models.

The constant model is used for validation for all Reynolds and Péclet numbers since the total amount of oxygen in the domain over time is known. In Fig. 3.11 the error over time is shown for varying Reynolds and Péclet numbers. The percent mass error is the relative mass error, defined in Chapter 2, multiplied by 100, which gives a percentage rather than a ratio. There is an initial spike in this error since there is initially very little oxygen in the domain. However, one can see that even in the high Péclet number and high Reynolds number regimes, the mass error is less than 7%. Results for $Pe = 10$ and 200 are not shown here, but the errors fall within the ranges for the cases shown in Fig. 3.11. Other numerical methods were considered and tested to discretize the advection term in Eq. (2.10), but large errors were observed in the total mass and therefore the third-order WENO scheme is chosen as it greatly improved this result.

The interesting qualitative results observed above resulted in a more quantitative analysis of the concentration dynamics to understand the interplay between the Reynolds and Péclet numbers in the two photosynthesis models. We computed several different quantities in each simulation: the maximum concentration to analyze the dynamics of the oxygen around the tentacles, the evaluation of the source term, and the average concentration in the domain to quantify how much oxygen is being produced in each parameter regime for the oxygen-limited model, the variance in the oxygen concentration as a measure of mixing, and the transport across horizontal lines at varying heights to quantify how well the oxygen is transported away in different parameter regimes.

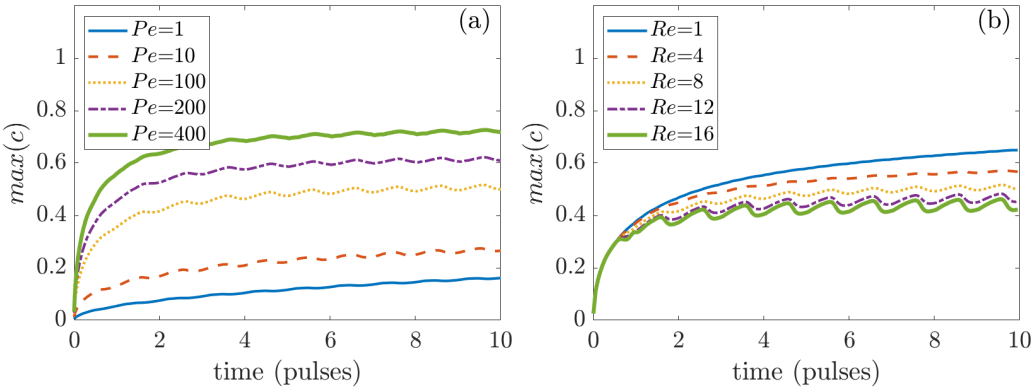

FIGURE 3.12: The maximum dimensionless concentration in the domain in the oxygen-limited model for (a) Re = 8 and varying Péclet numbers and (b) Pe = 100 and varying Reynolds numbers.

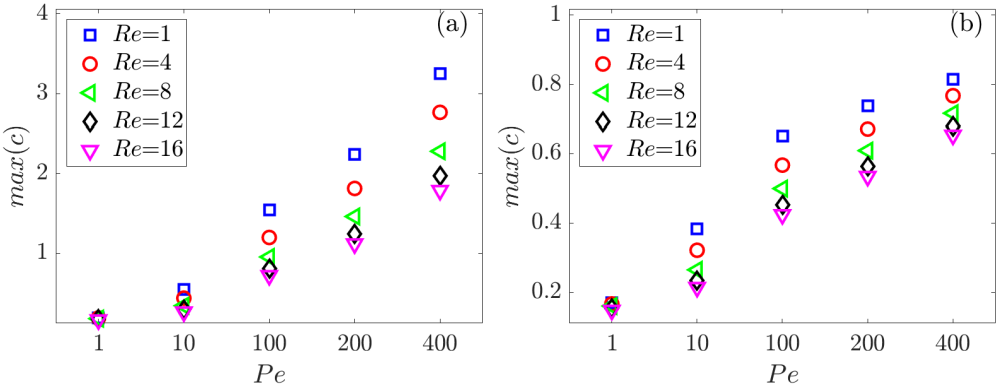

FIGURE 3.13: Maximum concentration during the final pulse for varying Péclet and Reynolds numbers for the (a) constant model and (b) oxygen-limited model.

The maximum concentration is a metric of how much oxygen concentration builds up around the tentacles and thus indicates how well oxygen is transported away from the tentacles. Less oxygen around the tentacles allows for more photosynthesis in the oxygen-limited model. The maximum concentration in the domain over time is presented in Fig. 3.12 for the oxygen-limited model. In Fig. 3.12(a) the Reynolds number is fixed as $Re = 8$ and the Péclet number is varied and in Fig. 3.12(b) the Péclet number is fixed as $Pe = 100$ and the Reynolds number is varied. In Fig. 3.12(a), as the Péclet number increases, the maximum concentration does too. This trend is consistent in time. Since a smaller Péclet number indicates a more diffusive driven flow, the concentration diffuses away from the tentacles more quickly. For a larger Péclet number, a larger accumulation of concentration is entrained in the fluid around the tentacles. In Fig. 3.12(b), as the Reynolds number increases, the maximum concentration decreases. Due to the inertia in the flow, more concentration is transported away from coral tentacles for a larger Reynolds number. The maximum concentration fluctuates more in time for larger Reynolds numbers due to the periodic pulsing. Furthermore, the difference between the maximum concentrations is more pronounced in Fig. 3.12(a), indicating that the variations in the Péclet number contribute more significantly to the transport of oxygen away from the tentacle. These quantities are reaching a quasi-steady state in time and the maximum concentration during the final pulse is given in Fig. 3.13 for $Re = 1$, 4, 8, 12, and 16 and $Pe = 1$, 10, 100, 200, and 400 for the constant and oxygen-limited models. The trends shown in Fig. 3.12 are reflected in Fig. 3.13 for varying Reynolds and Péclet numbers for both models, but note that the oxygen produced in the oxygen-limited model is significantly less. In the higher Péclet regime, there is much more variability between $Re = 1$, 4, and 8, compared to $Re = 8$, 12, and 16, which indicates that $Re = 8$ is advantageous for mixing in the high Péclet regime. Since $Re \approx 8$ and $Pe \approx 400$ are the biologically relevant parameters, these results suggest that the corals operate in a desirable mixing regime.

The evaluation of the source term in the oxygen-limited model,

$$S(t) = \int_{\Gamma} \kappa(1-C)\delta(\underline{x} - \underline{X}(s,t))d\underline{s} \ ,$$

shown in Fig 3.14, is proportional to the amount of photosynthesis occurring by the symbiotic algae in this model. Similarly, the spatial average of the concentration, presented in Fig. 3.15, is a measure of the amount of oxygen in the domain,

$$\langle c(t) \rangle = \frac{\int_{\Omega} c(\underline{x},t)d\underline{x}}{\int_{\Omega} d\underline{x}} \ .$$

Both of these quantities allow one to study which parameters lead to more photosynthesis occurring.

The evaluation of the source term, Fig. 3.14(a), and the spatial average of concentration, Fig. 3.15(a), over time, is presented for $Re = 8$ and varying Péclet numbers for the oxygen-limited model. As the Péclet number increases, the amount of oxygen produced decreases since there is an accumulation of the concentration around the tentacle, as seen in Fig. 3.12(a), inhibiting the production of more oxygen. The oscillations of the source term for larger Péclet numbers are also consistent with the oscillations of the maximum concentration in Fig. 3.12(a), showing that the flow field is contributing more to the dynamics in the large Péclet number regime. The evaluation of the source term, Fig. 3.14(b), and the spatial average of concentration, Fig. 3.15(b), is presented over time for $Pe = 100$ and varying Reynolds number for the oxygen-limited model. As the Reynolds number increases, more oxygen is produced as the inertia in the fluid advects the oxygen away from the tentacles, as seen in Fig. 3.12(b), allowing more photosynthesis to occur.

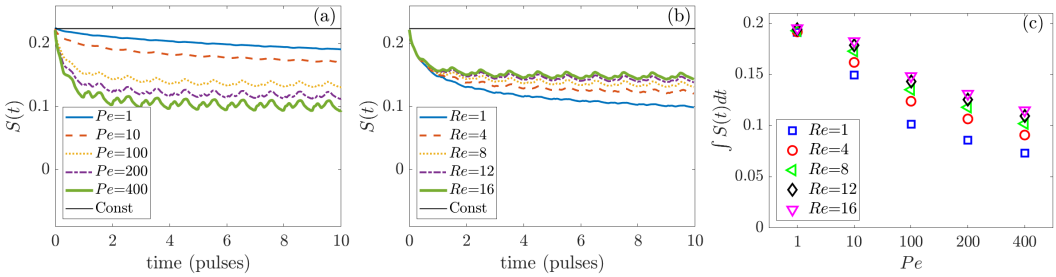

FIGURE 3.14: Evaluation of the source term over time in the oxygen-limited model for (a) Re = 8 and varying Péclet numbers and (b) Pe = 100 and varying Reynolds numbers. (c) The total dimensionless oxygen produced during the tenth pulse for varying Péclet and Reynolds numbers.

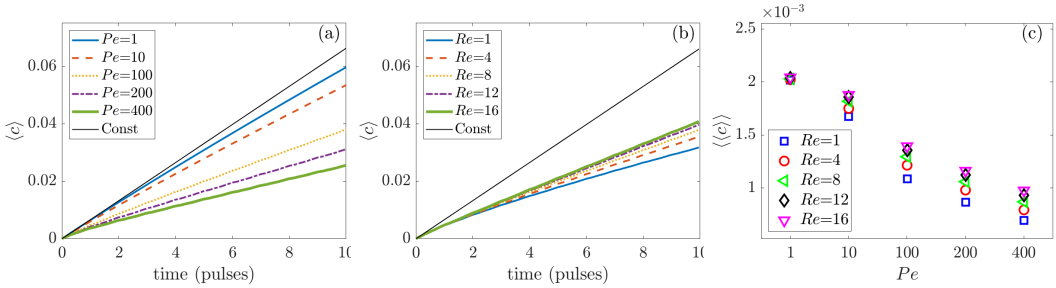

FIGURE 3.15: Spatial average of the dimensionless concentration in the domain over time for the oxygen-limited model for (a) Re = 8 and varying Péclet numbers and (b) Pe = 100 and varying Reynolds numbers. (c) Spatial and temporal average of the dimensionless concentration in the domain during the tenth pulse for varying Péclet and Reynolds numbers.

In Fig. 3.14(c), the source term is integrated in time over the tenth pulse for each Reynolds and Péclet number to evaluate the total amount of oxygen produced during

the final pulse. The spatial and temporal average of the oxygen concentration in the domain over the tenth pulse is presented in Fig. 3.15(c). The amount of oxygen produced and average concentration decreases with increasing Péclet number and increases with increasing Reynolds number. The difference in the Péclet numbers affects oxygen production more so than the difference in Reynolds number, which is consistent with the observation in the maximum oxygen concentration. For small Péclet numbers, the results are very similar over varying Reynolds numbers, while for the larger Péclet numbers, the average concentration and oxygen produced are more dependent on the Reynolds number. In both Fig. 3.14(c) and Fig. 3.15(c), it is observed that the amount of oxygen produced in the high Péclet number regime is similar for Re = 8, 12, and 16, and considerably less for Re = 1 and 4, again indicating that the biologically relevant Reynolds number, $Re \approx 8$, is an efficient choice for photosynthesis when the Péclet number is large. These trends were also reflected and noted in Fig. 3.12(c).

The next quantity presented and discussed is the concentration variance,

$$var(c) = \sqrt{\int_{\Omega} (c(\underline{x},t) - \langle c(t) \rangle)^2 d\underline{x}} \, ,$$

a measure of how mixed the system is [117]. To be able to compare between models with varying parameters and different amounts of oxygen present in the domain the adjusted variance is used,

$$adjvar(c) = \sqrt{\int_{\Omega} \left(\frac{c(\underline{x},t)}{\langle c(t) \rangle} - 1 \right)^2 d\underline{x}} \, .$$

Ideal mixing would be when the oxygen is mixed into the domain from the tentacle to a steady state instantaneously, $c(\underline{x},t) = \langle c(t) \rangle$ and $adjvar(c) = 0$. The adjusted variance of the concentration gives a measure of how far away the solution is from this ideal mixing which takes the role of oxygen diffusion into account, unlike the analysis of the fluid flow conducted above. The temporal average of the concentration variance during the final pulse for all Reynolds and Péclet numbers is given in Fig. 3.16 for the constant and oxygen-limited models. Smaller Péclet numbers have lower variance values, suggesting that diffusion is an ideal mixer compared to advection. For larger Péclet numbers, larger Reynolds numbers have more mixing. This result is consistent with the previous metrics that indicated more mixing with larger Reynolds numbers. The benefit from Re = 1 to 4 and Re = 4 to 8 is considerable, but there seems to be less benefit between Re = 8 and 12 and Re = 12 and 16. These larger Reynolds numbers result in more energy being expended. Since $Re \approx 8$ and $Pe \approx 400$ are the biologically relevant parameters, these results suggest that the corals operate in a desirable mixing regime without expending extra energy. This result indicates that the biologically relevant parameters are also advantageous

for mixing in addition to photosynthesis. These results are intuitive, Figs. 3.13(b) and 3.14(c) showed that for small Péclet numbers, less oxygen is built up around the tentacles resulting in more oxygen production and that in the high Péclet number limit, larger Reynolds number have less oxygen buildup around the tentacles and more oxygen production. These results show that the adjusted variance metric captures the mixing trends through the lens of photosynthesis and oxygen production.

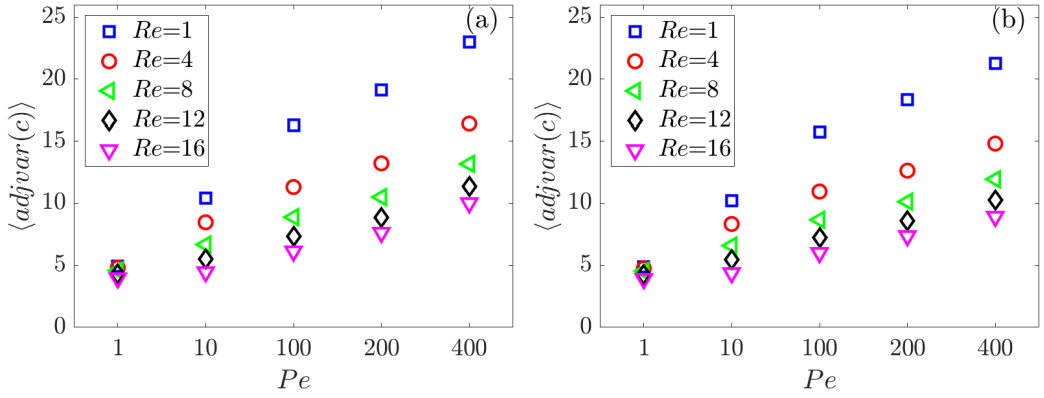

FIGURE 3.16: Temporal average over the last pulse of the dimensionless adjusted concentration variance in the domain for the (a) constant and (b) oxygen-limited models.

Another useful way of analyzing the photosynthesis dynamics is quantifying how far away the oxygen is transported from the coral. This metric will take into account the role of the fluid flow away from the corals, which is relevant to understanding coral colony dynamics. The previous results presented focused on the dynamics closer to the coral polyps, which are more relevant to individual polyps. We consider a box B in the domain that spans the width of the domain, starts at $y = y_o$ and ends at the top of the domain. Then, the amount of oxygen in that box at time t is $\int_B c(\underline{x},t)d\underline{x}$ and the amount of oxygen leaving and entering the box is,

$$\int_B \nabla \cdot (c(\underline{x},t)\underline{u}(\underline{x},t))\, d\underline{x} = \int_{\partial B} (c(\underline{x},t)\underline{u}(\underline{x},t)) \cdot \underline{n}\, dS \ .$$

Since the sides of the box are periodic boundaries and the top of the box has a no flux boundary condition, the only part of the box where oxygen enters and exits is through $y = y_o$. Thus, the amount of oxygen in B at time t is defined as,

$$c_B(y_o,t) = \int_0^t \int_{-1.875}^{1.875} c(x,y_o,t')u_2(x,y_o,t')\ dx\ dt' \ ,$$

since there is no initial oxygen in B. The limits -1.875 and 1.875 show that we are integrating over the width of the domain. This equation also gives the total net

amount of oxygen that has passed through the line $y = y_0$ by time t. To compare between simulations, the percentage of oxygen in B of the total oxygen in the domain at time t is computed as

$$\%c_B(y_o,t) = \frac{c_B(y_o,t)}{\int_\Omega c(\underline{x},t)d\underline{x}} \times 100 \ .$$

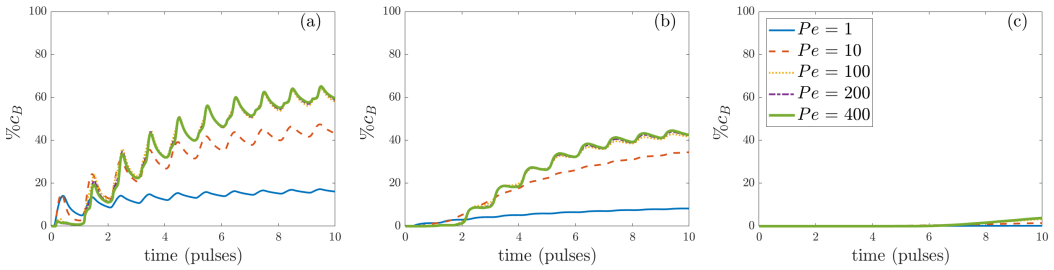

FIGURE 3.17: Percentage oxygen in B over time, given in dimensionless form, for Re = 8, with varying Péclet numbers for (a) $y_o = 1$, (b) $y_o = 2$, and (c) $y_o = 4$.

The results presented are for the oxygen-limited model. These quantities were also computed for the constant model. However, the behavior is similar to the oxygen-limited results, so they are omitted here. The dynamic results with Re = 8 and varying Péclet numbers are shown in Fig. 3.17 for y_o = 1, 2, and 4. For y_o = 1, the box starts right above the tips of the coral tentacles when fully contracted, y_o = 2 is one tentacle length above the fully contracted coral polyp, and y_o = 4 is three tentacle lengths above the fully contracted coral polyp. The percentage of oxygen in the box when y_o = 1, Fig. 3.17(a), is smaller for Pe = 1 and stays relatively steady. This is because the concentration has diffused from the coral, and the upward flow is not affecting the dynamics. For larger Péclet numbers, the percentage increases with fluctuations due to the flow and reaches a periodic steady state. These dynamics are similar in Fig. 3.17(b), the percentage of oxygen in the box when $y_o = 2$. There is a smaller percentage of oxygen in this box compared to when y_o = 1 since the bottom of the box is farther away from the top of the pulsing coral. In Fig. 3.17(c) there is a very small percentage of concentration in the domain when y_o = 4. In the large Péclet number regime, the concentration does not accumulate directly above the coral. Rather the concentration is transported away from the coral for these biologically relevant parameters. Additionally, the dynamics in Fig. 3.17 show that for all Péclet numbers the majority of the concentration above the coral is between y_o = 2 and y_o = 4. The majority of the oxygen is transported within about three tentacle lengths away from the coral.

A similar analysis for Pe = 100 and varying Reynolds numbers is shown in Fig. 3.18. The percentage in the box when y_o = 1 for the varying Reynolds numbers are

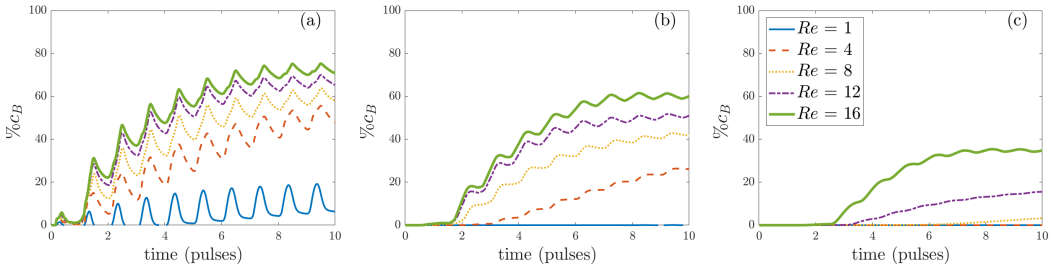

FIGURE 3.18: Percentage dimensionless oxygen in B over time for Pe = 100, with varying Reynolds numbers for (a) $y_o = 1$, (b) $y_o = 2$, and (c) $y_o = 4$.

shown in Fig. 3.18(a). Reversible flow is present for Re = 1, resulting in very little net transport away from the coral. As the Reynolds number increases, more oxygen is transported across y_o = 1, with the oscillations corresponding to the coral pulsing. This behavior is also seen in Fig. 3.18(b), where y_o = 2, for Re = 4, 8, 12, and 16. However, as seen in Fig. 3.17, the percentages are smaller since the bottom of the box is farther away from the coral. For Re = 1, the percentage is close to zero, showing the lack of transport away from the coral. In Fig. 3.18(c) where y_o = 4, the percentage of oxygen in B is close to zero for Re = 1 and 4. For Re = 8, 12, and 16, there is an increasing amount of oxygen in B, respectively. This shows that in these higher inertia regimes that the flow has advected a significant amount of the oxygen up to three tentacle lengths away from the coral.

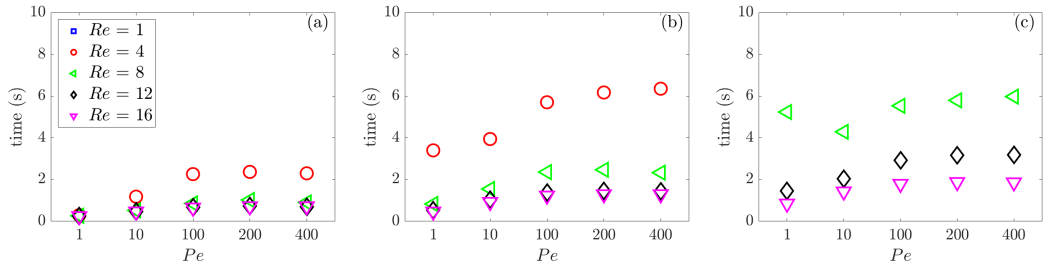

FIGURE 3.19: Dimensionless time to non-zero percentage of oxygen in B when (a) $y_o = 2$, (b) $y_o = 3$, and (c) $y_o = 4$.

In Figs. 3.17 and 3.18 there is a lag time until the percentage of oxygen is noticeably greater than zero when y_o = 2 and 4. Although our interest is the long-term steady-state behavior of the system, computing the time it takes for the percentage of concentration to be larger than zero shows the time it takes to transport oxygen away from the coral. In Fig. 3.19, this is shown for y_o = 2, 3, and 4 for all Reynolds and Péclet numbers, with a tolerance of 0.1%. For Re = 1, the oxygen percentage is never greater than the tolerance showing a lack of oxygen transport away from the coral. For Re = 4, it takes approximately one to two pulses to exceed the tolerance

when $y_o = 2$, four to six pulses when $y_o = 3$, and never exceeds the tolerance for $y_o = 4$. For $Re = 8$, 12, and 16 the tolerance is exceeded for $y_o = 2$ within the first pulse. For larger y_o, we see shorter lag times for larger Reynolds numbers.

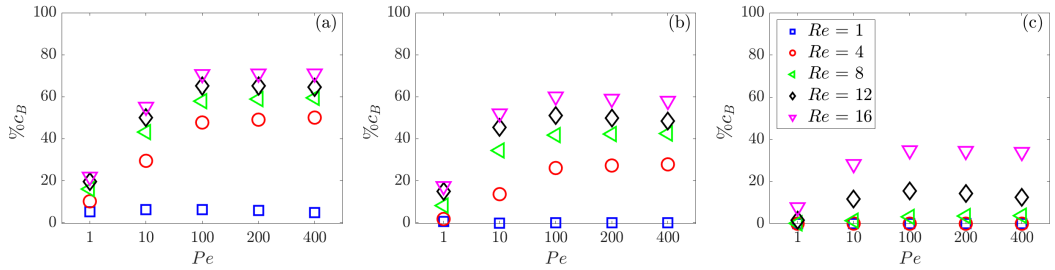

FIGURE 3.20: Total percentage of oxygen in B at the end of the final pulse when (a) $y_o = 1$, (b) $y_o = 2$, and (c) $y_o = 4$.

The long-term behavior of transport of oxygen away from the tentacles is shown in Fig. 3.20. The total percentage of oxygen in the box at final time $t = 10$ is shown for $y_o = 1$, 2, and 4 for all Reynolds and Péclet numbers. For $Re = 1$, the percentage is small when $y_o = 1$, and close to zero when $y_o = 2$ and 4, for all Péclet numbers. This result is consistent with previous results showing that the mixing in this regime is limited directly around the coral tentacles. As the Reynolds number increases, the percentage of oxygen in these boxes increases due to the upward flow observed in previous results. As the Péclet number increases, the percentage in the boxes increases for $Pe = 1$, 10, and 100, but plateaus after Pe =100. This regime is more advective driven and is more influenced by the upward flow than for smaller Péclet numbers, which diffuse quickly away from the coral tentacles but are not transported upward. The advective transport upward rather than diffusive driven radial transport could be advantageous for coral colonies. The upward transport could result in less recirculation of oxygen-rich water by neighboring polyps. For the larger biologically relevant Péclet numbers, there are differences between the results when comparing the Reynolds numbers and y_0 values. For $y_o = 1$, we can see more variability between $Re = 1$ and 4, and much less variability between $Re = 4$, 8, 12, and 16. For $y_o = 2$, we can see more variability between $Re = 1$, 4, and 8, and much less variability between $Re = 8$, 12, and 16. For $y_o = 4$, we can see more variability between $Re = 12$ and 16, and much less variability between $Re = 1$, 4, 8, and 12. This result shows that $Re = 4$ is advantageous for transporting oxygen a short distance, but $Re = 8$ is advantageous for transporting up to a coral length away, and Re =16 is advantageous for transporting oxygen up to three coral lengths away. From the previous analysis, we know that $Re = 8$ is advantageous for mixing and more photosynthesis, indicating that transporting oxygen a tentacle length away is enough to facilitate photosynthesis and prevent fluid recirculation by neighboring polyps.

This chapter shows the pulsing coral fluid flow results coupled to different photosynthesis models, focusing on the oxygen-limited model. The mixing due to the

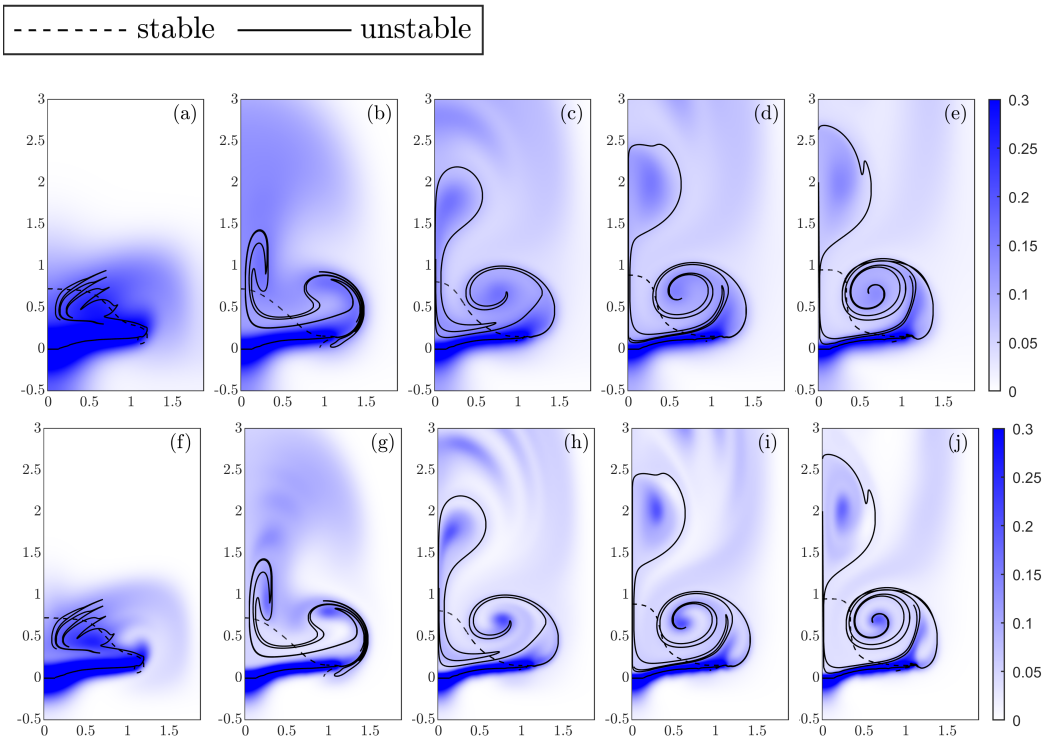

FIGURE 3.21: Dimensionless oxygen concentration for the oxygen-limited photosynthesis model at the end of ten pulses for (a)-(e) $Pe = 100$ and (f)-(j) $Pe = 400$ for varying Reynolds numbers, (a,e) $Re = 1$, (b,g) $Re = 4$, (c,h) $Re = 8$, (d,i) $Re = 12$, and (f,j) $Re = 16$ overlaid with the corresponding stable (dashed) and unstable (solid) manifolds. Half of the domain is presented.

flow is examined for varying Reynolds numbers in Section 3.2. The photosynthesis model is quantitatively analyzed for varying Reynolds and Péclet numbers by observing the maximum oxygen concentration, the evaluation of the oxygen-limited source term, the average oxygen concentration in the domain, the adjusted variance of the oxygen concentration, and the transport of oxygen away from the coral tentacles. We have presented results that have studied the dynamics of a fixed Reynolds number and varied Péclet number and vice versa. When both numbers are simultaneously varied, this is equivalent to varying the Schmidt number $Sc = \frac{\nu}{D}$, the ratio of fluid viscosity to diffusivity. Fig. 3.22 shows the maximum concentration as a function of the Schmidt number. One can observe a general trend of increasing maximum concentration with increasing Schmidt number. Recalling that smaller Schmidt numbers correspond to oxygen concentration dynamics that are diffusion driven. We chose to vary the Reynolds and Péclet numbers independently to get a more in depth understanding of the dynamics. When investigating the interaction of the Reynolds and Péclet number, we have found advantageous parameter regimes for mixing, photosynthesis, and oxygen transport by analyzing these results.

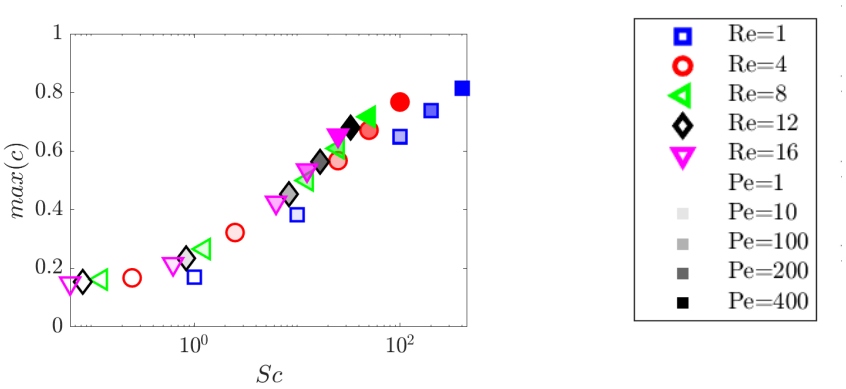

FIGURE 3.22: Maximum dimensionless oxygen concentration as a function of the Schmidt number. The corresponding Reynolds and Péclet numbers are denoted with shapes and shading, respectively.

Fig. 3.21 ties together the fluid flow mixing analysis and photosynthesis modeling results. The oxygen concentration after ten pulses for *Pe* = 100 and 400 and varying Reynolds numbers are shown overlaid with the corresponding steady and unsteady manifolds of the fluid flow. The higher Péclet regime best shows agreement between the Poincaré map manifolds and the oxygen dynamics, as expected. For *Re* = 1, most of the oxygen stays within the interior region and is not transported away. For the larger Reynolds numbers, the oxygen moves out of the interior region to the escape lobe (which corresponds to vortices in the flow) and into other subsequent lobes in the domain.

The effect of diffusion and the source term on these dynamics can be observed. In these results, the Péclet number is constant in (a)-(e) and (f)-(j). However, if the Péclet number had been defined using the maximum flow velocity, rather than the pulsing frequency, then (a) and (f) would have a smaller Péclet number than (e) and (j). In these dynamics, (a) and (f) are more diffusive, so the manifolds do not give as much information as (e) and (j). The algae produce oxygen on both sides of the tentacle. The oxygen produced from the underside of the tentacle is not in the interior region, so the oxygen dynamics can only partially be explained by the Poincaré map lobes. These results show that it is necessary to model the concentration dynamics to understand how the mixing facilities the photosynthesis of the symbiotic algae. However, both techniques provide useful and relevant information into the mixing dynamics of the pulsing soft corals and the photosynthesis of their symbiotic algae.

3.4 Discussion Of Two-Dimensional Modeling, Numerical Methods, And Results

In this work, a new mathematical model and numerical method is developed in two dimensions to study the fluid flow of a pulsing soft coral coupled with the photosynthesis of symbiotic algae. The fluid flow of the pulsing soft corals is solved for using the immersed boundary method, and photosynthesis is modeled by solving an advection-diffusion equation for oxygen, the byproduct of photosynthesis. Included in the advection-diffusion equations is a source term on the moving tentacles to model oxygen production by the symbiotic algae. The mixing due to fluid flow is analyzed using a dynamical systems approach by applying dynamical systems techniques. Photosynthesis and mixing dynamics were quantitatively analyzed using the maximum oxygen concentration, the evaluation of the oxygen-limited source term, the average oxygen concentration in the domain, the adjusted variance of the oxygen concentration, and the transport of oxygen away from the coral tentacles for varying Reynolds and Péclet numbers. The novelty of this work is including a photosynthesis model coupled with fluid-structure interaction. This novelty required developing a method to solve a partial differential equation with a boundary condition on a moving immersed elastic boundary.

In the analysis of the fluid flow, the larger Reynolds numbers produced more mixing, as expected. The benefit from the larger Reynolds number lessens right around the biologically relevant Reynolds number, which is determined by the kinematics of the pulsing coral. The benefit of mixing and oxygen concentration variance with respect to the energy expended by the coral in the fluid simulations will be included in the manuscript related to this work [104]. The other primary numerical study on soft coral flow dynamics around a single coral polyp used Lagrangian Coherent Structures and Finite-Time Lyapunov exponents to examine mixing [14]. A similar methodology is presented on PIV flow fields to study the feeding habits of jellyfish [94]. These methods are useful for qualitative analysis for regions of high or low mixing in unsteady flow. The methodology presented in this work instead can give quantitative results for varying Reynolds numbers. This methodology allows for a quantitative metric for mixing rather than qualitative results.

The next step of this work is to apply this novel methodology in three dimensions, presented in Chapters 5. From prior work, it is already known that the fluid flow has characteristics that cannot be captured in two dimensions [14].

Chapter 4

Implementation in `IB2d`

`IB2d` is an open-source two-dimensional MATLAB and Python implementation of the immersed boundary method [118]. The user-friendly architecture allows students and researchers to bypass the steep learning curve to understand the immersed boundary method and fluid-structure interaction problems. In addition to the traditional immersed boundary method, the code has other more advanced capabilities used in immersed boundary fluid-structure interaction problems, including muscle models, invariant beams, tracers, and a Boussinesq approximation, and the addition of a background concentration in the flow [69], [118], [119]. In this chapter, the methodology implemented in `IB2d` to have the immersed boundary act as a sink or source of the concentration is discussed.

The work developed in Chapter 2 is contributed to this open-source code. In addition to the inclusion of the immersed boundary acting as a source or a sink of the background concentration, we contributed the capability of solving the advection component of the advection-diffusion equation using a third-order WENO scheme [114]. The motion of the coral from Chapter 2 is added into `IB2d` as an example that utilizes the new methodology. The challenge in this work is blending the new methodology into the existing framework.

In the `IB2d` library, the functions that advance the solution and the problem-specific applications are separate. The functions that advance the simulation are found in the IBM BlackBox directory, while the framework for the different examples is in the Example directory. In the IBM BlackBox directory, the contributions were the advection-diffusion solver with a sink or source term, the functions which defined the sinks or sources on the immersed boundary, and the third-order WENO advection scheme. In the Example directory, two examples were added for this framework: a standard rubber band that acted as a source or sink for a concentration, used in a convergence study to validate the methodology, and a single coral polyp with the motion presented in Chapter 2, where the coral tentacles acted as a source for the concentration. Other collaborators added examples of an appendage sniffing and heat dissipation on a leaf.

In this chapter Section 4.1 will give the mathematical modeling contributed to `IB2d`. Section 4.2 will overview the corresponding numerical methods. Section 4.3 will present the convergence study of the canonical immersed boundary problem, a

rubber band. Section 4.4 will show a simulation with the coral motion from Chapter 2 implemented in `IB2d`. In Section 4.5 the chapter is summarized and the impact of this work is discussed. This work has led to a paper that has been submitted [120].

4.1 Mathematical Model

The background concentration, already implemented in `IB2d`, $c(\underline{x},t)$ is governed by the dimensional advection-diffusion equations

$$c_t + \underline{u} \cdot \nabla c = D\nabla^2 c \tag{4.1}$$

where $\underline{u}(\underline{x},t) = (u_1, u_2)$ is the velocity from the fluid-structure interaction, and D is the diffusion coefficient. The quantities introduced in Chapter 2 and 3 are dimensionless. However, in this chapter, the quantities will be dimensional, as `IB2d` is a dimensional code.

`IB2d` uses the immersed boundary method, which has been discussed in Chapter 2. The contribution to this work is adding the immersed boundary acting as a source or sink of the concentration, which will be the focus of this chapter. The advection-diffusion equation, for concentration $c(\underline{x},t)$, is then given as,

$$c_t + \underline{u} \cdot \nabla c = D\nabla^2 c + \int_0^\ell \tilde{f}(s,t)\delta(\underline{x} - \underline{X}(s,t))ds \ ,$$

where $\underline{x}$ denotes Cartesian points in the fluid domain, $\underline{X}(s,t)$ denotes the Lagrangian points on the immersed boundary, and $\tilde{f}(s,t)$ is the sink or source model with units of amount of chemical per length per time defined for arclength $0 \leq s \leq \ell$ at time t. There are three models included in this framework, the first two are presented in Chapter 2, and the third is a newer implementation,

$$\tilde{f}(s,t) = \kappa \ , \tag{4.2}$$

$$\tilde{f}(s,t) = \kappa(C_\infty - C(s,t)) \ , \tag{4.3}$$

$$\tilde{f}(s,t) = \kappa C(s,t) \ , \tag{4.4}$$

where $C(s,t) = \int_\Omega c(\underline{x},t)\delta(\underline{x} - \underline{X})d\underline{x}$. The constant κ is an absorption constant when given a negative value and a desorbtion constant when given a positive value. In Eq. (4.2) the units of κ are the amount of chemical per length per time, and in Eqs. (4.3) and (4.4) the units of κ are length per time. C_∞ is the saturation limit of the concentration.

As before in Chapter 2, Eq. (4.2) is referred to as the constant model, where the boundary produces a constant amount of concentration over time. Eq. (4.3) is referred to as the limited model. Since C_∞ is the saturation limit of the concentration, in this model, the amount of concentration produced by the boundary is dependent

on the amount of concentration locally around the immersed boundary. Eq. (4.4) is referred to as the reaction model. As the boundary moves through the fluid, the amount of concentration produced or absorbed is directly proportional to the concentration present locally. These models can theoretically be used as a sink or source by changing the sign of κ depending on the specific application. The limited model will be used as a source model in this work, and the reaction model will be used as a sink model.

4.2 Numerical Methods

The original advection-diffusion scheme for Eq. (4.1) implemented in `IB2d` is fully explicit and first order. The velocities solved for from the fluid-structure interaction, $u(\underline{x},t) = (u_1, u_2)$, are used to advect the background concentration $c(\underline{x},t)$. The concentration, c^{n+1}, at time t^{n+1} are updated using forward Euler,

$$c^{n+1} = c^n + \Delta t \left(-({u_1}^n \tilde{c}_x^n + {u_2}^n \tilde{c}_y^n) + D\nabla_h^2 c^n \right) \tag{4.5}$$

for time step Δt. The derivatives $\tilde{c}_x$ and $\tilde{c}_y$ are found using a first-order upwind method using the fluid velocities and concentration at time t^n. Here ∇_h^2 refers to the standard second order finite-difference Laplacian operator.

This method is now updated to incorporate the immersed boundary as a source or sink of a concentration and allow for more accuracy in the advective terms. Both of these have new user-defined inputs. The methodology is updated as,

$$c^{n+1} = c^n + \Delta t \left(-({u_1}^n \tilde{c}_x^n + {u_2}^n \tilde{c}_y^n) + D\nabla_h^2 c^n + \sum_{k=1}^{k=N} \tilde{f}_k^n \delta_h(\underline{x} - \underline{X}_k^n)\Delta s \right) , \tag{4.6}$$

where $\tilde{c}_x^n$ and $\tilde{c}_y^n$ are found using either the first-order upwind method or the third-order WENO method depending on the user-defined input. Here $\tilde{f}_k^n$ is the discrete analog of the sink or source model. For the three models corresponding to Eqs. (4.2)-(4.4) they are defined as $\tilde{f}_k^n = \kappa$, $\tilde{f}_k^n = \kappa(C_\infty - C_k^n)$, and $\tilde{f}_k^n = \kappa C_k^n$, respectively. Recall in the limited and reaction model $C(s,t)$ is the local concentration interpolated onto the boundary. Numerically, this is discretized using the trapezoid rule,

$$C_k^n = \sum_{ij} c_{ij}^n \delta_h(\underline{x}_{ij} - \underline{X}_k^n)\Delta x \Delta y$$

Making these additions led to further modifications in the `IB2d` library. The source or sink term in Eq. (4.6) is analogous to the force spreading interaction equation in the IB method,

$$\int_o^\ell \tilde{f}(s,t)\delta(\underline{x} - \underline{X}(s,t))ds \ .$$

The original implementation discretized this equation as,

$$\sum_{k=1}^{k=N} \tilde{f}_k^n \delta_h(\underline{x} - \underline{X}_k^n)\Delta s \ , \tag{4.7}$$

assuming a closed boundary. If $\tilde{f}(s,t) = \kappa$ is constant and there is no initial concentration in the domain then we expect the total mass in the domain at time t to be,

$$\int_0^t \int_0^\ell \kappa \delta(\underline{x} - \underline{X}(s,t'))dsdt' = \kappa \int_0^t L(t')dt' \ .$$

Where $L(t)$ is the length of the curve at time t. However, in practice, Eq. (4.7) is only valid for an immersed boundary with a fixed length. This condition is due to the assumption that the distance between points is fixed at Δs. For small deformations, this is a good approximation. If this method is used for applications that resulted in large deformations in the immersed boundary, there would be issues in the conservation of total mass. A more robust method is desired for `IB2d`. Therefore, we added a different discretization for Eq. (4.7),

$$\sum_{k=1}^{N-1} \frac{1}{2}(\tilde{f}_k^n \delta_h(\underline{x} - \underline{X}_k^n) + \tilde{f}_{k+1}^n \delta_h(\underline{x} - \underline{X}_{k+1}^n)) \ || \ \underline{X}_{k+1}^n - \underline{X}_k^n \ ||_2 \tag{4.8}$$

for open curves and

$$\sum_{k=1}^{N} \frac{1}{2}(\tilde{f}_k^n \delta_h(\underline{x} - \underline{X}_k^n) + \tilde{f}_{k+1}^n \delta_h(\underline{x} - \underline{X}_{k+1}^n)) \ || \ \underline{X}_{k+1}^n - \underline{X}_k^n \ ||_2 \tag{4.9}$$

for closed curves, where $\underline{X}_{N+1} = \underline{X}_1$. This new discretization is implemented for the force spreading interaction equation in the immersed boundary method and for the source or sink term in Eq. (4.6). This work was developed jointly with collaborators Shilpa Khatri, Laura Miller, and Nicholas Battista, and implementation for the discretization in `IB2d` was implemented by Khatri and Battista.

4.3 Convergence

In order to validate the methodology implemented in `IB2d`, a convergence study is conducted on a canonical immersed boundary example, a Hookean rubber band. The initial configuration of the rubber band is an ellipse given by,

$$X_1 = 0.5 + a\cos(s)$$
$$X_2 = 0.5 + b\sin(s)$$

for $0 \leq s \leq 2\pi$, with a = 0.4, and b = 0.2. The fluid flow is solved on an $[0,1] \times [0,1]$ domain with periodic boundary conditions and is initially at rest.

The fluid grid is discretized with Nx = 32, 64, 128, 256, and 512 points and grid size $h = \frac{1}{Nx}$. The number of points to discretize the rubber band are given by $N = \lceil 4\pi\sqrt{ab}Nx \rceil$. The time step corresponding to gridsize h is $\Delta t = \frac{h}{62.5}$ and the simulation is run until final time $t = 2$. The Hookean spring constants for the immersed boundary were set to $k_s = \frac{10^5}{64^2}Nx^2$.

The errors in the convergence studies are computed in the same way as in Section 2.2.1, where the error at mesh width h, for a quantity Q_h is approximated as $Q_h - Q_{h/2}$. The computation of the mass in the domain is computed differently to take the new methodology into account. The exact mass in the domain at time t when using the constant model is given by,

$$M(t) = \int_0^t \int_0^\ell \kappa\delta(\underline{x} - \underline{X}(s,t'))dsdt' = \kappa \int_0^t L(t')dt' \ .$$

When the length of the immersed boundary is fixed, $L(t) = L$, this integral simplifies to $M(t) = \kappa L$. However, when the length of the immersed boundary varies in time the total mass is given by.

$$M(t) = \kappa \int_0^t L(t')dt' \ ,$$

which is approximated using the trapezoidal rule.

The convergence results for the concentration when using the constant source model and the upwind scheme for the advective terms with $D = 10^{-2}$ m^{2}s^{-1} and $\kappa = 0.1$ mol m^{-1}s^{-1} are given in Table 4.1. The convergence results when using the WENO scheme instead are given in Table 4.2. The concentration initial condition is $c(\underline{x}, 0) = 0$ mol m^{-2}. Fig. 4.1 shows snapshots of this simulation at the most refined grid, Nx = 512. One can see that the convergence study results are similar between the two methods and are approaching first order as expected. However, there is a clear benefit of the WENO method in the total mass error. The WENO method gives an order of magnitude improvement in mass error compared to the upwind method. Given these results, convergence results for the two additional models will be presented when using the WENO scheme for the advection term.

The convergence results for the concentration when using the limited source model and the WENO scheme for the advective terms with $D = 10^{-2}$ m^{2}s^{-1}, $C_\infty =$ 1 mol m^{-2}, and $\kappa = 0.1$ ms^{-1} are given in Table 4.3. The concentration initial condition is $c(\underline{x}, 0) = 0$ mol m^{-2}. Fig 4.2 shows snapshots of this simulation at the most refined grid, Nx = 512. Notice that since the total mass in the domain for this case is unknown, the error for the total mass is computed using the grid refinement as for the concentration error.

The convergence results for the concentration when using the reaction sink model and the WENO scheme for the advective terms with $D = 10^{-2}$ m^{2}s^{-1} and $\kappa =$

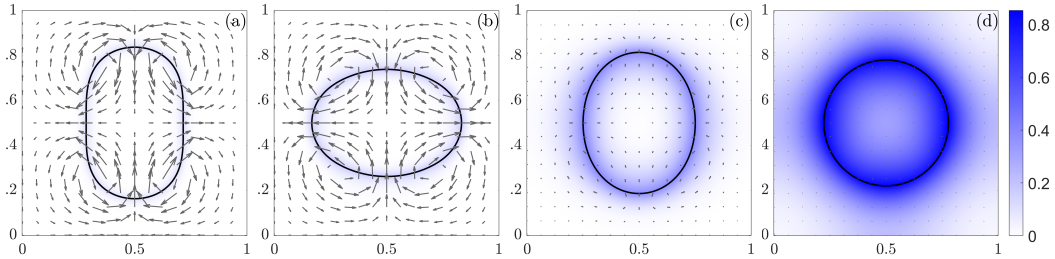

FIGURE 4.1: Snapshots of rubber band simulation with the constant source model and diffusion coefficient $D = 10^{-2}$ m^{2}s^{-1} and desorption coefficient $\kappa = 0.1$ mol m^{-1}s^{-1} using the WENO advection scheme at (a) $t = 0.05$ s, (b) $t = 0.1$ s, (c) $t = 0.5$ s, and (d) $t = 2$ s. The vectors give the velocity field and the color map shows the concentration.

TABLE 4.1: Convergence results for the concentration field solved using a first-order upwind advection scheme with the constant source model and $D = 10^{-2}$ m^{2}s^{-1} and desorption coefficient $\kappa = 0.1$ mol m^{-1}s^{-1} at $t = 2$ s. The error and order of convergence is presented in both the L_2 and L_∞ norms and for the total mass error.

h	Δt	$\|\|c_h - c_{h/2}\|\|_2$	order	$\|\|c_h - c_{h/2}\|\|_\infty$	order	$\|\int_\Omega c_h d\underline{x} - \int_\Omega c d\underline{x}\|$	order
1/32	5.00×10^{-4}	7.46×10^{-2}	-	2.10×10^{-1}	-	2.83×10^{-2}	-
1/64	2.50×10^{-4}	3.38×10^{-2}	1.14	9.45×10^{-2}	1.15	1.57×10^{-2}	0.85
1/128	1.25×10^{-4}	2.22×10^{-2}	0.60	6.75×10^{-2}	0.48	8.53×10^{-3}	0.88
1/256	6.25×10^{-5}	1.30×10^{-2}	0.78	3.93×10^{-2}	0.78	4.51×10^{-3}	0.92

TABLE 4.2: Convergence results for the concentration field solved using a third-order WENO advection scheme with the constant source model and $D = 10^{-2}$ m^{2}s^{-1} and desorption coefficient $\kappa = 0.1$ mol m^{-1}s^{-1} at $t = 2$ s. The error and order of convergence is presented in both the L_2 and L_∞ norms and for the total mass error.

h	Δt	$\|\|c_h - c_{h/2}\|\|_2$	order	$\|\|c_h - c_{h/2}\|\|_\infty$	order	$\|\int_\Omega c_h d\underline{x} - \int_\Omega c d\underline{x}\|$	order
1/32	5.00×10^{-4}	7.67×10^{-2}	-	1.93×10^{-1}	-	1.33×10^{-4}	-
1/64	2.50×10^{-4}	3.39×10^{-2}	1.18	8.92×10^{-2}	1.12	1.46×10^{-3}	-3.45
1/128	1.25×10^{-4}	2.21×10^{-2}	0.62	6.27×10^{-2}	0.51	6.90×10^{-4}	1.08
1/256	6.25×10^{-5}	1.28×10^{-2}	0.79	3.65×10^{-2}	0.78	3.10×10^{-4}	1.15

-0.1 ms^{-2} are given in Table 4.4. The concentration initial condition is $c(\underline{x}, 0) = 1$ mol m^{-2}. Fig 4.3 shows snapshots of this simulation at the most refined grid, $Nx = 512$. Notice that since the total mass in the domain for this case is also unknown, the error for the total mass is computed using the grid refinements, as before with the limited source term.

One can see from Tables 4.2, 4.3, and 4.4 that as the grid is refined, the solution is approaching first order, and the error in the total mass is approaching first order or better, which validates the methodology.

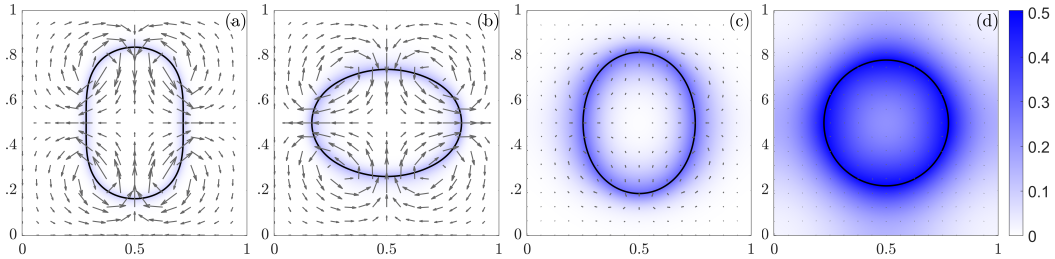

FIGURE 4.2: Snapshots of rubber band simulation with the limited source model and diffusion coefficient $D = 10^{-2}$ m^{2}s^{-1}, saturation limit $C_\infty = 1$ mol m^{-2}, and desorption coefficient $\kappa = 0.1$ ms^{-1} using the WENO advection scheme at (a) $t = 0.05$ s, (b) $t = 0.1$ s, (c) $t = 0.5$ s, and (d) $t = 2$ s. The vectors give the velocity field and the color map shows the concentration.

TABLE 4.3: Convergence results for the concentration field solved using a third-order WENO advection scheme with the the limited source model and $D = 10^{-2}$ m^{2}s^{-1} and desorption coefficient $\kappa = 0.1$ ms^{-1} at $t = 2$ s. The error and order of convergence is presented in both the L_2 and L_∞ norms and for the total mass error.

h	Δt	$\|\|c_h - c_{h/2}\|\|_2$	order	$\|\|c_h - c_{h/2}\|\|_\infty$	order	$\left\|\int_\Omega c_h d\underline{x} - \int_\Omega c_{h/2} d\underline{x}\right\|$	order
1/32	5.00×10^{-4}	7.67×10^{-2}	-	1.93×10^{-1}	-	4.12×10^{-3}	-
1/64	2.50×10^{-4}	3.39×10^{-2}	1.18	8.92×10^{-2}	1.12	4.54×10^{-3}	-0.14
1/128	1.25×10^{-4}	2.21×10^{-2}	0.62	6.27×10^{-2}	0.51	3.19×10^{-3}	0.51
1/256	6.25×10^{-5}	1.28×10^{-2}	0.79	3.65×10^{-2}	0.78	1.96×10^{-3}	0.70

4.4 Coral Simulations

In the `IB2d` library, we have included an example of a pulsing coral and the photosynthesis of the symbiotic algae based on the work presented in Chapters 2 and 3. Photosynthesis is modeled by tracking its byproduct, dissolved oxygen. The motion of the tentacles is prescribed using tether points as in Eq. (2.5) with $\tilde{f}_d = 0$, meaning no damping, and the concentration of dissolved oxygen is produced from the tentacles using Eq. (4.3). The physical and numerical parameters for this example are given in Table 4.5, simulating a single coral polyp pulsing in water. The length of a coral tentacle is 0.4070 cm and the polyp length is 0.9198 cm in a 2.0×5.0 cm^2 box. The coral pulse is composed of a contraction, expansion, and resting period. The Reynolds number is defined using the tentacle length and pulsation frequency as $Re = \rho L^2 \gamma / \mu = 8.7546$ and the Péclet number is set to $Pe = L^2 \gamma / D = 100$. These dimensionless parameters correspond to the simulations presented in Chapter 3.

Snapshots for the coral simulation are given in Fig. 4.4 during the tenth and final pulse. Notice the similarities with Fig. 3.8 in Chapter 3. Once again, the concentration is getting trapped in the vortices and advected away from the tentacles.

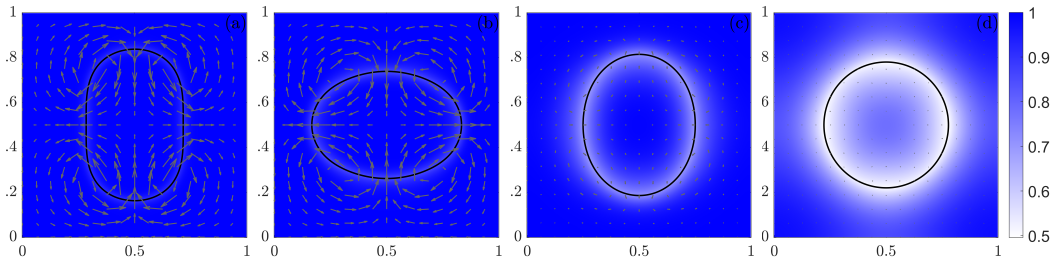

FIGURE 4.3: Snapshots of rubber band simulation with the reaction sink model and diffusion coefficient $D = 10^{-2}$ m^{2}s^{-1} and absorption coefficient $\kappa = -0.1$ ms^{-2} using the WENO advection scheme at (a) $t = 0.05$ s, (b) $t = 0.1$ s, (c) $t = 0.5$ s, and (d) $t = 2$ s. The vectors give the velocity field and the color map shows the concentration.

TABLE 4.4: Convergence results for the concentration field solved using a third-order WENO advection scheme with the reaction sink model and $D = 10^{-2}$ m^{2}s^{-1} and absorption coefficient $\kappa = -0.1$ ms^{-2} at $t = 2$ s. The error and order of convergence is presented in both the L_2 and L_∞ norms and for the total mass error.

h	Δt	$\|\|c_h - c_{h/2}\|\|_2$	order	$\|\|c_h - c_{h/2}\|\|_\infty$	order	$\lvert\int_\Omega c_h d\underline{x} - \int_\Omega c_{h/2} d\underline{x}\rvert$	order
1/32	5.00×10^{-4}	4.76×10^{-2}	-	1.02×10^{-1}	-	1.01×10^{-2}	-
1/64	2.50×10^{-4}	2.09×10^{-2}	1.19	4.55×10^{-2}	1.17	3.67×10^{-3}	1.46
1/128	1.25×10^{-4}	1.28×10^{-2}	0.70	3.03×10^{-2}	0.59	9.29×10^{-4}	1.98
1/256	6.25×10^{-5}	7.18×10^{-3}	0.84	1.60×10^{-2}	0.92	7.12×10^{-5}	3.71

TABLE 4.5: Numerical and physical parameters for the example of pulsing corals.

Parameter	**Value**	**Units**
Domain size	2.0×5.0	cm^2
Tentacle length (L)	0.4070	cm
Fluid density (ρ)	1	g cm^{-3}
Fluid viscosity (μ)	0.01	g cm^{-1}s^{-1}
Pulsation Frequency (γ)	0.5286	s^{-1}
Diffusivity (D)	8.7546×10^{-4}	cm^{2}s^{-1}
Saturation limit (C_∞)	1	$\times 10^{-6}$mol cm^{-3}
Desorbtion coefficient (κ)	0.0215	cm s^{-1}
Time step (Δt)	0.00025	s
Spatial step (h)	1/256	cm
Target stiffness (k_{targ})	5×10^6	g cm s^{-2}

Also, observe that the maximum concentration is similar in magnitude.

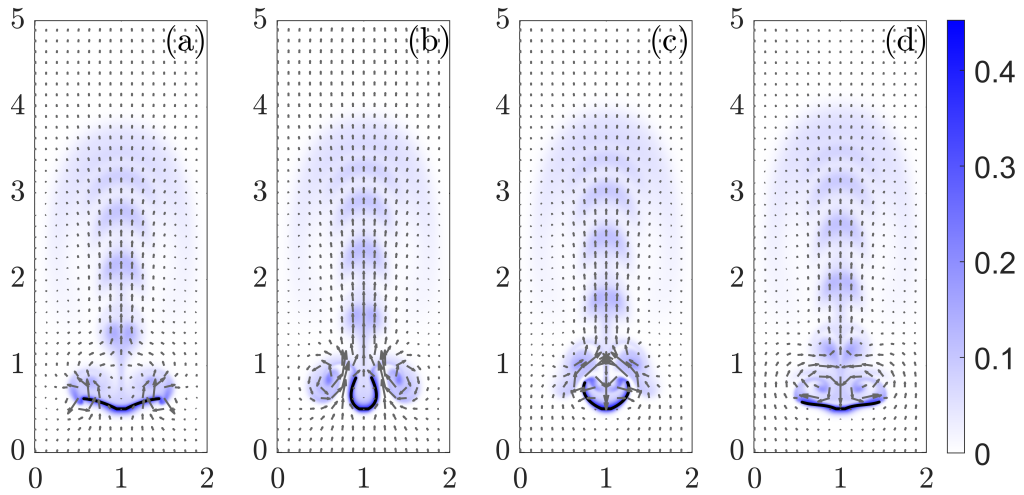

FIGURE 4.4: Snapshots of the coral simulation example included in `IB2d` with the limited source model at approximately (a) 10%, (b) 30%, (c) 50%, and (d) 80% through the tenth pulse. The vectors give the velocity field and the color map shows the concentration.

4.5 Summary and Impact

This chapter has discussed the generalization of the modeling, numerical methods, and applications from Chapters 2 and 3 implemented in the open-source code `IB2d`. Due to this work, students and researchers will be able to use the methodology we have developed for a moving boundary acting as a source or sink of a concentration coupled to fluid flow for various two-dimensional applications allowing them to bypass the steep learning curve to understanding and implementing the methodology. This implementation will allow for a quicker turnaround for advances in two-dimensional applications. It will also allow for an easier transition to advanced topics and applications for student researchers. The new methodology and implementations are discussed in the submitted paper, along with a few example problems. We contributed the coral example we have discussed above; other examples contributed by other authors are flow past a flapping plate used to model heat dissipation on a leaf and flow past moving cylinders used to model a sniffing process.

Chapter 5

Three-Dimensional Simulations

The next goal of this work is to extend the modeling and analysis done in two dimensions and apply it to three-dimensional simulations of the pulsing soft corals. In the full three-dimensional coral model, there are eight tentacles. As the coral pulses, the fluid is replenished through the gaps between tentacles, rather than from fluid above the coral resulting in a continuous upward jet. It was found that full three-dimensional studies were necessary to capture the full dynamics of the fluid flow around pulsing corals [14].

The three-dimensional simulations are conducted using the immersed boundary finite element (`IBFE`) software library [53]. The `IBFE` library is part of the `IBAMR` software package [65]. It allows for a hybrid finite-difference finite-element method, where the fluid flow is solved using the finite-difference method. The immersed boundary is represented using a finite-element (FE) mesh. Using the FE representation for the immersed boundary in the simulations results in a less restrictive time step. The library also has support for adaptive mesh refinement and parallelization. This dissertation will focus on the formulation of the immersed boundary finite-element method rather than the high-performance computing aspect of this software. Additional details can be found in the original paper introducing `IBAMR`, the three-dimensional adaptive mesh, and parallelizable implementation of the immersed boundary method [70]. Collaborator Laura Miller set up the three-dimensional coral simulations, and the code was adapted for the MERCED computing cluster by collaborator Gabrielle Hobson. In this work, there are two goals: (1) to gain insight into the mixing in three dimensions and (2) to incorporate the photosynthesis model coupled with the fluid flow by having the immersed boundary points act as a sink or source of the oxygen concentration.

We present the `IBFE` formulation in Section 5.1. The coral kinematics implemented are discussed in Section 5.2. We present the concentration modeling and corresponding numerical methods in Section 5.3. This section will include a brief survey of the existing framework in `IBAMR` and `IBFE` as well as the numerical methods needed to add the immersed boundary finite element mesh as a source or sink of a concentration. The mixing methodology and results are given in Section 5.4. In Section 5.5 we will present the preliminary simulations where the coral polyp is

coupled to a background concentration. The chapter summary is given in Section 5.6.

5.1 IBFE Formulation

The IBFE formulation is given in three dimensions with a three-dimensional solid immersed boundary rather than an infinitely thin elastic material. As in two dimensions, the fluid flow is modeled by the Navier-Stokes equations,

$$\rho\left(\frac{\partial \underline{u}}{\partial t}+\underline{u}\cdot\nabla\underline{u}\right)+\nabla p=\mu\nabla^2\underline{u}+\underline{f}\ , \tag{5.1}$$

$$\nabla\cdot\underline{u}=0\ , \tag{5.2}$$

where $\underline{u}=(u_1,u_2,u_3)$ is the velocity, p is the pressure, $\underline{f}=(f_1,f_2,f_3)$ is the external body force, $\underline{x}=(x_1,x_2,x_3)$ is the Eulerian cartesian spatial grid, and t is time. We also have the parameters ρ, the fluid density, and μ, the fluid viscosity. As in Chapter 4, quantities in this chapter are all dimensional.

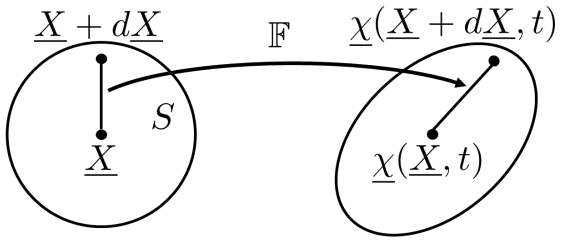

FIGURE 5.1: Schematic of the reference configuration $\underline{X}$ of the immersed boundary mapped to the current configuration at time t, $\underline{\chi}(\underline{X},t)$

.

The Lagrangian structure is defined using its reference configuration

$$\underline{X}=(X_1,X_2,X_3)\in S\ ,$$

where S is the domain of the Lagrangian structure. The reference configuration in this work is defined when there is zero elastic energy. It is used to define the elastic energy of the current configuration. The position of the points at time t in the current configuration is given by $\underline{\chi}(\underline{X},t)$, shown in Fig. 5.1. For this formulation, the first Piola Kirchoff (PK1) stress tensor is used to compute the elastic force, which is preferable for large deformations. Details are provided below.

Consider a line element $d\underline{X}$ as a perturbation of $\underline{X}$ in the reference configuration. Then the perturbation in the current configuration is at time t,

$$d\underline{\chi} = \chi(\underline{X} + d\underline{X}, t) - \chi(\underline{X}, t) \ ,$$

as illustrated in Fig. 5.1. Then one can define,

$$d\underline{\chi} = \mathbb{F} d\underline{X} \ ,$$

where $\mathbb{F}(\underline{X}, t) = \frac{\partial \underline{\chi}}{\partial \underline{X}}$ is the deformation gradient tensor [121].

For a volume dV in the reference configuration, the corresponding volume in the current configuration dv can be related by $dv = JdV$, where the Jacobian $J = \det(\mathbb{F})$. For incompressible materials $J = 1$. A surface element in the reference configuration dS with a unit normal $\underline{N}$ and the corresponding surface element in the current configuration ds with unit normal $\underline{n}$, shown in Fig. 5.2, can be related as

$$\underline{n} ds = J\mathbb{F}^{-T} \underline{N} dS \ , \tag{5.3}$$

called Nanson's formula [121].

In order to understand the PK1 tensor, we will relate it to the Cauchy stress tensor σ. The force acting on a surface element ds in the current configuration is $d\underline{f}^* = \sigma \underline{n} ds$ with unit normal $\underline{n}$. The PK1 tensor, $\mathbb{P}$, is similarly defined in the reference configuration as, $d\underline{f}^* = \mathbb{P}\underline{N} dS$ where dS is the corresponding surface in the reference configuration with normal $\underline{N}$, illustrated in Fig. 5.2. Thus,

$$\mathbb{P}\underline{N} dS = \sigma \underline{n} ds$$

relates the Cauchy and PK1 stress tensors [121]. Using Eq. (5.3),

$$\mathbb{P}\underline{N} dS = J\sigma\mathbb{F}^{-T} \underline{N} dS \ . \tag{5.4}$$

Since this is true for arbitrary dS then Eq. (5.4) reduces to

$$\mathbb{P} = J\sigma\mathbb{F}^{-T} \ , \tag{5.5}$$

defining in terms of the Cauchy stress tensor σ. The PK1 stress tensor defined in Eq. (5.5) is a general form. The specific stress tensor used for the coral simulations describes a passive elastic neo-Hookean material model,

$$\mathbb{P} = \eta_{tot}(\mathbb{F} - \mathbb{F}^{-T}) \ , \tag{5.6}$$

where η_{tot} is the elastic modulus of the material. This model is used to describe the coral tentacle elasticity [15].

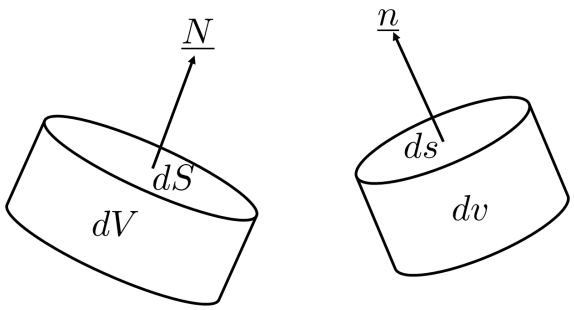

FIGURE 5.2: Schematic of a volume and surface element of reference configuration dV and dS, respectively, with normal $\underline{N}$ and volume and surface element of current configuration dv and ds, respectively, with normal $\underline{n}$.

In the current configuration, the immersed boundary interaction equations are given as,

$$\underline{f}(\underline{x},t) = \int_S \underline{F}(\underline{X},t)\delta(\underline{x}-\underline{\chi}(\underline{X},t))d\underline{X} \ , \tag{5.7}$$

$$\frac{\partial \underline{\chi}(\underline{X},t)}{\partial t} = \underline{U}(\underline{X},t) = \int_\Omega \underline{u}(\underline{x},t)\delta(\underline{x}-\underline{\chi}(\underline{X},t))d\underline{x} \ . \tag{5.8}$$

As before $F(\underline{X},t)$ is the force of the boundary on the fluid defined in Lagrangian coordinates and $f(\underline{x},t)$ is the force of the boundary on the fluid defined in Eulerian coordinates. $\underline{U}(\underline{X},t)$ is the velocity of the immersed boundary. The force in Eq. (5.7) is defined as,

$$\underline{F}(\underline{X},t) = \underline{F}_{targ} + \underline{F}_{elast}$$

Where $\underline{F}_{targ}$ is the target force which prescribes the motion of the coral tentacles in the current configuration,

$$\underline{F}_{targ} = \kappa_T \left(\underline{\chi}_T(\underline{X},t) - \underline{\chi}(\underline{X},t)\right) \ . \tag{5.9}$$

Here, $\underline{\chi}_T(\underline{X},t)$ prescribes the configuration and κ_T is the spring constant. $\underline{F}_{elast}$ is the force due to the elasticity of the material defined using the PK1 tensor $\mathbb{P}$ given in Eq. (5.6),

$$\int_S \underline{F}_{elast} \cdot \underline{G}(\underline{X})d\underline{X} = -\int_S \mathbb{P}(\underline{X},t) : \nabla_x \underline{G} d\underline{X} \ . \tag{5.10}$$

This definition is given in weak form for a test function $\underline{G}$ [65].

5.1.1 Numerical Implementation

To solve for the velocity and pressure, $\underline{u}(\underline{x},t)$ and $p(\underline{x},t)$, the Navier-Stokes equations Eqs. (5.1) and (5.2), are discretized using finite differences on an adaptive Cartesian mesh with a staggered grid, see Fig. 5.3. The velocities are defined on the cell faces,

$$(u_b)_{i-n,j-m,k-l}$$

for $b = 1,2,3$. For each b, the corresponding values of n, m, and l are shown in Fig. 5.3. The pressure is defined on the cell centers, $p_{i-1/2,j-1/2,k-1/2}$, similar to what was presented for the MAC grid in two dimensions, discussed in Chapter 2.

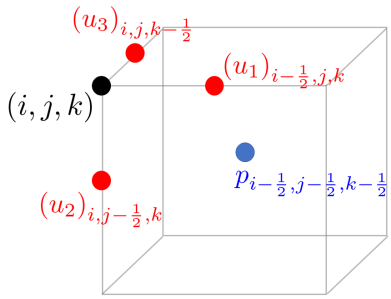

FIGURE 5.3: Three-dimensional staggered grid used to solve the Navier-Stokes equations in `IBAMR`. The cell node is given in black, the locations of the velocities are given in red, and the location of the pressure is given in blue.

The Lagrangian structure is discretized using a finite element representation. The nodes of the mesh are denoted as

$$\{\underline{X}_l\}_{l=1}^{M}$$

for nodes $l = 1,\ldots,M$. The positions of the nodes of the Lagrangian mesh are given as $\{\underline{\chi}_l(t)\}_{l=1}^{M}$. An example is given in Fig. 5.4. The finite element basis functions are defined as $\{\underline{G}(\underline{X})\}_{l=1}^{M}$. Using these definitions, the discretion of $\underline{\chi}(\underline{X},t)$ is given as

$$\underline{\chi}_{\Delta s}(\underline{X},t) = \sum_{l=1}^{M} \underline{\chi}_l(t)\underline{G}_l(\underline{X}) \ ,$$

for Lagrangian grid size Δs. Notice here that we are summing over the FE nodes $\chi_l(t)$. The discretized deformation gradient $\mathbb{F}$ is approximated as,

$$\mathbb{F}_{\Delta s}(\underline{X},t) = \frac{\partial \underline{\chi}_{\Delta s}}{\partial \underline{X}}(\underline{X},t) = \sum_{l=1}^{M} \underline{\chi}_l(t)\frac{\partial \underline{G}_l}{\partial \underline{X}}(\underline{X}) \ .$$

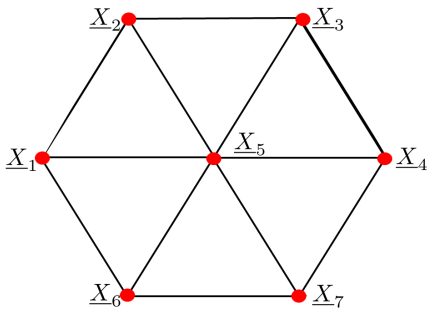

FIGURE 5.4: Schematic of a finite element mesh. Finite element nodes are given in red.

Notice here that we are summing over the FE nodes $\underline{\chi}_l(t)$. Additionally the force, $\underline{F}(\underline{X},t)$, is approximated as,

$$\underline{F}_{\Delta s}(\underline{X},t) = \sum_{l=1}^{M} \underline{F}_l(t)\underline{G}_l(\underline{X}) \ .$$

Recalling that $\underline{F}_l = (\underline{F}_{elast})_l + (\underline{F}_{targ})_l$ is defined on FE node l. To find $(\underline{F}_{targ})_l$ we discretize Eq. (5.9),

$$(\underline{F}_{targ})_l = \kappa_T \left((\underline{\chi}_T)_l - \underline{\chi}_l \right) \ .$$

To find $(\underline{F}_{elast})_l$ we solve the discretized form of Eq. (5.10),

$$\sum_{l=1}^{M} \left(\int_S \underline{G}_l(\underline{X})\underline{G}_m(\underline{X})d\underline{X} \right) \underline{F}_{elast\,\Delta s} = -\int_S \mathbb{P}_{\Delta s}(\underline{X},t)\nabla_X \underline{G}_m(\underline{X})d\underline{X}$$

for each m = 1, ..., M. The integrals are approximated with Gaussian quadrature.

The force spreading given in Eq. (5.7) is discretized as,

$$(f_b)_{i-n,j-m,k-l} = \sum_{S^e} \int_S F_b(\underline{X},t)\delta_h(\underline{x}_{i-n,j-m,k-l} - \underline{\chi}(\underline{X},t))d\underline{X} \tag{5.11}$$

for b,n,m,l defined in Fig. 5.3 and finite elements S^e. The integrals are approximated using Gaussian quadrature. Note that we can define an operator $\mathbb{S}$ such that $\underline{f}(\underline{x},t) = \mathbb{S}(\underline{\chi}(\cdot,t))\underline{F}(\underline{X},t)$, where the operator $\mathbb{S}$ is implicitly defined using Eq. 5.11 where Gaussian Quadrature is used.

The velocity interpolation given in Eq. (5.8) is instead defined using a velocity-restriction operator $\mathbb{V}(\underline{\chi}(\cdot,t))$ in order to find the correct motion of the Lagrangian mesh

$$\frac{\partial \underline{\chi}}{\partial t} = \mathbb{V}(\underline{\chi}(\cdot,t))\underline{u}(\underline{x},t)$$

The velocity-restriction operator is necessary to define $\frac{\partial \underline{\chi}}{\partial t}$ in this way since the components of $\underline{U}$ cannot generally be expressed as linear combinations of the finite-element basis functions . In order to define $\mathbb{V}$ the discrete power identity is enforced,

$$(\underline{F}, \mathbb{V}\underline{u})_x = (\mathbb{S}\underline{F}, \underline{u})_x \ . \tag{5.12}$$

The Lagrangian operator $(\cdot,\cdot)_x$ is defined as $(\underline{A},\underline{B})_x = [A]^T \mathbb{M}[B]$ for arbitrary vectors $\underline{A}$ and $\underline{B}$ and the entries of $\mathbb{M}$ are given by $\int_S G_l(\underline{X})G_m(\underline{X})d\underline{X}$. The $[\cdot]$ notation indicates the vector of discretized values. The Eulerian inner product $(\cdot,\cdot)_x$ is defined as $(\underline{a},\underline{b})_x = [a]^T [b] h^2$ for arbitrary vectors $\underline{a}$ and $\underline{b}$. Thus Eq. 5.12 is discretized as,

$$[\underline{F}]^T [\mathbb{M}] [\mathbb{V}] [\underline{u}] = ([\mathbb{S}] [\underline{F}])^T [\underline{u}] h^2$$

and the velocity-restriction operator is defined as

$$\mathbb{V} = \mathbb{M}^{-1}\mathbb{S}^T h^2 \ .$$

Note that $\mathbb{V}\underline{u}$ is an approximation of

$$U_b = \sum_{ijk} (u_b)_{i-n,j-m,k-l} \delta_h(\underline{x}_{i-n,j-m,k-l} - \underline{\chi}(\underline{X},t))h^2$$

where U_b refers to the velocity interpolated on to the immersed boundary points and b,n,m,l are defined in Fig. 5.3.

5.2 Coral Kinematics

In Chapter 2, we used specific interpolating polynomials to describe the coral tentacles' kinematic motion in two dimensions. In three dimensions, the kinematics have been significantly simplified as described in Samson et al. [15]. We present kinematics in Fig. 5.9 for three dimensions, assuming the motion is planar for each of the eight tentacles. The kinematics give the position of the target point positions, $\underline{\chi}_T(\underline{X},t)$, in Eq (5.9). The tangent angle of the tentacle relative to the horizontal axis is given by,

$$\theta(s,t) = A(1 - e^{s/\beta(t)}) \ ,$$

for the dimensionless arclength $0 \le s \le 1$, prefactor $A = 1.9$, and $\beta(t)$ is a function dependent the time,

$$\beta(t) = \begin{cases} \beta_o + (\beta_m - \beta_o)\left(\frac{t}{t_c}\right)^2 & 0 \le t \le t_c \\ \beta_m + (\beta_o - \beta_m)\left(\frac{t-t_c}{t_f - t_c}\right)^2 & t_c \le t \le t_f \end{cases}$$

for the time of a pulse, $t_f = 1.6167$, the contraction time, $t_c = 0.7333$, and parameters

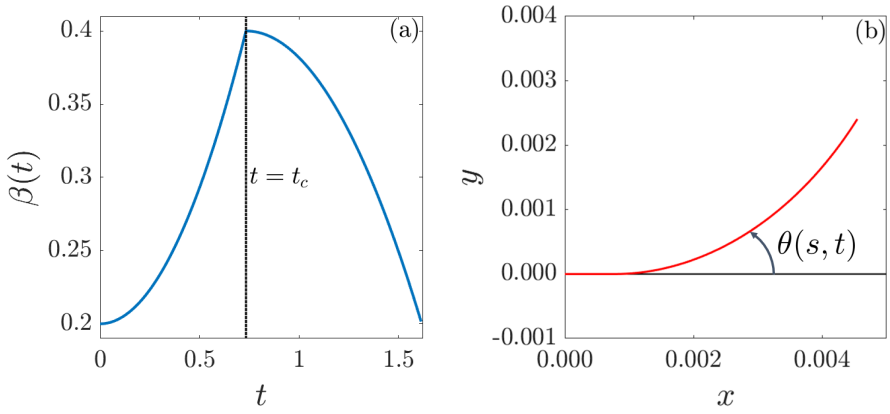

FIGURE 5.5: (a) Values of $\beta(t)$ corresponding to the closing phase for $t < t_c$ and the opening phase for $t > t_c$. (b) Coral kinematics in red showing $\theta(s,t)$.

$\beta_o = 0.2$ and $\beta_m = 0.4$. The prefactor A gives the approximate angle at the tip of the tentacles during the contraction. $\beta(t)$ is a periodic time dependent function that controls the opening and closing phases of the coral. $\beta(t)$ is shown in Fig. 5.5(a) and θ in relation to the coral tentacle is given in Fig. 5.5(b), . The coral kinematics are shown in Fig 5.6 in two dimensions. The closing phase is shown in Fig 5.6(a) in blue and the opening phase is shown in Fig 5.6(b) in red. The finite-element coral in the three-dimensional simulations in the initial position is shown in Fig 5.6(c).

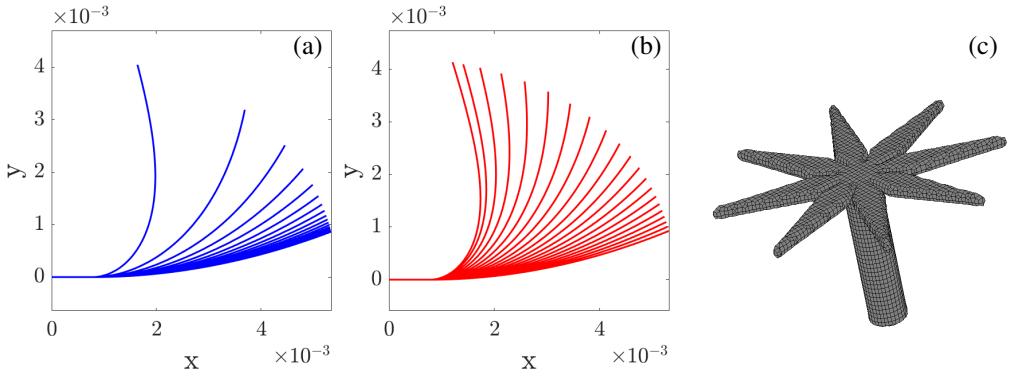

FIGURE 5.6: Coral kinematics in the (a) closing phase and (b) opening phase shown in 2D. (c) The finite-element coral in the three-dimensional simulations in the initial position.

5.3 Concentration Modeling

IBAMR and IBFE have the capability for three-dimensional advection-diffusion-reaction equations coupled to the fluid flow solved from the fluid-structure interaction equations. The three-dimensional advection-diffusion-reaction equations are,

$$c_t + \underline{u} \cdot \nabla c = D\nabla^2 c + r \tag{5.13}$$

The concentration is given by $c(\underline{x},t)$, $\underline{u}(\underline{x},t) = (u_1,u_2,u_3)$ is the velocity from the fluid-structure interaction, and D is the diffusion coefficient. The user-defined reaction function is $r(\underline{x},t)$. In order to have the immersed boundary as the sink or source of the concentration, the defined reaction term needs to be linked to the immersed boundary. Currently, it is only possible to define the reaction term as a function of $\underline{x}$ and t. Since it is known that the fluid dynamics of the full three-dimensional simulations have characteristics not captured in the two-dimensional simulations [14], we expect to see differences in the concentration dynamics presented in this chapter in comparison to the concentration dynamics presented in Chapter 3.

The goal of this work is to modify the reaction function to allow for the coral tentacles to act as a source or sink on the concentration,

$$r(\underline{x},t) = \int_{\partial S} \tilde{f}(\underline{\chi}(\underline{X},t))\delta(\underline{x} - \underline{\chi}(\underline{X},t))dA(\underline{X}) \ , \tag{5.14}$$

where as before, the current location of the Lagrangian structure at time t is given as $\underline{\chi}(\underline{X},t)$ with reference configuration $\underline{X}$. Note here that only the points on the surface of the immersed boundary are considered as sources of oxygen, since the boundary is now a three-dimensional structure rather than an infinitely thin surface. The source or sink model is described as $\tilde{f}(\underline{\chi}(\underline{X},t))$. As a first choice, we will consider the constant model, $\tilde{f}(\underline{\chi}(\underline{X},t)) = \kappa$.

5.3.1 Numerical Methods

In the IBAMR framework, there are multiple different options for various numerical schemes. Rather than an exhaustive survey of all of them, we will instead focus on the methods used for the coral simulations, which are based on code developed by collaborators [15].

The current discretization of Eq. (5.13) in IBAMR is in two steps. The concentration, velocity, and reaction term at the nth time step is given as c^n, $\underline{u}^n$, and r^n, respectively. The first step updates c^n from time t^n to $t^{n+1/2}$, using $\underline{u}^n$ and r^n,

$$c^{n+\frac{1}{2}} = c^n + \frac{2}{\Delta t}\left(-\underline{u}^n \cdot \tilde{\nabla}_h c^n + \frac{D}{2}\nabla_h^2\left(c^{n+\frac{1}{2}} + c^n\right) + r^n\right) \ . \tag{5.15}$$

The second step updates c^n from time t^n to t^{n+1}, using $\underline{u}^{n+1/2}$, $\underline{c}^{n+1/2}$, and $r^{n+1/2}$,

$$c^{n+1} = c^n + \frac{1}{\Delta t}\left(-\underline{u}^{n+\frac{1}{2}} \cdot \tilde{\nabla}_h c^{n+\frac{1}{2}} + \frac{D}{2}\nabla_h^2\left(c^{n+1} + c^n\right) + r^{n+\frac{1}{2}}\right) , \tag{5.16}$$

where ∇_h^2 is the standard centered second-order finite difference Laplacian operator and the values $\underline{u}^n$ and $\underline{u}^{n+1/2}$ come from the solving Eqs. (5.1) and (5.2). The advective term, $\underline{u}^n \cdot \tilde{\nabla}_h c^n$ is defined using a piece-wise parabolic method (PPM), a high-resolution implementation of the Godunov method [122]. The reaction term r^n and $r^{n+1/2}$ are defined by the user as a function. The corresponding linear equations are solved using an iterative Krylov solver.

Recalling that we have a three-dimensional Lagrangian mesh, discretized using a finite element representation, shown in Figs. 5.4 and 5.6. The nodes of the mesh are denoted as $\{\underline{X}_l\}_{l=1}^M$ for nodes $l = 1,\ldots,M$ and the positions of the nodes of the Lagrangian mesh are given as $\{\underline{\chi}_l(t)\}_{l=1}^M$.

For each element $S^e \in \partial S$, Eq. (5.14) is discretized as,

$$r_{i,j,k} = \sum_{S^e \in \partial S} \int_{\partial S} \tilde{f}_{\Delta s}(\underline{X},t)\delta_h(\underline{x}_{i,j,k} - \underline{\chi}(\underline{X},t))dA(\underline{X}) , \tag{5.17}$$

where the integral is solved using Gaussian quadrature as before with the force spreading function, Eq. (5.7). As before, the integral is defined only on the surface of the immersed boundary ∂S. The discrete source or sink model, $\tilde{f}$ is defined using the finite element basis functions,

$$\tilde{f}_{\Delta s}(\underline{X},t) = \sum_{l=1}^{M} \tilde{f}_l(t)\underline{G}_l(\underline{X}) .$$

5.3.2 Proposed Implementation in `IBAMR`

Although the work discussed in the previous subsection has not yet been fully implemented, we have investigated the current source code to find the best way to implement the methodology. In `IBAMR`, the software that handles the advection-diffusion-reaction equations, the Navier-Stokes solver, and the immersed boundary finite-element (`IBFE`) representation are all in separate classes. The advection-diffusion-reaction classes are linked to the classes used to solve the Navier-Stokes equations since the fluid velocity is needed in the advection term. The classes used to solve the Navier-Stokes equations and the classes used for the IBFE method are linked since both are coupled through the immersed boundary interaction equations. However, the classes that use the IBFE method and the advection-diffusion-reaction classes are not linked, and this has presented the largest challenge. The current plan defines the source or sink term in the `IBFE` classes and then sends the source or sink

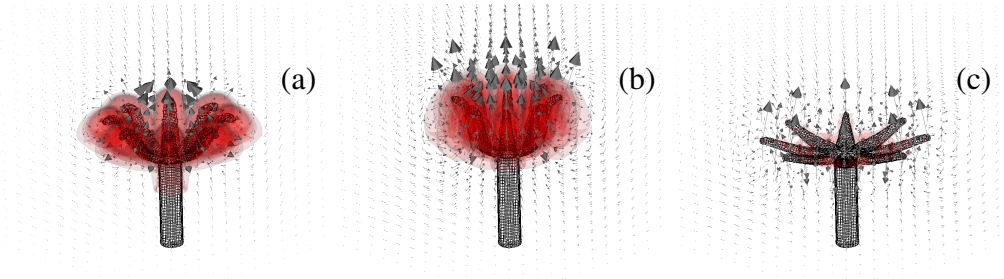

FIGURE 5.7: Snapshots of three-dimensional coral simulation during the tenth pulse at (a) $t = 14.8$s, (b) $t = 15.0$s, and (c) $t = 16.3$s. The vectors show the velocity fields and the red shows the vorticity magnitude contours.

term to the advection-diffusion-reaction solver. This will be completed in the same manner as to how the other classes are linked.

5.4 Three-Dimensional Mixing Analysis

The methods and intuition developed in Chapter 3 are now being implemented to study the three-dimensional flow fields. The challenge is now there is an additional dimension to consider, so the Poincaré map manifolds are surfaces rather than curves.

Here the three-dimensional coral simulation is conducted on a square domain of -0.0496 m $\leq x \leq 0.0496$ m, -0.0496 m $\leq z \leq 0.0496$ m, and -0.0070432 m $\leq y \leq 0.0921568$ m, with coral stem centered at the origin. The spatial mesh is adaptive with three levels. The finest mesh is $h_{fine} = 0.00992/512 = 0.00019375$m. The time step is chosen to be $\Delta t = 0.0001$s. The physical and numerical parameters are given in Table 5.1.

TABLE 5.1: Numerical and physical parameters for three-dimensional pulsing corals.

Parameter	**Value**	**Units**
Domain size	$0.0992 \times 0.0992 \times 0.0992$	m^3
tentacle length (L)	0.0055	m
Fluid density (ρ)	1029	kg m^{-3}
Fluid viscosity (μ)	0.00108	N s m^{-2}
Pulsation Frequency (γ)	0.61854	s^{-1}
Time step (Δt)	0.0001	s

The simulations are run for ten pulses up to $t = 16.32867$ s. The characteristic length in this problem is the length of a coral tentacle, L, the characteristic frequency is the frequency of the pulsation, γ, given in Table 5.1. These parameters correspond to a Reynolds number of $Re = \frac{\rho L^2 \gamma}{\mu} \approx 17.8$. Snapshots of the three-dimensional

coral simulation during the tenth pulse are shown in Fig. 5.7. The coral motion, fluid velocity field, and vorticity are shown. A continuous upward jet is present above the coral throughout the pulse [14].

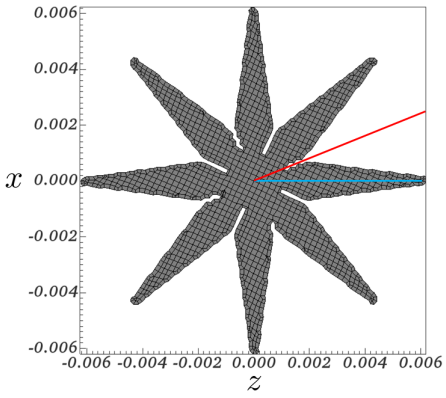

FIGURE 5.8: Visualization of slices. The blue line indicates the slice down the center of of the tentacle, and the red line indicates the slice down the center of the tentacle gap.

Since the flow field simulations are parallelized, using adaptive mesh refinement, the velocity data must be exported to a manageable format to post-process and analyze. When interpolating the data to a uniform grid, it was challenging to ensure the incompressibility of the flow. The solution is building the Poincaré Maps using VisIt, an open-source visualization software developed by Lawrence Livermore National Laboratory [123]. VisIt allows for direct access to the format of the output of the simulations, SAMRAI files.

The Poincaré maps are built using the Integral Curve operator. Massless tracers are seeded into desirable locations and advected forward or backward in time using an Adams-Bashforth scheme over the final pulse in the simulation. A Python script is used, which takes the new locations of these massless tracers after being advected over one pulse as the new seed locations to be advected in time and looped over multiple pulses.

We begin by using two-dimensional slices of the data to gain intuition into the three-dimensional mixing dynamics. We analyze slices through the center of the tentacle gap and the center of a tentacle, shown in Fig. 5.8. Due to numerical error, the tracers would sometimes be advected off of these planes. In these cases, the tracers were projected back to the plane at the end of each pulse.

5.4.1 Mixing Results

Approximately 150 points were seeded randomly into each slice, and they were advected forward over 127 pulses to create a Poincaré section, shown in Fig. 5.9. The Poincaré section of the slice through the center of the tentacle, given in blue in

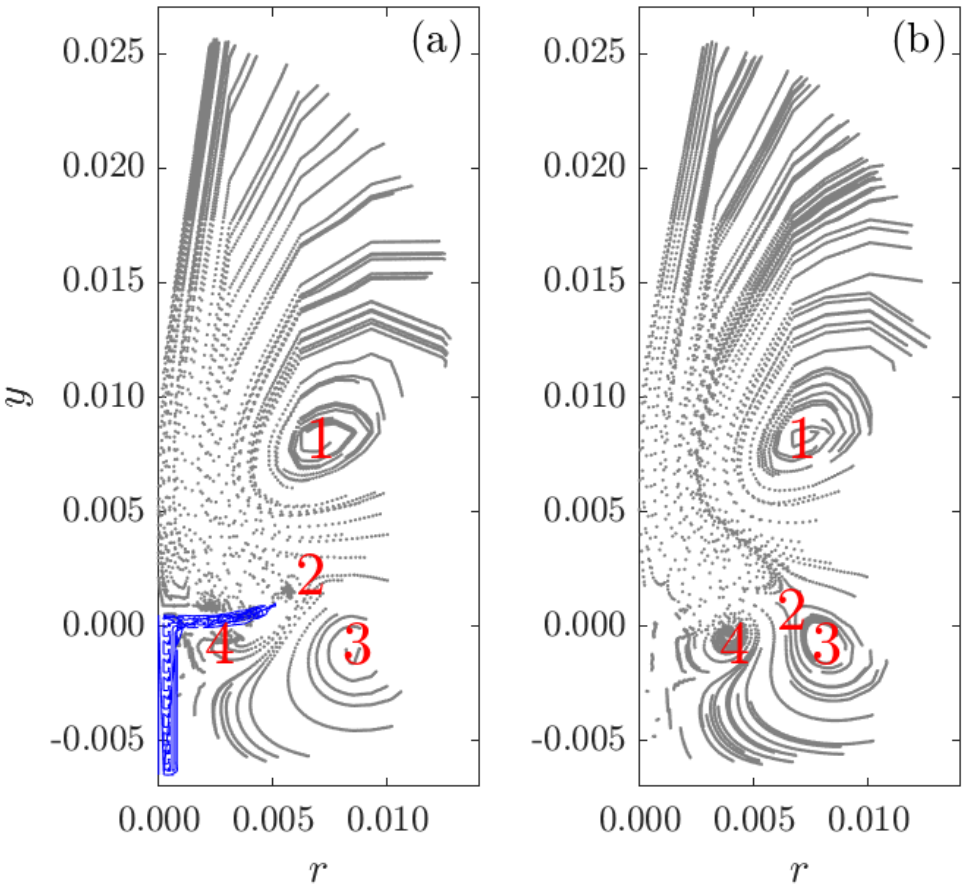

FIGURE 5.9: Poincaré sections for a slice (a) down the center of the tentacle and (b) down the center of the gap between the tentacles, as shown in Fig. 5.8. The x-axis is the radius away from the center of the coral stem, and the y-axis is the vertical component of the domain. In (a) the location of the coral tentacles and stem are given in blue. The red numbers denote different areas that contain fixed points.

Fig. 5.8, is shown in Fig. 5.9(a), with the coral stem and tentacle location shown in blue. The Poincaré section of the slice through the center of the gap between tentacles, given in red in Fig. 5.8, is shown in Fig. 5.9(b). The red numbers indicate areas where fixed points are being located. The area marked by 2 behaves like a hyperbolic fixed point that generates invariant manifolds. The areas marked by 1, 3, and 4 behave like stable and unstable spiral fixed points or invariant tori. In the two-dimensional simulations, there would be no sinks or sources as the velocity field is divergence-free. In these three-dimensional simulations, the velocity field is divergence-free, but the two-dimensional slices are not.

Recall that chaotic advection is indicated by a sensitivity to initial conditions.

That means that the distance between two points that are initially close together increases exponentially. However, in this system, we can qualitatively see that there is not very much chaos. For the biologically relevant Reynolds number in the two-dimensional system, there is much more chaos. We anticipate that the more quantitative analysis of the three-dimensional mixing will result in different results from the two-dimensional mixing.

5.5 Three-Dimensional Concentration Results

The implementation of the methodology described in Section 5.3 is currently in progress. Here, we present simulations of a background concentration coupled to the three-dimensional simulation of a soft coral presented in Section 5.4 shown in Fig. 5.7. The fluid parameters given in Table 5.1 are used in these simulations.

The initial condition of the concentration is a Gaussian function centered on the coral stem,

$$c(\underline{x},0) = e^{(-10^{-4}x_1^2 - 10^{-7}x_2^2 - 10^{-4}x_3^2)} .$$

Two diffusion coefficients are used, $D = 10^{-6}$ m^{2}s^{-1} and $D = 10^{-8}$ m^{2}s^{-1}. The corresponding Péclet number are $Pe = \frac{L^2\gamma}{D} \approx 18.7$ and 1871 for $D = 10^{-6}$ m^{2}s^{-1} and $D = 10^{-8}$ m^{2}s^{-1}, respectively.

Snapshots of the coral simulation are given in Fig. 5.10 for $D = 10^{-6}$ m^{2}s^{-1} and in Fig. 5.11 for $D = 10^{-8}$ m^{2}s^{-1}. In Fig. 5.10, the coral advects the oxygen concentration up, but diffusion dominates oxygen concentration dynamics due to the smaller Péclet number. However, in Fig. 5.11, one can see that the concentration dynamics are more dependent on the flow field due to the larger Péclet number. In 5.11(f), one can see oxygen gets advected away by the upward jet away from the coral. This work simulates the coral moving and mixing the fluid with an initial large buildup of oxygen around the tentacles. However, this does not take the oxygen being produced by the symbiotic algae on the tentacles into account. In order to get a deeper understanding of the photosynthesis dynamics, we need to couple the oxygen concentration with a sink or source located on the immersed boundary.

5.6 Summary

In this chapter, we have presented three-dimensional coral simulations using `IBFE`. We have included a discussion of the implementation of `IBFE` and how we prescribe the coral motion based on work done by collaborators [15]. Additionally, we overviewed the existing methodology in `IBAMR` to couple a fluid-structure interaction to a background concentration using an advection-diffusion-reaction equation. We have proposed a numerical methodology that would allow for the three-dimensional finite element mesh to be a sink or source of concentration using `IBFE`

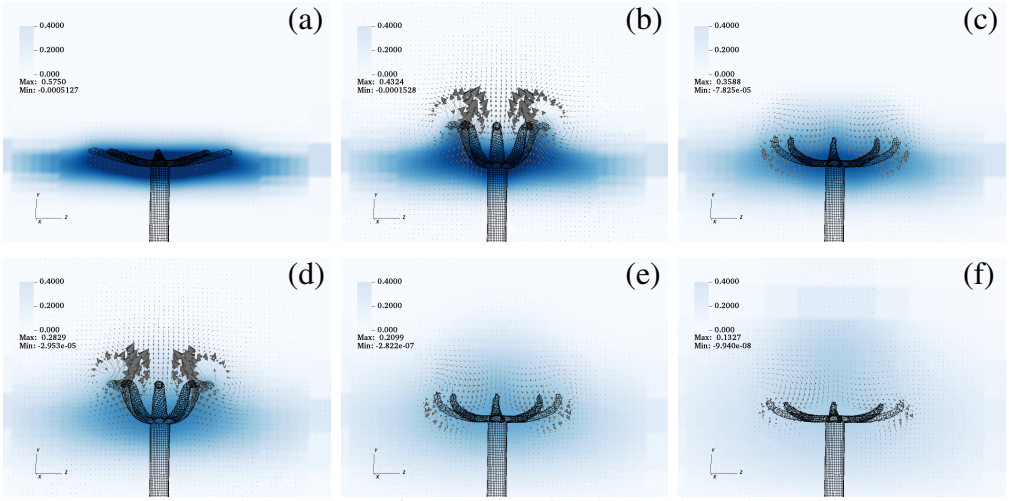

FIGURE 5.10: Snapshots of three-dimensional coral simulations with a background concentration shown for $D = 10^{-6}$ m^2s^{-1} with blue color map and velocity vectors shown with grey arrows at (a) t = 0.5 s, (b) t = 1.0 s, (c) t = 1.6 s, (d) t = 2.6 s, (e) t = 4.85 s, and (d) t = 16.3 s.

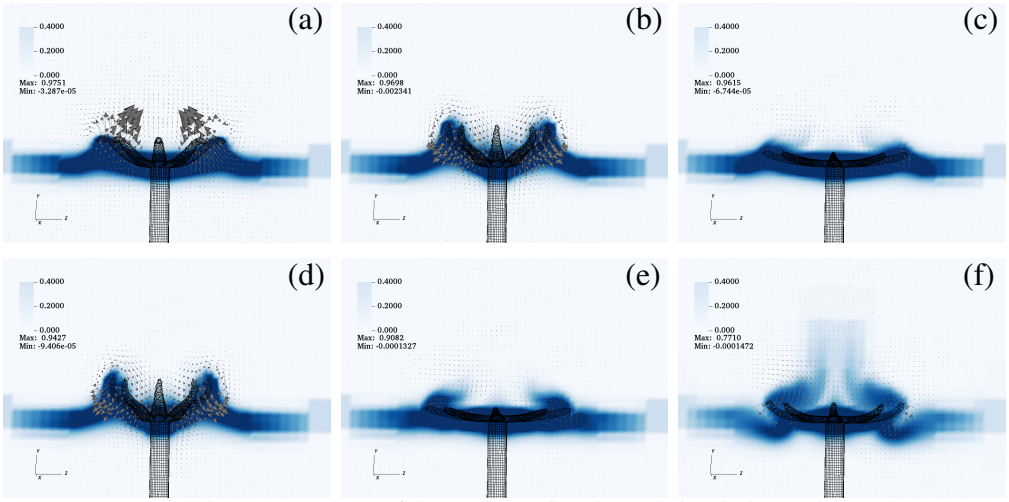

FIGURE 5.11: Snapshots of three-dimensional coral simulations with a background concentration for $D = 10^{-8}$ m^2s^{-1} shown with blue color map and velocity vectors shown with grey arrows at (a) t = 0.5 s, (b) t = 1.0 s, (c) t = 1.6 s, (d) t = 2.6 s, (e) t = 4.85 s, and (d) t = 16.3 s.

and discussed the best way to implement this. Additionally, we presented some preliminary work looking at Poincaré sections on two-dimensional slices of the three-dimensional simulations. We also presented preliminary work with three-dimensional coral simulations coupled to a background concentration.

Chapter 6

Conclusions and Future Work

In this dissertation, mathematical models, numerical methods, and simulations of pulsing soft corals and photosynthesis of their symbiotic algae are presented.

The modeling and numerical methods for a two-dimensional coral are presented in Chapter 2 and include a novel methodology to model photosynthesis, where the coral tentacles act as a source of the photosynthesis by-product, oxygen. The numerical methodology included a discussion of the immersed boundary method used to solve the fluid-structure interaction of the coral tentacle pulsing. We also discussed how the fluid-structure interaction is coupled to the photosynthesis model. In the photosynthesis model, we track the oxygen concentration in the fluid governed by the advection-diffusion equation. The numerical methods include a third-order WENO scheme for the advective terms and Crank-Nicolson for the diffusive term. The source term defined at the coral tentacle location was handled explicitly using a second-order Runge-Kutta method. The methodology was validated by conducting a convergence study of the fluid velocity and oxygen concentration dynamics. This study informed which spatial grid sizes were necessary for the numerical simulations and results presented.

The two-dimensional coral results are given in Chapter 3. Using the simulated velocity fields, we implement a dynamical systems approach using Poincaré maps to quantify mixing due to chaotic advection. The use of Poincaré maps in this work has been instrumental in understanding the fluid flow and quantifying the mixing. By analyzing the invariant manifolds presented, we were able to quantify how much fluid is replenished near the coral over one pulse. Additionally we used the oxygen concentration dynamics to evaluate the photosynthesis in different regimes. To investigate the coupled role of fluid inertia and diffusivity on photosynthesis dynamics, we simultaneously vary the Reynolds and Péclet numbers. We look at the role of these parameters on the maximum concentration, the evaluation of the source term, the average concentration in the domain, the concentration variance, and the flux across lines at varying heights away from the coral. The metrics used to analyze the photosynthesis dynamics in two dimensions showed increased mixing and more oxygen production for smaller Péclet numbers. In this regime, the oxygen concentration diffuses away from the tentacles and allows for more mixing and less buildup of oxygen concentration around the tentacles. These results were similar for

all simulated Reynolds numbers. However, the biologically relevant Péclet number for dissolved oxygen in water is large, $O(100) - O(1000)$ and in this regime, fluid flow plays a significant role. Smaller Reynolds numbers resulted in less mixing and photosynthesis due to more reversible flow, while the increased inertia of the larger Reynolds number allowed for more mixing and more photosynthesis. This benefit of the larger Reynolds number was not uniform. For Reynolds numbers larger than $Re = 8$, the benefit was considerably less. This behavior indicates that the biologically relevant Reynolds number, $Re \approx 8$, is advantageous for mixing and photosynthesis in a larger Péclet regime, suggesting that these corals expend the minimal energy required to gain the most benefit.

The role of fluid flow and diffusion in capture mechanisms of appendages, such as feeding or olfaction, has been well-studied [43]–[45], [124], [125]. It is widely accepted that although the appendages bring the materials close to the desired location, the actual capture is dominated by the diffusion dynamics [124]. In this work, rather than capturing material, the coral is expelling a by-product. One expects these dynamics to be similar, where diffusion dominates the dynamics near the tentacle. After the diffusion has transported the oxygen a short distance away from the tentacle, the fluid can transport oxygen farther away from the coral. Instead, in Fig. 3.21 we observe that the fluid dynamics do affect the concentration close to the tentacles. As the Reynolds number increases, the width of the oxygen buildup around the tentacle decreases. The increased inertia in the fluid flow removes oxygen by thinning the width of the accumulated oxygen around the tentacle. Thus both advective and diffusive forces can be significant in the dynamics close to appendages.

A significant component of this work is contributing the methods developed in Chapter 2 to open-source libraries so that other researchers and students can use these tools. We have discussed the implementation in the software library `IB2d` in Chapter 4, which will allow students and researchers to use these methods on two-dimensional applications. In this chapter, the methodology is presented generalizing the methods developed in Chapter 2, where the immersed boundary acts as a source or a sink of a concentration. In addition to contributing this methodology, the third-order WENO scheme for the advective terms in the advection-diffusion equation was introduced for better mass conservation in larger Péclet number regimes. Additionally, this work additionally led to a more robust implementation of the force-spreading operator used in the immersed boundary method component of the library. The results presented include a convergence study of a canonical immersed boundary example to validate the methodology and an example modeling a two-dimensional coral with photosynthesis. Additionally, collaborators used the methodology to model heat transfer over a flapping leaf and a sniffing process.

Chapter 5 introduces the three-dimensional coral simulations using the software library `IBAMR`. We first present the relevant modeling and numerical methods for the fluid-structure interaction when using the IBFE method. Next, the existing modeling and numerical methods present in `IBAMR` to couple the fluid-structure interaction

with the advection-diffusion-reaction equations are discussed. The modeling and numerical methods to discretize the immersed boundary using a finite element mesh acting as a sink or source of a concentration are proposed. We then discuss using Poincaré maps on two-dimensional slices of the three-dimensional simulations to understand the mixing in three dimensions. We present Poincaré sections to gain insight into the location of fixed points and qualitatively look at the mixing. We found that there was much more chaotic mixing in the two-dimensional simulations compared to the three-dimensional simulations. Further study of these dynamics will be completed in future work. Preliminary simulations are presented with the fluid-structure interaction coupled to a background oxygen concentration in two different Péclet number regimes to begin studying the photosynthesis dynamics in three dimensions.

The models, methods, and analysis provided in this dissertation can be used in scientific, industrial, and engineering applications where a pumping, pulsing, or stirring mechanism facilitates mixing. They can also be used to analyze photosynthesis, mass transfer, and heat transfer in other biological systems. These methods can also be used to understand feeding, sniffing, chemotaxis, and waste removal in biological organisms.

Bibliography

[1] T. Y. Wu, "Fish Swimming and Bird/Insect Flight", *Annual Review of Fluid Mechanics*, vol. 43, no. 1, pp. 25–58, Jan. 2011.

[2] H. Liu, S. Ravi, D. Kolomenskiy, and H. Tanaka, "Biomechanics and biomimetics in insect-inspired flight systems", *Philosophical Transactions of the Royal Society B: Biological Sciences*, vol. 371, no. 1704, p. 20 150 390, Sep. 2016.

[3] M. S. Triantafyllou and G. S. Triantafyllou, "An Efficient Swimming Machine", *Scientific American*, vol. 272, no. 3, pp. 64–70, 1995.

[4] H. Liu, "Simulation-Based Biological Fluid Dynamics in Animal Locomotion", en, *Applied Mechanics Reviews*, vol. 58, no. 4, pp. 269–282, Jul. 2005.

[5] P. W. Webb, "Body Form, Locomotion and Foraging in Aquatic Vertebrates", en, *Integrative and Comparative Biology*, vol. 24, no. 1, pp. 107–120, Feb. 1984.

[6] M. J. Lighthill, "Aquatic animal propulsion of high hydromechanical efficiency", en, *Journal of Fluid Mechanics*, vol. 44, no. 2, pp. 265–301, Nov. 1970.

[7] R. Godoy-Diana and B. Thiria, "On the diverse roles of fluid dynamic drag in animal swimming and flying", *Journal of The Royal Society Interface*, vol. 15, no. 139, p. 20 170 715, Feb. 2018.

[8] G. V. Lauder and E. G. Drucker, "Forces, Fishes, and Fluids: Hydrodynamic Mechanisms of Aquatic Locomotion", *Physiology*, vol. 17, no. 6, pp. 235–240, Dec. 2002.

[9] I. K. Bartol, P. S. Krueger, J. T. Thompson, and W. J. Stewart, "Swimming dynamics and propulsive efficiency of squids throughout ontogeny", en, *Integrative and Comparative Biology*, vol. 48, no. 6, pp. 720–733, Dec. 2008.

[10] Y Gabay, Y Benayahu, and M Fine, "Does elevated $p\mathrm{co}_2$ affect reef ocotocorals?", *Ecology and Evolution*, vol. 3, pp. 465–473, 3 2013.

[11] P.-J. Sung, M.-R. Lin, M. Y. Chiang, and T.-L. HWANG, "Soft corals and sea fans-a comprehensive guide to the tropical shallow-water genera of the central-west pacific, the indian ocean and the red sea soft corals and sea fans-a comprehensive guide to the tropical shallow-water genera of the central-west pacific, the indian ocean and the red sea 55, 154-157, 2001", *Bulletin of the Chemical Society of Japan*, vol. 82, no. 8, pp. 987–996, 2009.

[12] K. Fabricius and D. Klumpp, "Widespread mixotrophy in reef-inhabiting soft corals: The influence of depth, and colony expansion and contraction on photosynthesis", *Marine Ecology Progress Series*, vol. 125, pp. 195–204, 1995.

[13] M. Kremien, U. Shavit, T. Mass, and A. Genin, "Beneft of pulsation in soft corals", *Proceedings of the National Academy of Sciences of The United States of America*, vol. 110, no. 22, pp. 8978–8983, 2013.

[14] J. E. Samson, L. A. Miller, D. Ray, R. Holzman, U. Shavit, and S. Khatri, "A novel mechanism of mixing by pulsing corals", *Journal of Experimental Biology*, vol. 222, no. 15, 2019.

[15] J. E. Samson and L. A. Miller, "Collective pulsing in xeniid corals: Part ii—using computational fluid dynamics to determine if there are benefits to coordinated pulsing.", *Bulletin of Mathematical Biology*, vol. 82, no. 67, 2020.

[16] G. J. Collatz, M Ribas-Carbo, and J. Berry, "Coupled photosynthesis-stomatal conductance model for leaves of c4 plants", *Functional Plant Biology*, vol. 19, no. 5, pp. 519–538, 1992.

[17] D. De Pury and G. Farquhar, "Simple scaling of photosynthesis from leaves to canopies without the errors of big-leaf models", *Plant, Cell & Environment*, vol. 20, no. 5, pp. 537–557, 1997.

[18] W. Duncan, R Loomis, W Williams, R. Hanau, *et al.*, "A model for simulating photosynthesis in plant communities", *Hilgardia*, vol. 38, no. 4, pp. 181–205, 1967.

[19] R. Leuning, "A critical appraisal of a combined stomatal-photosynthesis model for c3 plants", *Plant, Cell & Environment*, vol. 18, no. 4, pp. 339–355, 1995.

[20] M. Dring, "Chromatic adaptation of photosynthesis in benthic marine algae: An examination of its ecological significance using a theoretical model", *Limnology and Oceanography*, vol. 26, no. 2, pp. 271–284, 1981.

[21] B.-P. Han, M. Virtanen, J. Koponen, and M. Straškraba, "Effect of photoinhibition on algal photosynthesis: A dynamic model", *Journal of plankton research*, vol. 22, no. 5, pp. 865–885, 2000.

[22] W. Xiong, C. Gao, D. Yan, C. Wu, and Q. Wu, "Double co2 fixation in photosynthesis–fermentation model enhances algal lipid synthesis for biodiesel production", *Bioresource technology*, vol. 101, no. 7, pp. 2287–2293, 2010.

[23] J. P. Bitog, I. B. Lee, C. G. Lee, K. S. Kim, H. S. Hwang, S. W. Hong, I. H. Seo, K. S. Kwon, and E. Mostafa, "Application of computational fluid dynamics for modeling and designing photobioreactors for microalgae production: A review", en, *Computers and Electronics in Agriculture*, vol. 76, no. 2, pp. 131–147, May 2011.

[24] T. Mass, A. Genin, U. Shavit, M. Grinstein, and D. Tchernov, "Flow enhances photosynthesis in marine benthic autotrophs by increasing the efflux of oxygen from the organism to the water", en, *Proceedings of the National Academy of Sciences*, vol. 107, no. 6, pp. 2527–2531, Feb. 2010.

[25] W. C. Dennison and D. J. Barnes, "Effect of water motion on coral photosynthesis and calcification", en, *Journal of Experimental Marine Biology and Ecology*, vol. 115, no. 1, pp. 67–77, Feb. 1988.

[26] O. H. Shapiro, V. I. Fernandez, M. Garren, J. S. Guasto, F. P. Debaillon-Vesque, E. Kramarsky-Winter, A. Vardi, and R. Stocker, "Vortical ciliary flows actively enhance mass transport in reef corals", en, *Proceedings of the National Academy of Sciences*, vol. 111, no. 37, pp. 13 391–13 396, Sep. 2014.

[27] B. A. Egan and J. R. Mahoney, "Numerical modeling of advection and diffusion of urban area source pollutants", *Journal of Applied Meteorology and Climatology*, vol. 11, no. 2, pp. 312–322, 1972.

[28] B. Faugeras and O. Maury, "Modeling fish population movements: From an individual-based representation to an advection–diffusion equation", *Journal of Theoretical Biology*, vol. 247, no. 4, pp. 837–848, 2007.

[29] J. L. Largier, "Considerations in estimating larval dispersal distances from oceanographic data", *Ecological Applications*, vol. 13, no. sp1, pp. 71–89, 2003.

[30] J. van der Lee and L. De Windt, "Present state and future directions of modeling of geochemistry in hydrogeological systems", *Journal of Contaminant Hydrology*, vol. 47, no. 2, pp. 265–282, 2001, International Conference on the Chemistry and Migration Behaviour.

[31] M. Ghalambaz, E. Jamesahar, M. A. Ismael, and A. J. Chamkha, "Fluid-structure interaction study of natural convection heat transfer over a flexible oscillating fin in a square cavity", *International Journal of Thermal Sciences*, vol. 111, pp. 256–273, 2017.

[32] A. Al-Amiri and K. Khanafer, "Fluid–structure interaction analysis of mixed convection heat transfer in a lid-driven cavity with a flexible bottom wall", *International Journal of Heat and Mass Transfer*, vol. 54, no. 17, pp. 3826–3836, 2011.

[33] Q. Fang, S. Sakadžić, L. Ruvinskaya, A. Devor, A. M. Dale, and D. A. Boas, "Oxygen advection and diffusion in a three dimensional vascular anatomical network", *Optics express*, vol. 16, no. 22, pp. 17 530–17 541, 2008.

[34] S. R. Lynch, N. Nama, Z. Xu, C. J. Arthurs, O. Sahni, and C. A. Figueroa, "Numerical considerations for advection-diffusion problems in cardiovascular hemodynamics", *International Journal for Numerical Methods in Biomedical Engineering*, vol. 36, no. 9, e3378, 2020.

[35] A.-R. Khaled and K. Vafai, "The role of porous media in modeling flow and heat transfer in biological tissues", *International Journal of Heat and Mass Transfer*, vol. 46, no. 26, pp. 4989–5003, 2003.

[36] Y. Deleuze, C.-Y. Chiang, M. Thiriet, and T. W. Sheu, "Numerical study of plume patterns in a chemotaxis–diffusion–convection coupling system", *Computers & Fluids*, vol. 126, pp. 58–70, 2016.

[37] J. R. N. Lazier and K. H. Mann, "Turbulence and the diffusive layers around small organisms", en, *Deep Sea Research Part A. Oceanographic Research Papers*, vol. 36, no. 11, pp. 1721–1733, Nov. 1989.

[38] S. Michelin and E. Lauga, "Optimal feeding is optimal swimming for all péclet numbers", *Physics of Fluids*, vol. 23, no. 10, p. 101 901, 2011.

[39] H. U. Riisgård and P. S. Larsen, "Particle capture mechanisms in suspension-feeding invertebrates", en, *Marine Ecology Progress Series*, vol. 418, pp. 255–293, Nov. 2010.

[40] S. Van Wassenbergh and P. Aerts, "Rapid pivot feeding in pipefish: Flow effects on prey and evaluation of simple dynamic modelling via computational fluid dynamics", *Journal of The Royal Society Interface*, vol. 5, no. 28, pp. 1291–1301, Nov. 2008.

[41] S. D. Olson, "Fluid dynamic model of invertebrate sperm chemotactic motility with varying calcium inputs", en, *Journal of Biomechanics*, Special Issue: Biofluid Mechanics, vol. 46, no. 2, pp. 329–337, Jan. 2013.

[42] A. Kiselev and L. Ryzhik, "Biomixing by chemotaxis and enhancement of biological reactions", *Communications in Partial Differential Equations*, vol. 37, no. 2, pp. 298–318, 2012.

[43] L. Waldrop, M. Reidenbach, and M. Koehl, "Flexibility of crab chemosensory sensilla enables flicking antennules to sniff", *Biological Bulletin*, vol. 229, pp. 185–198, Oct. 2015.

[44] L. D. Waldrop, L. A. Miller, and S. Khatri, "A tale of two antennules: The performance of crab odour-capture organs in air and water", *Journal of The Royal Society Interface*, vol. 13, no. 125, p. 20 160 615, Dec. 2016.

[45] L. D. Waldrop, Y. He, and S. Khatri, "What can computational modeling tell us about the diversity of odor-capture structures in the pancrustacea?", *Journal of Chemical Ecology*, vol. 44, 1084–1100, 2018.

[46] M. J. Weissburg, "The fluid dynamical context of chemosensory behavior", *The Biological Bulletin*, vol. 198, no. 2, pp. 188–202, 2000.

[47] R. Stocker and J. R. Seymour, "Ecology and Physics of Bacterial Chemotaxis in the Ocean", en, *Microbiology and Molecular Biology Reviews*, vol. 76, no. 4, pp. 792–812, Dec. 2012.

[48] S. JR., S. R., A. T., and S. R., "Chemoattraction to dimethylsulfoniopropionate throughout the marine microbial food web.", *Science (New York, N.Y.)*, vol. 329, pp. 342–5, 2010.

[49] P. N. Dudley, R. Bonazza, T. T. Jones, J. Wyneken, and W. P. Porter, "Leatherbacks swimming in silico: Modeling and verifying their momentum and heat balance using computational fluid dynamics", *PLOS ONE*, vol. 9, no. 10, pp. 1–14, Oct. 2014.

[50] M. M. Hossain and A. E. Staples, "Passive vortical flows enhance mass transport in the interior of a coral colony", *Physics of Fluids*, vol. 31, no. 6, p. 061 701, 2019.

[51] C. S. Peskin, "The immersed boundary method", *Acta Numerica*, vol. 11, pp. 479–517, 2002.

[52] ——, "Flow patterns around heart valves: A numerical method", *Journal of Computational Physics*, vol. 10, no. 2, pp. 252–271, 1972.

[53] B. E. Griffith and X. Luo, "Hybrid finite difference/finite element immersed boundary method", *International journal for numerical methods in biomedical engineering*, vol. 33, no. 12, 2017.

[54] A. Baird, L. Waldrop, and L. Miller, "Neuromechanical pumping: Boundary flexibility and traveling depolarization waves drive flow within valveless, tubular hearts", *Japan Journal of Industrial and Applied Mathematics*, vol. 32, no. 3, pp. 829–846, 2015.

[55] R. P. Beyer, "A computational model of the cochlea using the immersed boundary method", *J. Comput. Phys.*, vol. 98, pp. 145–162, 1992.

[56] L. J. Fauci and A. McDonald, "Sperm motility in the presence of boundaries", *Bulletin of Mathematical Biology*, vol. 57, no. 5, pp. 679–699, 1984.

[57] L. J. Fauci and C. S. Peskin, "A computational model of aquatic animal", *Journal of Computational Physics*, vol. 77, pp. 85–108, 1988.

[58] G. Herschlag and L. Miller, "Reynolds number limits for jet propulsion: A numerical study of simplified jellyfish", *Journal of Theoretical Biology*, vol. 285, pp. 84–95, 2011.

[59] C. Tu and C. S. Peskin, "Stability and instability in the computation of flows with moving immersed boundaries: a comparison of three methods", *SIAM Journal on Scientific and Statistical Computing*, vol. 13, no. 6, pp. 1361–1376, 1992.

[60] D. Goldstein, R. Handler, and L. Sirovich, *Modeling a no-slip flow boundary with an external force field*, 1993.

[61] M. C. Lai and C. S. Peskin, "An immersed boundary method with formal second-order accuracy and reduced numerical viscosity", *Journal of Computational Physics*, vol. 160, no. 2, pp. 705–719, 2000.

[62] J. M. Teran and C. S. Peskin, "Tether force constraints in Stokes flow by the immersed boundary method on a periodic domain", *SIAM Journal on Scientific Computing*, vol. 31, no. 5, pp. 3404–3416, 2009.

[63] K. Y. Chen, K. A. Feng, Y. Kim, and M. C. Lai, "A note on pressure accuracy in immersed boundary method for Stokes flow", *Journal of Computational Physics*, vol. 230, no. 12, pp. 4377–4383, 2011.

[64] Y. Bao, A. Donev, B. E. Griffith, D. M. McQueen, and C. S. Peskin, "An immersed boundary method with divergence-free velocity interpolation and force spreading", *Journal of Computational Physics*, vol. 347, pp. 183–206, 2017.

[65] B. E. Griffith, "On the volume conservation of the immersed boundary method", *Communications in Computational Physics*, vol. 12, no. 2, pp. 401–432, 2012.

[66] Y. Kim and C. S. Peskin, "Penalty immersed boundary method for an elastic boundary with mass", *Physics of Fluids*, vol. 19, no. 5, p. 053 103, 2007.

[67] Y. Liu and Y. Mori, "Properties of discrete delta functions and local convergence of the immersed boundary method", *SIAM Journal on Numerical Analysis*, vol. 50, no. 6, pp. 2986–3015, 2012.

[68] Y Mori, "Convergence proof of the velocity field for a stokes flow immersed boundary method", *Communications of Pure and Applied Mathematics*, vol. 61, no. 9, pp. 1213–1263, 2007.

[69] N. A. Battista, A. J. Baird, and L. A. Miller, "A mathematical model and MATLAB code for muscle-fluid-structure simulations", *Integrative and Comparative Biology*, vol. 55, no. 5, pp. 901–911, 2015.

[70] B. E. Griffith, R. D. Hornung, D. M. McQueen, and C. S. Peskin, "An adaptive, formally second order accurate version of the immersed boundary method", *Journal of Computational Physics*, vol. 223, no. 1, pp. 10–49, 2007.

[71] S. Osher and J. A. Sethian, "Fronts propagating with curvature-dependent speed: Algorithms based on hamilton-jacobi formulations", *Journal of computational physics*, vol. 79, no. 1, pp. 12–49, 1988.

[72] O. C. Zienkiewicz, R. L. Taylor, P. Nithiarasu, and J. Zhu, *The finite element method*. McGraw-hill London, 1977, vol. 3.

[73] W Dettmer and D Perić, "A computational framework for fluid–structure interaction: Finite element formulation and applications", *Computer Methods in Applied Mechanics and Engineering*, vol. 195, no. 41-43, pp. 5754–5779, 2006.

[74] R. Eymard, T. Gallouët, and R. Herbin, "Finite volume methods", *Handbook of numerical analysis*, vol. 7, pp. 713–1018, 2000.

[75] S. Khatri and A.-K. Tornberg, "An embedded boundary method for soluble surfactants with interface tracking for two-phase flows", *Journal of Computational Physics*, vol. 256, pp. 768–790, 2014.

[76] K. Y. Chen and M. C. Lai, "A conservative scheme for solving coupled surface-bulk convection-diffusion equations with an application to interfacial flows with soluble surfactant", *Journal of Computational Physics*, vol. 257, pp. 1–18, 2014.

[77] M. M. Hopkins and L. J. Fauci, "A computational model of the collective fluid dynamics of motile micro-organisms", en, *Journal of Fluid Mechanics*, vol. 455, pp. 149–174, Mar. 2002.

[78] R. Dillon, L. Fauci, A. Fogelson, and D. Gaver III, "Modeling biofilm processes using the immersed boundary method", *Journal of Computational Physics*, vol. 129, no. 1, pp. 57–73, 1996.

[79] H. Aref, "Chaotic advection of fluid particles", *Philosophical Transactions of the Royal Society of London. Series A: Physical and Engineering Sciences*, vol. 333, no. 1631, pp. 273–288, 1990.

[80] J. M. Ottino, "Mixing, chaotic advection, and turbulence", *Annual Review of Fluid Mechanics*, vol. 22, no. 1, pp. 207–254, 1990.

[81] M. A. Stremler, F. R. Haselton, and H. Aref, "Designing for chaos: Applications of chaotic advection at the microscale", *Philosophical Transactions of the Royal Society of London. Series A: Mathematical, Physical and Engineering Sciences*, vol. 362, no. 1818, pp. 1019–1036, 2004.

[82] A. Mokrani, C. Castelain, and H. Peerhossaini, "The effects of chaotic advection on heat transfer", *International Journal of Heat and Mass Transfer*, vol. 40, no. 13, pp. 3089–3104, 1997.

[83] M. Speetjens, G. Metcalfe, and M. Rudman, "Lagrangian transport and chaotic advection in three-dimensional laminar flows", *Applied Mechanics Reviews*, vol. 73, no. 3, p. 030 801, 2021.

[84] H. Aref, "Stirring by chaotic advection", *Journal of fluid mechanics*, vol. 143, pp. 1–21, 1984.

[85] A Babiano, G. Boffetta, A Provenzale, and A. Vulpiani, "Chaotic advection in point vortex models and two-dimensional turbulence", *Physics of fluids*, vol. 6, no. 7, pp. 2465–2474, 1994.

[86] S. Wiggins, "The dynamical systems approach to lagrangian transport in oceanic flows", *Annu. Rev. Fluid Mech.*, vol. 37, pp. 295–328, 2005.

[87] P. H. Haynes, "Transport and mixing in the atmosphere", *Mechanics of the 21st Century*, pp. 139–152, 2005.

[88] D Perugini, G Poli, and R. Mazzuoli, "Chaotic advection, fractals and diffusion during mixing of magmas: Evidence from lava flows", *Journal of Volcanology and Geothermal Research*, vol. 124, no. 3-4, pp. 255–279, 2003.

[89] A. Schelin, G. Károlyi, A. De Moura, N. Booth, and C Grebogi, "Chaotic advection in blood flow", *Physical Review E*, vol. 80, no. 1, p. 016 213, 2009.

[90] A. Priye, Y. A. Hassan, and V. M. Ugaz, "Microscale chaotic advection enables robust convective dna replication", *Analytical chemistry*, vol. 85, no. 21, pp. 10 536–10 541, 2013.

[91] J. Sivasamy, Z. Che, T. N. Wong, N.-T. Nguyen, and L. Yobas, "A simple method for evaluating and predicting chaotic advection in microfluidic slugs", *Chemical engineering science*, vol. 65, no. 19, pp. 5382–5391, 2010.

[92] M. A. Bees, I Mezic, and J McGlade, "Planktonic interactions and chaotic advection in langmuir circulation", *Mathematics and Computers in Simulation*, vol. 44, no. 6, pp. 527–544, 1998.

[93] B. Orme, S. Otto, and J. Blake, "Enhanced efficiency of feeding and mixing due to chaotic flow patterns around choanoflagellates", *Mathematical Medicine and Biology*, vol. 18, no. 3, pp. 293–325, 2001.

[94] J. Peng and J. O. Dabiri, "Transport of inertial particles by Lagrangian coherent structures: Application to predator–prey interaction in jellyfish feeding", en, *Journal of Fluid Mechanics*, vol. 623, pp. 75–84, Mar. 2009.

[95] T. P. Chiang, W. H. Sheu, and R. R. Hwang, "Effect of Reynolds number on the eddy structure in a lid-driven cavity", de, *International Journal for Numerical Methods in Fluids*, vol. 26, no. 5, pp. 557–579, 1998.

[96] E. Guilmineau and P. Queutey, "A numerical simulation of vortex shedding from an oscillating circular cylinder", *Journal of Fluids and Structures*, vol. 16, no. 6, pp. 773 –794, 2002.

[97] I. Jadic, R. So, and M. Mignolet, "Analysis of fluid– structure interactions using a time-marching technique", *Journal of Fluids and Structures*, vol. 12, no. 6, pp. 631 –654, 1998.

[98] R. D. Moser, J. Kim, and N. N. Mansour, "Direct numerical simulation of turbulent channel flow up to Re=590", en, *Physics of Fluids*, vol. 11, no. 4, pp. 943–945, Apr. 1999.

[99] A. M. Tartakovsky and S. P. Neuman, "Effects of Peclet number on pore-scale mixing and channeling of a tracer and on directional advective porosity", en, *Geophysical Research Letters*, vol. 35, no. 21, 2008.

[100] S. Michelin and E. Lauga, "Phoretic self-propulsion at finite Péclet numbers", en, *Journal of Fluid Mechanics*, vol. 747, pp. 572–604, May 2014.

[101] R. B. Fdhila and P. C. Duineveld, "The effect of surfactant on the rise of a spherical bubble at high Reynolds and Peclet numbers", en, *Phys. Fluids*, vol. 8, no. 2, p. 13, 1996.

[102] S. Ubal, C. H. Harrison, P. Grassia, and W. J. Korchinsky, "Numerical simulation of mass transfer in circulating drops", en, *Chemical Engineering Science*, vol. 65, no. 10, pp. 2934–2956, May 2010.

[103] N. Kishore, R. P. Chhabra, and V. Eswaran, "Mass Transfer from Ensembles of Newtonian Fluid Spheres at Moderate Reynolds and Peclet Numbers", en, *Chemical Engineering Research and Design*, vol. 85, no. 8, pp. 1203–1214, Jan. 2007.

[104] M. Santiago, K. A. Mitchell, and S. Khatri, "A numerical method for modeling photosynthesis of algae on pulsing soft corals", *Submitted*, 2021.

[105] R. Dillon, L. Fauci, and D. Gaver, III, "A microscale model of bacterial swimming, chemotaxis and substrate transport", *Journal of Theoretical Biology*, vol. 177, no. 4, pp. 325–340, 1995.

[106] A. Chorin, "Numerical solution of the Navier-Stokes equations", *Mathematics of Computation*, vol. 22, no. 104, pp. 745–762, 1968.

[107] L. J. P. Timmermans, P. D. Minev, and F. N. Van De Vosse, "an Approximate Projection Scheme for Incompressible Flow Using Spectral Elements", *International Journal for Numerical Methods in Fluids*, vol. 22, no. 7, pp. 673–688, 1996.

[108] J. L. Guermond and J. Shen, "On the error estimates for the rotational pressure-correction projection methods", *Mathematics of Computation*, vol. 73, no. 248, pp. 1719–1738, 2003.

[109] L. Klinteberg, D. Lindbo, and A. K. Tornberg, "An explicit Eulerian method for multiphase flow with contact line dynamics and insoluble surfactant", *Computers and Fluids*, vol. 101, pp. 50–63, 2014.

[110] S.-G. Cai, A Ouahsine, H Smaoui, J Favier, and Y Hoarau, "An efficient implicit direct forcing immersed boundary method for incompressible flows", *Journal of Physics: Conference Series*, vol. 574, p. 012 165, 2015.

[111] F Harlow and J Welch, "Numerical calculation of time-dependent viscous incompressible flow of fluid with free surface", *Physics of Fluids*, vol. 8, pp. 2182–2189, 12 1965.

[112] J. M. Stockie and B. R. Wetton, "Analysis of stiffness in the immersed boundary method and implications for time-stepping schemes", *Journal of Computational Physics*, vol. 154, no. 1, pp. 41–64, 1999.

[113] G. Strang, "On the construction and comparison of difference schemes", *SIAM Journal on Numerical Analysis*, vol. 5, no. 3, 1968.

[114] X.-D. Liu, S. Osher, T. Chan, *et al.*, "Weighted essentially non-oscillatory schemes", *Journal of computational physics*, vol. 115, no. 1, pp. 200–212, 1994.

[115] Y. Liu and Y. Mori, "Lp convergence of the immersed boundary method for stationary Stokes problems", *SIAM Journal on Numerical Analysis*, vol. 52, no. 1, pp. 496–514, 2014.

[116] J. Meiss, "Thirty years of turnstiles and transport", *Chaos*, vol. 25, no. 1, 2015.

[117] W. Liu and G. Haller, "Strange eigenmodes and decay of variance in the mixing of diffusive tracers", *Physica D: Nonlinear Phenomena*, vol. 188, no. 1, pp. 1 –39, 2004.

[118] N. A. Battista, W. C. Strickland, and L. A. Miller, "Ib2d: A python and matlab implementation of the immersed boundary method", *Bioinspiration & biomimetics*, vol. 12, no. 3, p. 036 003, 2017.

[119] N. A. Battista, W. C. Strickland, A. Barrett, and L. A. Miller, "Ib2d reloaded: A more powerful python and matlab implementation of the immersed boundary method", *Mathematical Methods in the Applied Sciences*, vol. 41, no. 18, pp. 8455–8480, 2018.

[120] M. Santiago, N. A. Battista, L. A. Miller, and S. Khatri, "Concentration dynamics incorporated into the library ib2d, a two-dimensional implementation of the immersed boundary method", *Submitted*, 2021.

[121] P. Kelly. (2021). "Mechanics lecture notes: An introduction to solid mechanics", [Online]. Available: `http://homepages.engineering.auckland.ac.nz/~pkel015/SolidMechanicsBooks/index.html` (visited on 2021).

[122] W. J. Rider, J. A. Greenough, and J. R. Kamm, "Accurate monotonicity- and extrema-preserving methods through adaptive nonlinear hybridizations", *Journal of Computational Physics*, vol. 225, no. 2, pp. 1827–1848, 2007.

[123] H. Childs, E. Brugger, B. Whitlock, J. Meredith, S. Ahern, D. Pugmire, K. Biagas, M. Miller, C. Harrison, G. H. Weber, H. Krishnan, T. Fogal, A. Sanderson, C. Garth, E. W. Bethel, D. Camp, O. Rübel, M. Durant, J. M. Favre, and P. Navrátil, "Visit: An end-user tool for visualizing and analyzing very large data", in *High Performance Visualization–Enabling Extreme-Scale Scientific Insight*, 2012, pp. 357–372.

[124] M. A. R. Koehl, "Hydrodynamics of sniffing by crustaceans", in *Chemical Communication in Crustaceans*, T. Breithaupt and M. Thiel, Eds. New York, NY: Springer New York, 2011, pp. 85–102.

[125] M. Koehl, "The Fluid Mechanics of Arthropod Sniffing in Turbulent Odor Plumes", *Chemical Senses*, vol. 31, no. 2, pp. 93–105, Dec. 2005.